Interwell Connectivity in Tight Formations

Mirzayev, Mammad

UNIVERSITY OF CALGARY

Interwell Connectivity in Tight Formations

by

Mammad Mirzayev

A THESIS

SUBMITTED TO THE FACULTY OF GRADUATE STUDIES

IN PARTIAL FULFILMENT OF THE REQUIREMENTS FOR THE

DEGREE OF DOCTOR OF PHILOSOPHY

GRADUATE PROGRAM IN CHEMICAL AND PETROLEUM ENGINEERING

CALGARY, ALBERTA

MAY, 2018

ABSTRACT

A significant amount of oil and gas are present in formations having permeability less than 100μd. Although these tight reservoirs typically have small well spacings, not all well pairs exhibit connectivity because of the reservoir heterogeneity. Measuring connectivity can improve model realism and identify important geological controls sufficiently that field management can be made more reliable.

In this study, we use the Capacitance Model (CM) to evaluate interwell connectivity. In order to render the CM suitable for tight reservoirs, we modified the model by adding a pseudo-well (CM-PW). This modification lets us apply the model to any areal window of interest and cope with long-transient periods in the production well flow rates. The CM-PW was tested with several heterogeneous simulation cases, which revealed that calculated connectivities from the tight permeability reservoirs agreed with results from higher permeability cases with only minor errors (< 7%). We applied the CM-PW to selected waterflooded areas from the East Pembina (Cardium Formation) and the Forget North (Bakken Formation) fields. As a further improvement on the existing CM analysis, horizontal wells were included in our field analyses.

- In the East Pembina Field, we could identify the effects of net local principal stress and hydraulic fracturing proppant amounts on the interwell connectivity. Pre-stimulation interwell connectivities are consistent with the maximum horizontal stress direction. We found that a change in connectivity was directly proportional with proppant tonnage. Also, the effect of the conglomerate layer on connectivity was studied. We found that strongest pseudo well connectivities are directed to the conglomerate-bearing region and the connectivities were related to the formation flow capacity. Finally, we also observed connectivity behavior consistent with the expected sandbody extent as identified through geological studies.
- In the Forget North Field connectivity study, we correlated well-to-well connectivities with geological and seismic analyses. We found that the natural fracture intensity and the Lodgepole Formation aquifer may be causes of long distance connectivity.

It is well known that the CM evaluation is affected by the formation diffusivity. Using the analogy with heat conduction, we propose a method to determine an “area of influence” for an

injection well. The method includes recognition that, in addition to the diffusivity, the injection rate frequency content affects the area size. The method was applied to determine the areal window size for the CM-PW application in tight oil reservoirs. From simulated and field applications, we observed that the interwell distance at the connectivity limit is within 3 to 5% of the interwell distance estimated from the heat conduction-based method.

The modified CM allows us to extend the application to important new reservoir cases. The two field studies once again show the important role of geological features on reservoir communication. Finally, the importance of the injection rate frequency spectrum on the CM measurement opens up a new understanding of the injection well influence in reservoir performance.

ACKNOWLEDGMENTS

I wish to express my sincere thanks to my supervising professor, Dr. Jerry Lee Jensen, for his support and guidance throughout my graduate studies. I am also thankful to Dr. Federico Krause and Dr. Christopher Clarkson for their service on my dissertation committee. Their support is sincerely acknowledged.

Thanks also extend to my friends and coworkers and the Department of Chemical and Petroleum Engineering faculty and staff. I would like to thank the Computer Modelling Group (CMG) for providing the software, their help, and support for my study. Their support is appreciated.

Thanks also go to Crescent Point Energy for providing the data for conducting the analysis in this dissertation. I also appreciate support and help of the AER Core Research Centre staff.

I was supported financially by the members of the Tight Oil Consortium. The Graduate Recruitment Scholarship by Ursula and Herbert Zandmer family is appreciated.

Finally, I am grateful for the love and support of my family, spouse, and daughter. Their sacrifice during the course of this study is greatly appreciated. I am also thankful to my elder brother Famil Garayev and his family for their strong support.

Dedicated to my Grandfathers Mirza Mirzayev and Hüseyn Allahverdiyev

TABLE OF CONTENTS

ABSTRACT II

ACKNOWLEDGMENTS IV

TABLE OF CONTENTS VI

LIST OF TABLES VIII

LIST OF FIGURES X

NOMENCLATURE XVII

CHAPTER 1 : INTRODUCTION 1
1.1 Interwell Connectivity Estimation in Tight Reservoirs 1
1.2 Model Application Challenges in Tight Reservoirs 2
1.3 Research Objectives 4
1.4 Thesis Organization 4

CHAPTER 2 : LITERATURE REVIEW AND CONNECTIVITY EVALUATION IN LOW PERMEABILITY CASES 6
2.1 IWC Methods – Strengths and Weaknesses 6
2.2 Capacitance Model and its Application 13
2.3 Common Challenges in Tight Reservoirs during Model Application 20

CHAPTER 3: MODIFIED CAPACITANCE MODEL CM-PW 22
3.1 Introduction 22
3.2 Model Development and Validation 22
3.2.1 Testing the CM-PW with Vertical wells 27
3.2.2 Testing with Horizontal Wells 39
3.2.2.1 CM-PW Performance during Early Flow Period 43
3.3 Conclusions 47

CHAPTER 4: DETERMINING WINDOW SIZE FOR THE CM-PW 48
4.1 Introduction 48
4.2 Use of heat equation analogy to reservoir parameters and analysis of key parameters 48
4.2.1 Vertical wells 49
4.2.2 Horizontal wells 56
4.3 Procedure for determining window size for the CM-PW application 58
4.4 Conclusions 64

CHAPTER 5: FIELD CASE STUDY OF THE HALO OIL FIELD EAST PEMBINA: CARDIUM FORMATION 66
5.1 East Pembina Field Description and Geology 71
5.2 IWC Evaluation in Selected Window Areas 72

5.2.1 Window 1 74
5.2.1.1 Optimum window size for the CM-PW application 74
5.2.1.2 CM-PW Analysis 78
5.2.2 Window 2 83
5.2.2.1 Optimum window size for the CM-PW application 83
5.2.2.2 CM-PW Analysis 85
5.3 Discussion 91
5.4 Conclusions 93

CHAPTER 6 INTERWELL CONNECTIVITY SURFACE PLOTS 95
6.1 Model and Parameters to be Tested 95
6.2 Automation of Model: Model linking CMG and CM-PW 97
6.3 Analysis of IWC Surface Plots 98
6.4 Conclusions 106

CHAPTER 7 : BAKKEN FORMATION WATERFLOOD CASE STUDY 107
7.1 Field Description and Geology 107
7.2 Connectivity Maps and Analysis 111
7.2.1 Window size calculation in the tracer test area 111
7.2.2 Connectivity maps 115
7.2.3 Comparison of CM-PW results with tracer tests 119
7.2.4 Integration of connectivity, seismic, and geological information 121
7.3 Discussion 127
7.4 Conclusions 131

CHAPTER 8: CONCLUSIONS AND RECOMMENDATIONS FOR FUTURE WORK 133
8.1 Conclusions 133
8.2 Recommendations for future work 135

REFERENCES 138

APPENDICES 144
Appendix 1: Testing simulation model flowrates for optimum grid size 144
Appendix 2: R_ε plots of injectors in the tracer test area from the Forget North pilot area. 147
Appendix 3: Copyright Forms 151

LIST OF TABLES

Table 2.1 Dynamic data based methods to infer injector-producer connectivity 10

Table 2.2 Strengths and weaknesses of the pressure based methods..... 11

Table 2.3 Strengths and weaknesses of the flow rate based methods..... 12

Table 3.1 Reservoir and fluid data used for the semi-homogeneous 5x4 model..... 27

Table 3.2 Case 3-3 R^2 and RMSE (root mean-squared error) of predicted rates of wells..... 33

Table 3.3 Reservoir and fluid data used for the Case 3-4 homogeneous 5x4 model..... 35

Table 3.4 P01 Hydraulic fracture properties..... 35

Table 3.5 Reservoir and fluid data used for the homogeneous 3x4 model..... 40

Table 3.6 Hydraulic fracture parameters 41

Table 3.7 Coefficients of determination, R^2, of Cases 3-5, 6, and 7, measuring agreement of simulated vs. CM-PW predicted production..... 43

Table 4.1 Model parameters used for diffusivity estimation..... 51

Table 4.2 Reservoir Simulation model parameters..... 60

Table 5.1 Lithofacies in Cardium Formation (Krause et al., 1987)..... 69

Table 5.2 Subfacies of main lithofacies (Krause et al., 1987) 69

Table 5.3 Some important East Pembina Field reservoir and fluid properties (Clarkson and Pedersen, 2011)..... 74

Table 5.4 Window 1 periods – R^2 values based on total predicted vs total measured production rates during each period..... 78

Table 5.5 Window 2 – R^2 values of total predicted vs total measured production rates during each period. 86

Table 6.1 Reservoir and fluid data used for the homogeneous 1x2 model..... 95

Table 6.2 λ_1s as I02 frequency changes for various diffusivities 100

Table 7.1 Frequency and amplitude of injectors from the tracer test area..... 113

Table 7.2 Injectors' distance of influence at $R_{\varepsilon\ crit.} = 3.4*10^{-12}$. 115

Table 7.3 Wells inside windows and R^2 (predicted vs measured total rate match) of windows. The tracer test area is divided into 3 smaller windows to include producers within the median distance of influence determined in Section 7.2.1. The large R^2 values suggest that the model can predict measured total rate with good accuracy. 118

Table 7.4 Wells inside windows and R^2 (predicted vs measured total rate match) of windows. 118

Table 7.5 Most likely causes of the connection between non-offsets well pairs. $\lambda > 0.1$ used as a connectivity threshold 131

LIST OF FIGURES

Figure 1.1 Timeline of a sample window area with 6 wells from the East Pembina Field 3

Figure 1.2 CM-predicted vs measured rates plot of two wells, Producers 9 and 16, from an area chosen from the East Pembina Field 4

Figure 3.1 Working algorithm of the model (λ for each injector-producer pair, τ for each producer) 24

Figure 3.2 Schematic drawings showing a sample window and a pseudo well accounting for flux imbalance; (A): Horizontal wells, (B): Vertical wells. Edited from Mirzayev and Jensen (2016) 26

Figure 3.3 Case 1-1 5x4 semi-homogeneous model with producers stimulated (-2 skin) by an enhanced near well region (10 md); production and injection wells are denoted by P and I, respectively. 28

Figure 3.4 Case 3-1 injection and production rates (sampled every 3 months)..... 28

Figure 3.5 Case 3-1 Left figure: CM-PW values (λ, shown with a line indicating the direction and the magnitude of connectivity) from the model with the pseudo well (I05). Right figure: The pseudo well is placed in the center of the map where only producers are shown. 29

Figure 3.6 Case 3-1 CM-predicted total rate vs simulator-based total rate ($R2 \geq 0.99$) – Pseudo well: I05..... 30

Figure 3.7 Case 3-1 connectivities from the case with I05 excluded vs. connectivities from the case I05 included..... 30

Figure 3.8 I05 not included history match plots from the CMP (left) & the CM-PW (right) 31

Figure 3.9 Case 3-2 λ maps of the model when P04 and I05 are removed. Additionally, the pseudo well connectivities are shown in the figure on right. 32

Figure 3.10 CM-predicted total rate vs measured total rate ($R^2 > 0.98$) – P04 and I05 removed from the model..... 32

Figure 3.11 Connectivities from the Case 3-2, where P04 and I05 are removed vs. connectivities from the case where all wells are included – low permeability model. 33

Figure 3.12 Case 3-3 CM-PW estimated λs with P01 shut-in are in good agreement with the λs obtained without the shut-in condition. 34

Figure 3.13 5x4 Heterogeneous model with producers stimulated (-2 skin)/fractured; production and injection wells are denoted by P and I, respectively. There are two barriers, one between P02 and I04 and the other between P01 and I02. 35

Figure 3.14 (a) injection rates (sampled quarterly), (b) production rates (sampled quarterly)..... 37

Figure 3.15 Connectivity map of the heterogeneous case with matrix permeability of 0.1md (*HF: hydraulic fractures)..... 37

Figure 3.16 Model prediction plot. 38

Figure 3.17 Sinusoidal injection rates of I02 and I04. Rates have amplitude of 30 and f = 0.317 cycle/years. They are also phase shifted to prevent collinearity. 38

Figure 3.18 Connectivity map of the heterogeneous case with matrix permeability of 0.1md and I02 and I04 with greater low-frequency (*HF: hydraulic fractures) 39

Figure 3.19 Simulation model with 7 horizontal wells; 3 injectors and 4 producers 40

Figure 3.20 Injection (left) and production (right) rates of the 3x4 model (rates sampled every 3 months) 41

Figure 3.21 Injector3 – not in the CM-PW model (Case 3-5 – left) and Producer3 – not in the model (Case 3-6 – right) 41

Figure 3.22 Case 3-7 connectivities from the case Injector1 and Producer4 – not in the model vs. connectivities of all wells included case 42

Figure 3.23 Schematic view of the heterogeneous model having 2 horizontal producers and an injector..... 44

Figure 3.24 λs from the first 8 months to 96 months intervals 45

Figure 3.25 τ-ratio from 8 months to 96 months intervals..... 45

Figure 3.26 Injection rate of the injector with revised injection rates, which are similar values to the Bakken Field example described later. 46

Figure 3.27 λs from two cases; different injection rate (left) and area doubled (right) 47

Figure 3.28 τ-ratios from two cases; different injection rate (left) and area doubled (right)..... 47

Figure 4.1 A schematic view of the 2x1 model 49

Figure 4.2 Emittance ratio R_ε versus interwell distance plot 51

Figure 4.3 The R_ε ratio for D = of 21097 and 2109.7md*psi/ cp versus interwell distance..... 52

Figure 4.4 The R_ε plot for different diffusivities 53

Figure 4.5 R_ε ratio for frequencies of 1 and 2 cpm versus interwell distance plot 53

Figure 4.6 For D=211 md*psi/ cp, the R_ε plots for the frequency range of 0.1 and 1 cycle per month (cpm) 54

Figure 4.7 R_ε ratio plot for k=1μd (D=21.1E-3 md*psi/ cp) 55

Figure 4.8 For vertical wells, the R_ε ratio for diffusivity range of 2109.7 to 42194.1 md*psi/ cp. 55

Figure 4.9 R_ε plots for diffusivity range of 21.1 and 42194.1 md*psi/ cp 57

Figure 4.10 For D = 21.1 md*psi/ cp, R_ε plots for frequency range of 0.1 and 1 cycle per month (cpm) 57

Figure 4.11 For horizontal wells, the R_ε ratio plots for diffusivity range of 2109.7 and 42194.1 md*psi/ cp. 58

Figure 4.12 Schematic view of a homogeneous simulation model with an injector and..... 60

Figure 4.13 Injector1 sinusoidal injection rate with f=1/3 cpm 61

Figure 4.14 λ vs IWD plot 61

Figure 4.15 Corresponding IWD at $\lambda_{cut\ off}$ = 0.1. IWD = 1080 ft. 62

Figure 4.16 Area Rε plot. The critical Re at IWD = 1080ft 62

Figure 4.17 Injector1 Rε plot. For the critical $R_\varepsilon = 2.0*10^{-16}$, IWD = 1857ft 63

Figure 4.18 λ vs IWD plots when noise added to production rates. The model fails when 40% noise added to production rate. λs are zero for all IWDs. 64

Figure 5.1 Map of Western Interior Seaway from the North America Continent before 89 MA. The current border of Alberta is shown with red dashed lines. Figure adapted from Blakey (2017). 66

Figure 5.2 Cardium Formation paleogeographic maps: a. Lower Cardium formation, b. Middle Cardium Formation, c. Upper Cardium Formation (Modified from Krause et al., 1994). 67

Figure 5.3 Cardium Formation stratigraphic subdivisions in the subsurface (Modified from Krause et al., 1994) 68

Figure 5.4 (A) Alberta map showing Cardium Formation paleogeography (Modified from Krause et al. (1994) as cited in Fic, 2013) and (B) Enlarged map of the East Pembina Oil Field well locations. 71

Figure 5.5 Conglomerate thickness map of the East Pembina Oil Field (Edited from Krause et al., 1994). Conglomerate thickness varies from 0.1 to 9 meters in this area. Contours are in meters: 0.1, 1.0, 3.0, and 9.0. 72

Figure 5.6 The East Pembina Oil Field – conglomerate thickness map (edited from Krause et al. 1994); Contours are in meters: 0.1, 1.0, 3.0, and 9.0. Orange colored outlines are the chosen window areas. 73

Figure 5.7 FFT periodogram of I40 injection rate 75

Figure 5.8 I18 and I37 FFT periodograms 76

Figure 5.9 Schematic view of a homogeneous simulation model with one injector and 5 producers. The model permeability is 0.7 md. 77

Figure 5.10 Corresponding IWD at λcut off = 0.1 77

Figure 5.11 Timeline of the Window I40-I37-I18 78

Figure 5.12 Window 1 – normalized connectivity map of the first period. Connectivities are larger in the NE-SW direction, consistent with the direction of larger horizontal principal regional stress. 79

Figure 5.13 Pseudo well connectivity during first period, showing strong connectivity from wells outside the area with well P127. 80

Figure 5.14 Window 1 – normalized connectivity map of the second period (P128 abandoned, P145 refractured in 1977) 81

Figure 5.15 Window 1 – normalized connectivity map of the third period (P145 fractured, P128 abandoned) 82

Figure 5.16 Cumulative injected volume with respect to time for injection well I40 (the numbers 1, 2 and 3 show the corresponding periods). 82

Figure 5.17 I62 FFT Periodogram showing the most significant low-frequency peak and its corresponding frequency value 83

Figure 5.18 Corresponding IWD at λcut off = 0.1 84

Figure 5.19 Area R_ε plot. The critical R_ε at IWD = 3600 ft 84

Figure 5.20 I62 Rε plot. For the critical Rε = 0.0001297, IWD = 3774 ft 85

Figure 5.21 Window 2 location and its proximity to significant conglomerate thicknesses. 86

Figure 5.22 Window 2: well treatment timeline (I62 and P 219 were intermittently suspended) 86

Figure 5.23 Window 2 – 1st Period –connectivity map where P224 and P219 are fractured (the plot in the lower right corner shows pseudo well connectivity). 87

Figure 5.24 λ' vs $k_{max}h$ for the initially unfractured wells P184 and P225; the connectivities are consistent with the well flow capacities. 88

Figure 5.25 Window 2 – the connectivity map after acid squeezing and fracturing P225 (2nd Period) 89

Figure 5.26 Pseudo well connectivity during the 2nd Period shows largest connectivity with P219 the east. 89

Figure 5.27 Change in connectivity, Δλ′, vs proppant tonnage suggests a linear relationship, where the point at the origin is added from physical reasoning. 90

Figure 5.28 Window 2: Connectivity map during the 3rd Period 90

Figure 5.29 Pseudo well connectivity during the 3rd Period 91

Figure 6.1 2x1 model - Producer surrounded by two injectors 96

Figure 6.2. Sample sinusoidal injection rate with amplitude A = 200 rb/day and f = 1 cycle per month 97

Figure 6.3 The workflow of the Matlab script. 98

Figure 6.4 2x1 semi-heterogeneous model having a barrier between I02 and P01 100

Figure 6.5 (-A-): Surface plot of $10*(\lambda_1/\lambda_2)$ when I02 frequency and diffusivity change. We multiplied the ratio by 10 to magnify the values. (-B-): same surface plot as in (-A-) with diffusivity in reverse order to show backside of the surface plot. 101

Figure 6.6 λ_1, λ_2 plots as I02 frequency changes, when D = 2.0E+06 md*psi/ cp 102

Figure 6.7 For D = 2.0E+06 md*psi/ cp, Emittance ratio plots for frequency range of 2 and 12 cpm 102

Figure 6.8 Producer P01 tau surface plot as I02 frequency and Simulation model diffusivity change 104

Figure 6.9 Producer P01 tau surface plot as injection signal amplitude in both injectors and Simulation model diffusivity change 104

Figure 6.10 λ_1 Surface plot in case of Semi-heterogeneous scenario (Figure 6.4) 105

Figure 6.11 λ_2 Surface plot in case of Semi-heterogeneous scenario (Figure 6.4) 105

Figure 6.12 Heterogeneity-ratio Surface plot of λ in case of Semi-heterogeneous model (Figure 6.4) 106

Figure 7.1 A. The Viewfield Bakken oilfield location (dashed circle) (modified from the CanadianOilStocks, 2015). B. Local stratigraphic column with well log responses, with Unit A being the main reservoir; Unit B is absent in the Forget North area (Edited from Cronkwright, 2017). 108

Figure 7.2 Wells from the Forget North area in Township 8, Range 7 W2M shown with red color (recently, a few infills have been added to the area and are not included in the analysis; Accumap, 2015) 109

Figure 7.3 A N-S core cross section through the Viewfield Bakken oilfield (From personal communication with D. Cronkwright). 110

Figure 7.4 Structure map of the top surface of Unit A of the Bakken Forget North pilot study area. The map was produced using horizontal gamma ray logs, and picking the interface between Unit A and the overlying Unit C contoured using kriging (From personal communication with D. Cronkwright). 111

Figure 7.5 Producer based tracer arrival times and concentrations shown with three colors: blue, green, red. Tracers were placed in the southernmost 3 injectors (Courtesy of CPE). 112

Figure 7.6 Schematic view of a homogeneous simulation model with an injector and 5 producers 113

Figure 7.7 Corresponding interwell distance at $\lambda_{cut\ off}$ = 0.1. IWD = 1080 ft. 114

Figure 7.8 Area Rε plot. The critical R_ε at IWD = 1080ft. $R_\varepsilon = 3.4*10^{-12}$ 114

Figure 7.9 Timeline of the wells used for the tracer test (tracer test: March 23, 2011)..... 116

Figure 7.10 Connectivity map of the tracer test area. Each blue horizontal line represents one of the horizontal wells. The dashed lines originating from injectors connect injector-producer pairs. Solid red lines show the magnitude of a connection (λ) by their length. The connectivity between offset pairs is shown with an order that the wells are introduced to the model. 117

Figure 7.11 Connectivity maps of other windows from the Forget North pilot area..... 119

Figure 7.12 Percent of tracer samples at producers B14, B12 and B10 (B9-inj: HTO – tritiated water, B11-inj:TIPA – tritiated isopropyl alcohol, B13-inj:C14-MeOH – methanol with C14)..... 120

Figure 7.13 Percent of tracer vs λ. Pairs above the orange line are assumed to be connecting via fracture hits. The operator found a direct fracture connection between B9-Inj and B10. Tracer percentages at producers B14, B12 and B10 reveal strong levels of connection with injectors B13-inj, B11-inj and B9-inj, respectively. IWC is subject to statistical variation: λ ± 0.1. Due to this variation, there might be a pair with relatively strong connection which received a negligible amount of tracer (e.g., B12:B13-Inj). 121

Figure 7.14 Seismic basemap with the wells which are used in the connectivity analysis. 122

Figure 7.15 Curvature attribute map-azimuth at maximum dip attribute with possible sub-seismic faults/fractures or barrier shown with the dashed lines. The color scale indicates the azimuth value at maximum dip of the seismic horizon in the reservoir. 123

Figure 7.16 The average relative acoustic impedance over the reservoir interval. The color key is normalized and the higher values are masked and shown in light color. The lower values of relative acoustic impedance are purple..... 124

Figure 7.17 A seismic section of relative acoustic impedance volume in direction of A-B which is shown in the basemap (top right). The arrow on the left shows the reservoir zone. 125

Figure 7.18 Division of the target area to 7 zones. 126

Figure 7.19 A comparison between the average relative acoustic impedance in the area between wells and IWC. $R^2 = 0.72$ and the regression line slope is non-zero at the 0.017 level of probability. 126

Figure 7.20 Maximum AI vs connectivity of non-neighboring wells shows a “threshold” behavior..... 127

Figure 7.21 Horizontal cross section of Well B24 with the gamma ray log and deviation survey. 129

Figure 7.22 Water cut plot of B24. 129

Figure 7.23 Water cut plots of B10 and B14; the starting dates of the offset injectors shown. . 130

Figure 7.24 Water cut plot of B18; the starting dates of the offset injectors shown. 130

Figure 7.25 Average relative acoustic impedance vs connectivity plot revisited. The likely connection types are identified. 131

NOMENCLATURE

Symbol	Definition
C	= CM number
C_v	=Coefficient of variation
c	=specific heat, $mL^2t^{-2}T^{-1}$
c_t	= total compressibility, $m/(Lt^2)$
D	=diffusivity, L^2/t
f	= frequency, t^{-1}
I	= total number of injection wells
J	= well productivity index, $(L^4t^2)/m$
K	= total number of production wells
K*	= heat conductivity, $mLt^{-3}T^{-1}$
k	= permeability, L^2
L	= number of samples per model parameter
N	= total number of samples (time steps) in the analysis period
p_{wf}	= bottom-hole pressure of the producer, $m/(Lt^2)$
$p'_{wf\,kj}(t)$	= convolved BHP of producer k at the location of producer j at time step t, $m/(Lt^2)$
$\hat{q}(t)$	= predicted total production rate at time step t, L^3/t
q(t)	= measured total production rate at time step t, L^3/t
$q_j(t_0)$	= initial total production rate of producer j, L^3/t
$q_p(t)$	= pseudo well production rate at time step t, L^3/t
R^2	=coefficient of determination
R_ε	= emittance ratio
T	= temperature, T
w(t)	= measured total injection rate at time step t, L^3/t
$w'_{ij}(t)$	= convolved injection rate of injector i at the location of producer j at time step t, L^3/t
t_0	= time at the beginning of the window, t
t	= time
V_p	= pore volume, L^3

Greek symbols

λ	= interwell connectivity between an injector-producer pair
λ’	=normalized interwell connectivity between an injector-producer pair
μ	= viscosity, m/(Lt)
ν	= coefficient of producers’ bottom-hole pressure term in the CM
ν’	= temperature, T
ρ	=density, m/L^3

ω	= angular frequency, rad/t
τ	=time constant/time delay of producer, t

Acronyms	Definition
CM	Capacitance Model
CMIP	Capacitance Model with time constant per Injector-Producer pair
CMP	Capacitance Model with one time constant for each Producer
CM-PW	Capacitance Model – Pseudo Well
comseg-CM	compensated and segmented Capacitance Model
FFT	Fast Fourier Transform
IWC	Interwell Connectivity
IWD	Interwell Distance
RMSE	Root Mean Square Error

CHAPTER 1: INTRODUCTION

1.1 Interwell Connectivity Estimation in Tight Reservoirs

To produce oil found in low-permeability reservoirs in an economically feasible way is a challenge. Water injection might be one of the ways to deal with this challenge. Injectors are designed to maintain the reservoir pressure and sweep oil towards producers. Because of low permeability formations, the well spacings between an injector and a producer are smaller than the ones in conventional reservoirs. Although tight reservoirs have smaller well spacings, not all well pairs have connections with each other due to the heterogeneity in the reservoirs. Therefore, researchers are trying to develop methods which can evaluate heterogeneities in a reservoir.

Various models have been developed to mimic real field scenarios. However, the complexity of these models increases day by day. The more complex models require more inputs and more computational time. At the end of the day, all inputs and time cost money that researchers endeavor to minimize. Even models with complex geology, honoring detailed reservoir characterizations with no upscaling, involve some degree of uncertainty which can influence the reservoir management decisions in large scales. The uncertainties in the input data and their interactions may result in a fuzzy economic risk analysis result based on a numerical simulation model output and which could take months to attain. On the other hand, ignoring the heterogeneities may result in disappointing outcomes. So, the price paid at the end can be much higher than the investment in the model building stage.

The Capacitance Model (CM) is straightforward to use for estimating interwell connectivity (IWC) between an injector-producer pair, which requires injection and production data. Our analysis results show the CM is successful to evaluate IWC in tight reservoirs.

The connectivity parameters found with the CM are divided into two categories:

- injector-producer connectivity (IPC)
- producer-producer connectivity (PPC).

In most real field CM applications, wells are vertical or slightly deviated. Even though the CM is a zero-dimensional model, there has not been inter-horizontal well connectivity estimation for real field using the CM. This motivated us to apply it to the field developed with horizontal

wells. The Forget North Pilot from the Viewfield Pool is one of these fields, where we have applied a modified form of the CM with favorable results.

Many case studies show the CM can successfully predict production and identify flow channels and barriers in conventional reservoirs. The challenging task is to extend the CM to achieve estimating connectivity between injectors and producers in tight reservoirs. The fluid contained within these reservoir rocks does not naturally flow to the wellbore at economic rates without using advanced completion methods. These fields possess high well densities, which create the need to perform IWC evaluations over small areas. Dividing the field into subzones can create a problem in that wells within a subzone may be in communication with wells outside the subzone. The contribution of the outside wells can be significant and affect the IWC estimation.

In addition, we also want to investigate other parameters likely to affect the degree of IWC, which we name zero-type connectivity parameters after Kaviani (2009). These are the zero-type connectivity parameters:

- Injection signal frequency,
- Injection signal amplitude.

1.2 Model Application Challenges in Tight Reservoirs

The CM has been tested in numerous conventional fields where the CM results were found consistent with the geological and geophysical information acquired from the independent studies. When the model is used in real field applications, core assumptions must be met to estimate connectivity parameters representing the nature of well-to-well and near well heterogeneities:

- Constant producer productivity indices (no well treatment, near-unit mobility ratio etc.)
- Instantaneous equilibrium in the control volume (tank assumption)
- Slightly compressible fluid
- Constant number of producers
- Pseudo steady state flow.

Violating the constant productivity index assumption with well treatments makes the model underperform. Since the wells in tight reservoirs are treated frequently, choosing an appropriate period to perform connectivity analysis becomes very challenging. For example, in a small area with a few wells, selecting periods where little or no change occurs can be problematic (**Figure 1.1**), which makes the CM impractical to run for large unconventional fields without areal and time windowing (period).

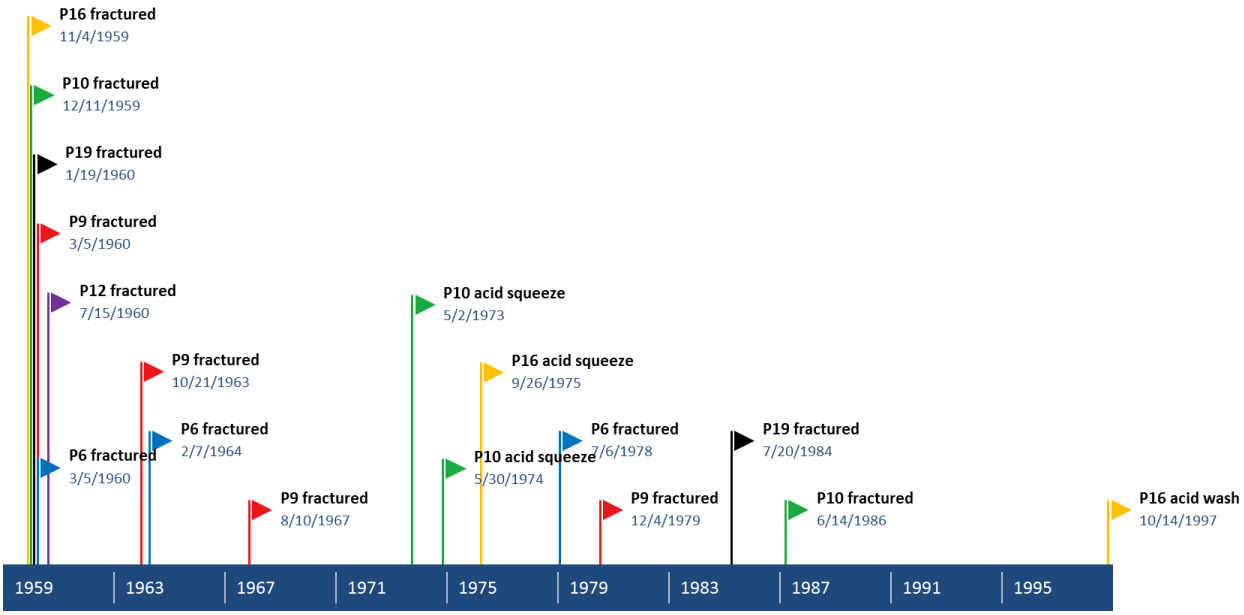

Figure 1.1 Timeline of a sample window area with 6 wells from the East Pembina Field

Wells located outside of the window area for IWC analysis may interact with the wells of interest. When we neglect the effect of the outside wells, the match between predicted and measured rates obtained with the conventional CM is poor: $(R^2)_{P16} = 0.33$, $(R^2)_{P9} = 0.34$ where R^2 is the coefficient of determination (**Figure 1.2**). The CM barely catches the trend between these rates. Most of the time, Cardium wells with low average rate have a poor correlation between the CM-predicted and measured rates.

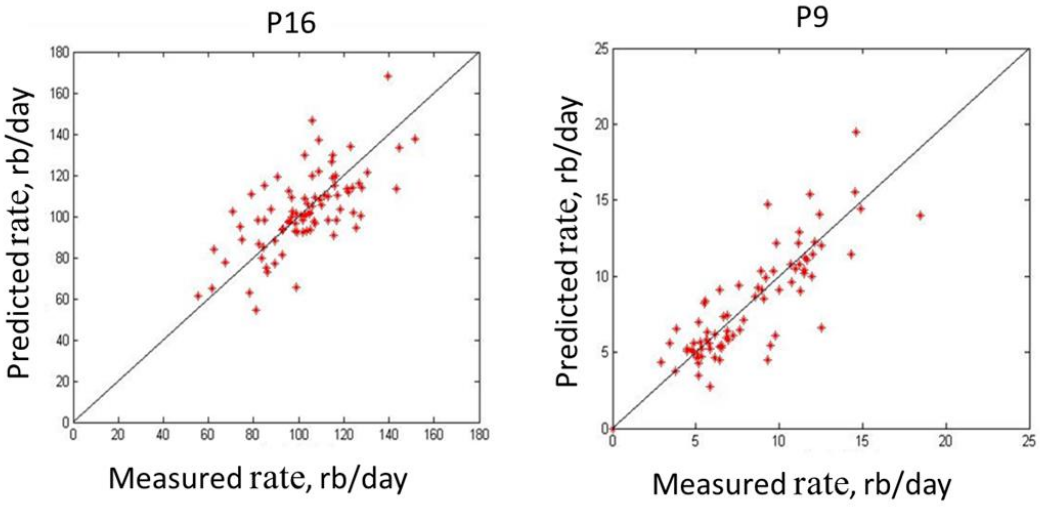

Figure 1.2 CM-predicted vs measured rates plot of two wells, Producers 9 and 16, from an area chosen from the East Pembina Field

1.3 Research Objectives

The objectives of this research study are:

Make the CM applicable to tight reservoirs. Specifically,

1. Explore limitations on the application of the CM in tight reservoirs
2. Inter-HW connectivity evaluation with the CM
3. Analyze the effect of the transient flow period in IWC evaluation
4. Apply the CM to real tight oil reservoirs
5. Investigate zero-type parameter effects on IWC
6. Analyze the effect of aquifer on well communication
7. Study hydraulic fracture effect on IWC
8. Determine an optimum window size for the CM application.

1.4 Thesis Organization

The literature review is presented in Chapter 2. In Chapter 3, we discuss how the modified CM can evaluate IWC in case of imbalance in the system for vertical and horizontal well. Chapter 4 contains a determination of window size for the CM-PW. We use heat equations, analogy to

reservoir parameters, and analyze the effect of key parameters on injection well emittance rate. The field case study of the tight oil reservoir East Pembina is presented in Chapter 5. We evaluate IWC in selected areas from the field and study the effect of a conglomerate layer on IWC. We also estimate optimum window size for the CM-PW application. The effect of hydraulic fracturing on IWC is analyzed. The CM-PW results are used to investigate lateral continuity in the field. In Chapter 6, we generate IWC surface plots of changing diffusivity and injection signal frequency. The CM-PW is linked with the CMG IMEX © to make the process automated, which gives us a chance to run more than 100 simulation runs for a specific surface plot to better understand the behavior of the CM-PW estimates. The work in Chapter 7 is primarily based on the journal paper entitled "Determining well-to-well connectivity using a modified capacitance model, seismic, and geology for a Bakken Waterflood" but with updated and expanded results. I am lead author and Riazi, N., Cronkwright, D., and others are co-authors. Dr. Riazi did the seismic interpretation. Cronkwright prepared Figures 7.1 – B, 7.3, 7.4 and 7.22 and parts of Section 7.1 text. Cronkwright and Dr. Pedersen helped respond to the reviewers' concerns regarding the Bakken geology. We evaluate IWC of horizontal wells and compared them with the tracer test results. The effect of the Lodgepole Formation aquifer on IWC is studied. We also integrated IWC with the results of seismic interpretation and known geology.

Finally, Chapter 8 – our wrap-up consists of conclusions and recommendations for future work.

CHAPTER 2: LITERATURE REVIEW AND CONNECTIVITY EVALUATION IN LOW PERMEABILITY CASES

Well rate fluctuations are vital sources of information to better understand reservoir behavior. Various methods have been presented in the literature to analyze flow rate measurements and characterize the reservoir during waterflooding. In particular, identifying the degree of communication between an injector and a producer (IWC) aids reservoir management. For example, connectivity information can help us to reduce water recycling, predict future production, and identify geological features controlling fluid flow.

Numerical simulators inherently evaluate IWC but they require a geological model. To build the geological model employing all the needed data, however, often demands considerable scientific judgment and effort. Instead, a simple input-output model, the Capacitance Model (CM or CRM in some reports), can estimate IWC using flow rates and bottom-hole pressures, BHPs, if available.

The CM has been used to analyze flow rates to measure IWC. Numerous case studies show the CM can successfully predict production and identify flow paths and barriers in conventional reservoirs (Weber, 2009; Yousef et al., 2006; Soroush, 2014; Sayarpour, 2008; Liang et al, 2007; Kaviani and Jensen, 2010).

A signal sent from an injector takes a long time to reach a producer in tight formations. The attenuated signals make the optimization problem in the CM difficult to obtain IWC estimates that are not misleading. Thus, the stability of the model parameters is a concern. The unstable results cause a poor match between predicted and measured rates. In addition to the effect of the attenuated signals, the variable imbalance and fluid compression in the chosen area can be the potential cause of the problem.

2.1 IWC Methods – Strengths and Weaknesses

Stable and physically meaningful IWC estimates are a useful source of information for reservoir management. IWCs can be utilized to determine a proxy function which can be an alternative to geological realizations.

Exploiting available dynamic and/or static data to infer injector-producer connectivity is an important task, which has been studied for years. Many methods have been developed to evaluate

IWC; however, the field applicability of most methods is not feasible because of their limitations. For example, skin change, well shut-in, and adding new well are some of these limitations. On the other hand, some old methods, such as tracer tests, are time-consuming and costly. In this literature review, some of the dynamic data-based connectivity approaches are presented.

Johnson et al. (1966) presented pulse-testing for evaluating transmissibility (kh/μ) and storage (ϕch) between wells. Pulse-testing uses a sensitive pressure gauge, which can measure pressure with a sensitivity of around 0.001 psi. Pulses created at a nearby well will not take more than several hours to be measurable in an observation well. The method is applicable during unsteady state period and accounts for compressible-flow. The authors applied the pulse-testing to more than 25 reservoirs and observed that the cases with time lags higher than 1000 minutes are not practical to apply. The testing capability of the method is limited to a certain value of transmissibility and or storage because the attenuated response should not be lower than the detection level.

Later, Stewart et al. (1984) highlighted the necessity of considering the effect of barriers on the pressure response at the observation well. They used interference testing to analyze the effect of sealing and non-sealing fault planes on the test response and estimate rock-fluid properties from the region near to a well or between wells. In the sealing fault case, systems of intersecting and parallel faults were examined employing the method of images. The reservoir parameters kh/μ and $\phi\mu c_t$ are estimated using implicit function theory (IFT). The IFT determines the unknown coefficients of parabolic and elliptic partial differential equations from defined boundary conditions. The main drawback of the IFT is that it cannot estimate more than two unknowns. In the partially communicating fault case, a 2-D single-phase numerical simulator was utilized to investigate the effect of the partially sealing fault between wells. Log-log type curves were created for different fault conductivity values. For the faults with low transmissibility, the method requires long testing time, which raises cost concerns.

Some researchers have preferred statistical methods to analyze flow rates to qualitatively measure connectivity between wells. Jansen and Kelkar (1997) observed that calculating the cross-correlation of flow rates between pairs of wells to obtain information about the flow path in a reservoir can be problematic. They offered the non-linear and non-stationary nature of the interwell relationship as reasons. Instead, they presented the wavelet transformation to decompose the

production data into a combination of high-frequency and smoothed components. The time localizing capability of the transformation is employed to create a robust and time-dependent cross-correlation between pairs of wells. Then, they proposed to use this cross-correlation to appraise the degree of IWC and to determine preferential flow paths and flow barriers. The applicability of the method is controlled by the sampling rate and a number of data points, which limits the number of frequencies. Furthermore, the interference of injection rates from several wells diminishes the capability of the approach.

Soeriawinata and Kelkar (1999) defined the effect of the superposed injectors on the producer as constructive or destructive, which removes the limitation of the interaction of injection rates on the cross-correlation method of Jansen and Kelkar (1997). Using the Spearman rank cross-correlation between injectors and producers and an arbitrary threshold value for it, an injector is chosen with the highest cross-correlation with the selected producer among all the nearby wells. Then, the approach looks for an injector that contributes the highest improvement in cross-correlation. At the end, the method finds if there exists an injector or a set of injectors showing a connection with the selected producer.

Another statistically based method, a neural-network, was used by Demiryurek et al. (2008) to determine injector-producer relationships. They created a neural network to define the mapping function between each producer and the adjacent injectors based on the injection and production data. To train the three-layer feed-forward neural network using real data, they utilized the Back-Propagation-Through-Time learning algorithm. Then, the generated neural network model was applied to analyze sensitivities for quantifying the effect of the injectors on the corresponding producers. They observed that the method gives better results when the size of the training dataset gets larger.

An analytical approach was introduced to evaluate the pair-wise injector-producer (IP) relationships (Khodaei et al., 2009). They used the Mutual Information (MI) data mining tool to design the proposed metric to include the non-linearity of the IP relationship between the injection and production rates. In addition to considering the non-linear aspect of the IP relationship, their metric accounts for the distance between the IP pair and their relative injection and production rates. To identify underperforming producers, the model uses 3 parameters: barrels of oil per day

(BOPD), water oil ratio (WOR), and gas oil ratio (GOR). The change in these parameters between two consecutive months and GOR are tested with user-defined thresholds (a, b, c, and d):

$\Delta BOPD < a$
$\Delta WOR > c$
$\Delta GOR > b$
$GOR \geq d$.

Using the same thresholds for compartmentalized reservoirs can give misleading results.

Ghori and Heller (1998) theoretically generated a catalog of tracer production curves for different sets of geostatistical parameters for five-spot flooding patterns. They obtained quantitative information about the permeability heterogeneity of the reservoir area between an injector and a producer. Moreover, they did experimental work in which tracer concentrations were measured at the production well. The minipermeameter-measured permeabilities were used as an input into the simulator and the numerical production curves were compared with the experimental ones. They found that with the tracer output curves, one could estimate geostatistical parameters of field permeability (e.g., permeability semivariogram).

Instead of flow rate, using the bottomhole pressure for connectivity evaluation can be an alternative way to estimate IWC. Dinh and Tiab (2008) extended their technique (Dinh and Tiab, 2007) which determines IWC in a reservoir based on fluctuations of bottomhole pressure of both injectors and producers during waterflooding. They used a constrained multivariate linear regression analysis to get useful information about permeability trends, channels, and barriers. Their model is applicable for fully penetrating vertical wells in a closed rectangular reservoir. The model can detect reservoir compartmentalization. They analyzed different synthetic reservoir models, such as homogeneous, anisotropic reservoirs, reservoirs with high permeability channel, partially sealing and sealing faults. Compared to flow rate data, pressure data are not abundant in real field examples, which makes the model impractical. In low permeability formations, it may be difficult to differentiate real BHP perturbations from noise.

Kaviani and Valkó (2010) evaluated IWC using the multiwell productivity index (MPI). In their study, the MPI was formulated to assess waterflood performance in a homogeneous reservoir. It can estimate the liquid rates, average reservoir pressure, and injector bottomhole pressures. Moreover, using the injection and production data, the model predicts the normalized IWCs for

heterogeneous systems. This method is not reliant on operational conditions, such as well shut-ins, reallocating wells etc. The model was validated successfully with various homogeneous and heterogeneous cases.

Some researchers have used streamline-based methods to evaluate IWC (Thiele and Batycky, 2006; Izgec and Kabir, 2009). Thiele and Batycky (2006) introduced dynamic well allocation factors (WAFs) between injector and producer, which are generated by the streamline simulator. To quantify and visualize reservoir flow, their model requires well positions and rates, geological description and continuity, relative permeability, and fluid properties.

We introduce and discuss the CM separately, in Section 2.2.

In summary, we can divide dynamic data based methods into two groups; pressure based methods and flow rate based methods (**Table 2.1**). Furthermore, we can summarize some of the weaknesses and strengths of these methods (**Tables 2.2 and 2.3**).

Table 2.1 Dynamic data based methods to infer injector-producer connectivity

Pressure based methods	Flow rate based methods
• Pulse-testing • Interference testing • BHP-based Connectivity	• Wavelet transformation • Artificial Neural Network • Capacitance Model • Spearman Rank Correlation

Table 2.2 Strengths and weaknesses of the pressure based methods

Method	Strengths	Weaknesses/limitations
Pulse-testing	- measure pressure with a sensitivity of around 0.001 psi - account for compressible-flow	- Not practical to use when the time lag is greater than 1000 minutes. - Limited to a certain value of transmissibility and or storage.
Interference testing	- Fault transmissibility can be estimated - distance from the active well to a fault can be found	-In low transmissibility cases, it requires long testing time, which makes it costly.
BHP-based connectivity models	- can detect reservoir compartmentalization - can forecast field production rate	- Producer BHPs should be recorded, which is not common in many fields. - In tight reservoirs, it is difficult to differentiate between injector and producer caused BHP perturbations.

Table 2.3 Strengths and weaknesses of the flow rate based methods

Method	Strengths	Weaknesses/limitations
Wavelet transformation	- Employs frequency content of flow rates to estimate the degree of IWC	- Sensitive to the sampling rate and number of data points - Interference of injection rates makes it hard to apply
Artificial Neural Network	- Can be used to analyze sensitivity for quantifying the effect of injectors on the corresponding producers - Can predict production rates	- Requires large size of the training dataset - Ignore effects of production well treatment/maintenance on the injector-producer pair relationship
Capacitance Model	- Can exploit both pressure and flow rates - Incorporate time delay - Can be coupled with fractional flow models to calculate oil rate and optimize it.	- In low diffusivity constant cases, it might get stuck in local minima, which can give spurious results. - Violating core assumptions causes deviation from true values
Spearman Rank Correlation	- Only cross-correlations between well pairs are estimated. - Simple to apply	- Determining the cross-correlation threshold values is challenging. - Ignores events in well history. e.g., skin change, well shut-ins.

2.2 Capacitance Model and its Application

Yousef et al. (2006) proposed the CM (sometimes called the Capacitance-Resistance Model, or CRM) to quantify communication between vertical wells in a reservoir on the basis of fluctuations in flow rates. The CM, nonlinear in the capacitance parameter, provides valuable information about flow trends and barriers in a reservoir. The authors introduced a time constant (τ), which depends on pore volume, compressibility, and productivity index, to characterize the time lag of the injection signal to producers. The distance between wells and the filtering property of the porous medium cause the attenuation of signals. To account for the attenuation and time delay, τ is employed. The τ value is related with the distance between an injector-producer pair. Moreover, τ increases as the system becomes more compressible. Low permeability also amplifies the time constant, because decreasing permeability decreases the productivity index (J) and, in turn, tau increases.

Yousef et al. (2006) coupled material balance, Eq. (2-1), with a linear productivity model, Eq. (2-2).

$$c_t V_P \frac{d\bar{p}}{dt} = w(t) - q(t) \quad \ldots (2\text{-}1)$$

$$q(t) = J\left(\bar{p}(t) - p_{wf}(t)\right) \quad \ldots (2\text{-}2)$$

where w (t) and q(t) are injection and production rates at time t, respectively. Replacing $\frac{d\bar{p}}{dt}$ in Eq. (2-1) with differentiated form Eq. (2-3) of the Eq. (2-2), we get

$$\frac{d\bar{p}}{dt} = \frac{1}{J}\frac{dq}{dt} + \frac{dp_{wf}}{dt} \quad \ldots (2\text{-}3)$$

$$\frac{C_t V_p}{J}\frac{dq}{dt} + C_t V_p \frac{dp_{wf}}{dt} = w(t) - q(t) \quad \ldots (2\text{-}4)$$

$\frac{C_t V_p}{J} = \tau$ is called time constant for the producer drainage volume. By reformulating the Eq. (2-4), it can be written as

$$\tau \frac{dq}{dt} + q(t) = w(t) - \tau J \frac{dp_{wf}}{dt} \qquad \ldots (2\text{-}5)$$

Dividing both sides with τ, the Eq. (2-5) becomes

$$\frac{dq}{dt} + \frac{1}{\tau} q(t) = \frac{1}{\tau} w(t) - J \frac{dp_{wf}}{dt} \qquad \ldots (2\text{-}6)$$

The left-hand side of the Eq. (2-6) is the first order differential equation that can be solved employing integrating factor technique

$$\mu(t) = e^{\int \frac{1}{\tau} dt} = e^{\frac{t}{\tau}}$$

We can multiply both sides of the Eq. (2-6) and write it in this form:

$$\frac{d}{dt}[e^{\frac{t}{\tau}} q] = e^{\frac{t}{\tau}}[\frac{1}{\tau} w(t) - J \frac{dp_{wf}}{dt}] \qquad \ldots (2\text{-}7)$$

Now we integrate both sides of the Eq. (2-7) with respect t,

$$[e^{\frac{t}{\tau}} q]_{t_0}^{t} = \int e^{\frac{t}{\tau}}[\frac{1}{\tau} w(t) - J \frac{dp_{wf}}{dt}]dt \qquad \ldots (2\text{-}7.1)$$

The Eq. (2-7.1) can be solved as follows

$$e^{\frac{t}{\tau}} q(t) - e^{\frac{t_0}{\tau}} q(t_0) = \int e^{\frac{t}{\tau}}[\frac{1}{\tau} w(t) - J \frac{dp_{wf}}{dt}]dt \qquad \ldots (2\text{-}7.2)$$

$$e^{\frac{t}{\tau}} q(t) - e^{\frac{t_0}{\tau}} q(t_0) = \int e^{\frac{t}{\tau}}[\frac{1}{\tau} w(t) - J \frac{dp_{wf}}{dt}]dt \qquad \ldots (2\text{-}7.3)$$

$$q(t) = q(t_0) e^{-\left(\frac{t-t_0}{\tau}\right)} + e^{-\frac{t}{\tau}} \int_{y=t_0}^{y=t} e^{\frac{y}{\tau}} \left(\frac{1}{\tau} w(y) - J \frac{dp_{wf}}{dy} \right) dy \qquad \ldots (2\text{-}7.4)$$

$$q(t) = q(t_0)e^{-\left(\frac{t-t_0}{\tau}\right)} + e^{-\frac{t}{\tau}} \int_{y=t_0}^{y=t} \frac{e^{\frac{y}{\tau}}}{\tau} w(y)dy - Je^{-\frac{t}{\tau}} \int_{y=t_0}^{y=t} e^{\frac{y}{\tau}} \frac{dp_{wf}}{dy} dy \qquad \ldots (2\text{-}7.5)$$

The Eq. (2-7.5) can be solved using integration by parts

$$q(t) = q(t_0)e^{-\left(\frac{t-t_0}{\tau}\right)} + e^{-\frac{t}{\tau}} \int_{y=t_0}^{y=t} \frac{e^{\frac{y}{\tau}}}{\tau} w(y)dy + J\left(p_{wf}(t_0)e^{-\left(\frac{t-t_0}{\tau}\right)} - p_{wf}(t) + \frac{e^{-\frac{t}{\tau}}}{\tau} \int_{y=t_0}^{y=t} e^{\frac{y}{\tau}} p_{wf}(y)dy \right) \qquad \ldots (2\text{-}7.6)$$

The Eq. (2-7.6) can be generalized for multiple injectors and producers by applying superposition in space and discretization of the integrals, which is

$$\hat{q}_j(t) = \lambda_{pj} q_j(t_0) e^{-(\frac{t-t_0}{\tau_{pj}})} + \sum_{i=1}^{i=I} \lambda_{ij} w'_{ij}(t) + \sum_{k=1}^{k=K} v_{kj} \left(p_{wf\,j}(t_0) e^{-(\frac{t-t_0}{\tau_{kj}})} - p_{wf\,j}(t) + p'_{wf\,kj}(t) \right) \qquad \ldots (2\text{-}7.7).$$

The CM estimates three coefficients for each injector-producer pair: λ, showing the magnitude of the connectivity; τ, expressing the fluid storage in the interwell region and time delay; and ν, quantifying the effects of producer BHPs (Eq. 2-7.7).

$$\hat{q}_j(t) = q_{PP} + q_{WFP} + q_{BHP} \qquad \ldots (2\text{-}7.7a)$$

q_{PP} – primary production

q_{WFP} – waterflooding production

q_{BHP} - bottomhole pressure change-induced production

where $\hat{q}_j(t)$ is the predicted total production rate of producer j, $w'_{ij}(t)$ and $p'_{wf\,kj}(t)$ are

$$w'_{ij}(t) = \sum_{m=1}^{n} \left(e^{\left(\frac{t_m - t}{\tau_{ij}}\right)} - e^{\left(\frac{t_{m-1} - t}{\tau_{ij}}\right)} \right) w_i(t_m)$$

$$p'_{wf\,kj}(t) = \sum_{m=1}^{n} \left(e^{\left(\frac{t_m - t}{\tau_{kj}}\right)} - e^{\left(\frac{t_{m-1} - t}{\tau_{kj}}\right)} \right) p_{wf\,k}(t_m)$$

Liang et al. (2007) and Liang (2010) proposed the CM coupled with a fractional flow model as a method to optimize the produced oil volume by adjusting the water injection rates in mature waterfloods. The objective function can minimize the total production costs or maximize the cumulative oil production. The authors used one time constant ($\tau_j = c_t V_{pj}/J_j$) for each producer, and call it the CMP model. They tested the optimization problem for various oil prices, which led to different scenarios of favorable injection profiles. In this study, they showed that the CM is capable of predicting the dynamic behavior for injection and production wells. The fractional flow model underperforms when early time data are used. Furthermore, employing a single τ in the model cannot account well for the remnant primary production.

Later, Sayarpour (2008) introduced analytical solutions with superposition in time to Yousef's (2006) CMIP and Liang et al.'s (2007) CMP. Moreover, the author presented the CM with a single time constant which assumes a reservoir consists of a virtual injector (aggregated injection rates per step) and a virtual producer (aggregated production rates per step). The BHP variation of individual wells is neglected in the CMT (tank representation of the entire field). The techniques were applied in history-matching and reservoir uncertainty evaluation of water-CO_2 floods. In this work, the CM is coupled with a fractional flow model to calculate oil rate and optimize oil production by reallocating the field injection rates. The CMT does not account for the BHP variations of individual wells. Using the fractional flow model to calculate oil rate is limited to mature waterflooding cases. In all 3 approaches, Sayarpour (2008) uses the same time constant to consider the primary production and the time lag between an injector-producer pair, which might not represent the physics of the primary production.

In the CMT, the sum of λs is assumed to be unity. In real reservoirs, some of the injected fluid may not reach the producer due to fluid escape to an aquifer or thief zone. To account for this, Chen and coworkers (2010) modified the CM by relaxing the assumption of unity λ_{ij} in the case of a lumped reservoir model (tank model) in which a single injector and a single producer exist. They also modified the CM to enhance the accuracy of matching and predicting oil production. Gentil's (2005) fractional-flow model is used in the modification of the CM where the squared errors between measured and predicted oil production rates are minimized by optimization. The application of the modified CMT for oil rate prediction in compartmentalized reservoirs may fail since the input signals can be different than the output signals.

For the first time, Izgec and Kabir (2009) employed the CM to evaluate injector-producer connectivity before breakthrough of injected fluid. They showed that the CM is practical in transient-flow periods before fluid breakthrough. The model is tested with the synthetic inverted 5-spot and the channelized system. The connectivity values were compared with the Streamline Simulator (SS) allocation factors and found almost equal. In the study, the governing equations of both the pressure-transient testing and the CM are formulated utilizing the continuity equation to show both approaches are equivalent. The authors indicated the importance of the injection rate perturbation to propagate signals effectively over targeted distances in the system.

Nguyen (2012) validated the CM parameters using Darcy's law (for λ, weight) and step test (for τ, time constant) to express them in terms of physical properties. The author showed that the connectivity can be used to calculate the transmissibility, where Gentil's (2005) definition of λ is used:

$$\lambda_{ij} = \frac{T_{ij}}{\sum_{j}^{K} T_{ij}}$$

and recommended converting λ to transmissibility, which allows comparison of the producer connectivities with different injectors. Nguyen (2012) has confirmed that, for the conditions assumed, the CM results agree with the SS results. Before the field application, calculating the coefficient of variation (C_v) of the rates and eliminating the ones with small variance rate can assist the model to avoid unreliable connectivity information. Furthermore, the CM was employed to evaluate IWC and forecast production rate for a water-CO_2 flood. The author identified the weaknesses of the model application to water-CO_2 and the further needs, such as rock and fluid data, to improve the performance of the model.

In real field examples, it is likely that there will be violations of the core assumptions of the CM during certain events, such as producer shut-ins and adding new producer. If producer BHP's are fluctuating, the CM needs them as input data to provide better IWC estimates. Failing to provide the BHP data may result in unstable estimates, which do not describe well the physics of the problem. Therefore, modified versions of the CM have been proposed to estimate more stable and physical parameters. Kaviani et al. (2012) made the CM more robust to field conditions where changing producer pressures (BHPs) are unavailable and the number of producers is not

constant during the window time. They proposed the segmented CM for the absence of BHPs and the compensated CM for cases with producer shut-in periods. The segmented CM finds the limited number of segmentation times and adjusts the BHP term in the model during each segmentation time. The compensated CM divides the window time into intervals where the number of producers stays constant during each interval. The connectivites of each interval are updated using the shut-in producer connectivities and the IWC coefficients between the virtual injector at the location of the shut-in well and other producers. The authors tested the combination of compensated and segmented CMs with both synthetic and field data and found that the enhanced model performs better than the "simple" CM. In a field application, the segmented/compensated CM results agreed with the findings from an independent geological study.

Compared to Stewart et al. (1984)'s estimation of fault conductivity (mD/ft), Bansal and Sayarpour (2012) estimated fault-block transmissibility in terms of net flux (bbl/day/psi) using injection, production and pressure data as inputs in their semi-analytical CM. In a compartment, the amount of fluid flowing out/in is calculated using the connectivities estimated from the Eq.(2-7.7):

$$\sum_j \sum_i \lambda_{ij} i_i(t) - \sum_j q_j(t)$$

where λ_{ij} is the connectivity between injector i and producer j, and i_i and q_j are the injection and production rates, respectively. They used simultaneous pressure and rate history together to check fault status (sealing or leaking), calculate the average reservoir pressure in enclosed parts of a reservoir, and estimate effective flux rate through a leaking fault. They validated the analytical formulation embedded in model with synthetic and real field data. These authors concluded that utilizing pressure data along with the production data is crucial to establish fault-block transmissibility in compartmentalized reservoirs.

Though the CM is mainly used to capture the effects of interwell heterogeneity, it was not known whether the heterogeneity was due to the near- wellbore region or a similar heterogeneity far from the wellbore. Soroush (2014) investigated the CM employing vertical wells to study near wellbore heterogeneities. This author found that the heterogeneities around the wellbore have more impact on IWC than the ones between the wells. The CM was modified to apply in real field cases

in which producer shut-ins, mini shut-ins or skin changes exist. The application of the model in conventional and heavy oil reservoirs was presented.

Cao and Lake (2014) recently proposed a version of the CM which includes an oil material balance and uses fractional flow theory. In this work, the CM minimizes the squared sum of two residuals for total rate and oil rate. Pressure and saturation values change at each time step to consider the variation of total mobility. The authors tested the coupled CM with heterogeneous synthetic field data and observed that the model results are consistent with the field geology.

Moreno and Lake (2014) discussed the problem of setting an upper limit on the uncertainty of IWCs obtained from the CM employment. They found that the uncertainty for the unconstrained parameter estimates can be used to fix upper limits on the fluctuations from the means of the constrained case, in which $\lambda_{ij} > 0$, all producers have the same time constant $\tau_j = \tau$ and $\sum_j \lambda_{ij} = 1$. The application of the second-order perturbation theory to this issue provides analytical bounds revealing clearly the degradation in parameter estimates when more well-to-well interactions are included. A *posteriori* approach presented by Kaviani et al. (2014) also shows that for a maximum available window time, optimizing more than a certain number of well interactions provides more variable estimates. Compared with λs, τ estimates tend to be more variable. They introduced two dimensionless numbers, the CM number, C (Eq. 2.2b), and the ratio of number of measurements to the number of model unknowns, L, for a quick evaluation of the stability of the parameter estimates, λ and τ.

$$C = 0.006328 \frac{D\Delta t}{\frac{A}{K}} \qquad \ldots (2.2b)$$

where D is the diffusivity constant, Δt is a sampling time, A is an area, and K is the number of producers. They evaluated the range of the CM number and L for stable estimates:

- λ estimates are stable, when $0.3 < C$ and $L \geq 4$,
- τ estimates are stable, when $0.3 < C < 10$.

To our knowledge, none of the above CM versions has been used to evaluate tight reservoir IWC. Indeed, Kaviani et al. (2014) indicate that the conventional CM may perform poorly in tight reservoirs for IWC evaluation. For example, for cases with permeability less than 1 md, the

prediction error of the estimated rates and variabilities (as measured by the coefficient of variation, C_v) of the connectivity estimates increases up to 1% and ~0.5, respectively, assuming that a sufficient number of data is provided.

2.3 Common Challenges in Tight Reservoirs during Model Application

Fracture stimulating horizontal wells in low permeability formations, such as tight oil reservoirs, is a common practice. Estimating the connectivity between these wells is useful for the design and management of a field, especially when waterflood recovery is applied. We know that a fluid inside very low permeability rocks will not flow at an economic rate without fracture stimulation. Since fracturing enhances the near wellbore region permeability, this makes the CM useful for connectivity evaluation in low permeability reservoirs.

Fractures make IWC analysis complicated, as the complexity of fracture geometry introduces additional heterogeneities in the interwell region. It is challenging to distinguish between these fracture related heterogeneities and local geological heterogeneities. The CM results reveal the effect of these heterogeneities altogether.

Pumped proppant tonnage also may affect IWC. For instance, pumping too much proppant can create fracture hit/onlap, which might cause reduction of the interwell heterogeneity information embedded in the flow rates. Injected fluid preferentially followed the paths through these fracture hits, which leads to loss of valuable information such as the existence of fault/barrier between wells. Another challenge is a change of the fracture-to-fracture connection over time. Most of the long distance fracture-to-fracture connections may be lost as depletion continues within the fracture system (Sardinha et al., 2014).

As the reservoir is waterflooded, fracture shear failure might occur and which directly affects the connectivity of a fractured well (Palmer et al., 2007). It is not well known when exactly the fracture shear failure happens. This process may occur gradually; therefore, we might not be able to exclude this period from our analysis period. It might introduce dubious information to our analysis results, as it is hard to differentiate.

Injection induced fractures can also control the IWC. Fluid pumped to these fractures might not represent the real signal sent, which can cause misleading results interpretation. Therefore, determination of threshold injection rates to avoid fracturing a formation can alleviate such causes.

Despite all these challenges, the CM has a capability of production history matching for individual wells, a group of wells, and an entire field. The above-mentioned methods cannot identify the problems highlighted as challenges, however, the CM results are helpful to identify the challenges. In addition to that, the CM can provide us enough information to evaluate the water flooded reservoir heterogeneity. Using the CM results, we can prepare an infill drilling plan, which is out of the scope of the above discussed methods. For the model, flow rates are enough to do all of these. Integrating the CM results with other data enriches reservoir characterization. The model only requires flow rates. Furthermore, it can identify wells interacting with an aquifer. We can also determine the type of IWC employing the CM results. With the help of the CM results, we can find optimum values for hydraulic fracturing design.

CHAPTER 3: MODIFIED CAPACITANCE MODEL CM-PW

3.1 Introduction

Wells are an important source of information to better understand the reservoir characteristics. From the drilling to final production stages, engineers collect many types of data from wells that will be used for the field management. Some of these data are low cost, such as injection and production data. In conventional numerical simulators, injection and production data are needed for history matching. Once the past reservoir behavior is modeled, the ultimate target is to predict the future behavior. Yet not a single model or scenario is enough to quantify geological uncertainty in a system. Considering that increasing number of input parameters involving noise might augment the risk of making a wrong decision during heuristic processing, for the sake of simplicity, the uncertainty evaluation of a single input parameter model is to be preferred to multi-input models. Using only the injection and production data without the need of a geological model makes for a practical and attractive approach.

A practical technique has been developed to quantify interwell connectivity in a reservoir using production- and injection-rate fluctuations. Yousef et al. (2006) proposed the Capacitance Model (CM – some literature refers to the CM as the Capacitance-Resistive Model or CRM) to predict the production rate of a producer as a summation of the effects of primary production, the contributions from surrounding injection wells, and the BHP changes of the connected producers. The CM has been used to analyze flow rates for estimating IWC. Many case studies show the CM can successfully predict production and identify flow conduits and barriers in conventional reservoirs. The challenging task is to extend the CM to estimate connectivity between injectors and producers in tight reservoirs.

3.2 Model Development and Validation

As discussed in Section 2.2, t original CM was proposed by Yousef et al. (2006). The full model has three unknown parameters for each injector-producer pair: (1) λ, showing the magnitude

of the connectivity; (2) τ (time constant), reflecting the fluid storage and compressibility in the interwell region; and (3) ν, quantifying the effects of producer BHPs (Eq. 3-1).

$$\hat{q}_j(t) = \lambda_{pj} q_j(t_0) e^{-\left(\frac{t-t_0}{\tau_{pj}}\right)} + \sum_{i=1}^{i=I} \lambda_{ij} w'_{ij}(t) + \sum_{k=1}^{k=K} v_{kj} \left[p_{wf_j}(t_0) e^{-\left(\frac{t-t_0}{\tau_{pj}}\right)} - p_{wf_j}(t) + p'_{wf_{kj}}(t) \right] \quad \ldots (3\text{-}1)$$

λ can also be interpreted as an allocation factor and compared with streamline simulation results. The time constant τ is a function of active pore volume, compressibility, and productivity index and reflects the time lag of the injection signal at the producers. $\hat{q}_j(t)$ is the predicted total fluid production rate of producer j. $w_{ij}'(t)$ and $p'_{wf\,kj}(t)$ are defined as

$$w'_{ij}(t) = \sum_{m=1}^{n} \left(e^{\left(\frac{t_m - t}{\tau_{ij}}\right)} - e^{\left(\frac{t_{m-1} - t}{\tau_{ij}}\right)} \right) w_i(t_m) \quad \ldots (3\text{-}2a)$$

and

$$p'_{wf_{kj}}(t) = \sum_{m=1}^{n} \left(e^{\left(\frac{t_m - t}{\tau_{kj}}\right)} - e^{\left(\frac{t_{m-1} - t}{\tau_{kj}}\right)} \right) p_{wf_k}(t_m). \quad \ldots (3\text{-}2b)$$

A version of the CM, called the CMP, uses the producer drainage volume based CM (CMP = Capacitance Model Producer-based effective pore volume, Liang et al., 2007; Liang, 2010). For the CMP, $\tau_{ij} = \tau_j$ and $\tau_{kj} = \tau_j$. That is, there is only one time constant for each producer well, rather than a time constant for each injector-producer well pair. Therefore, Eq.s 3-2 become

$$w'_{ij}(t) = \sum_{m=1}^{n} \left(e^{\left(\frac{t_m - t}{\tau_j}\right)} - e^{\left(\frac{t_{m-1} - t}{\tau_j}\right)} \right) w_i(t_m) \quad \ldots (3\text{-}3a)$$

and

$$p'_{wf_{kj}}(t) = \sum_{m=1}^{n} \left(e^{\left(\frac{t_m - t}{\tau_j}\right)} - e^{\left(\frac{t_{m-1} - t}{\tau_j}\right)} \right) p_{wf_k}(t_m). \quad \ldots (3\text{-}3b)$$

The discretized CMP for multiple injectors is

$$\hat{q}_j(t) = \lambda_{pj} q_j(t_0) e^{-\left(\frac{t-t_0}{\tau_{pj}}\right)} + \sum_{i=1}^{i=I} \lambda_{ij} w'_{ij}(t) + \sum_{k=1}^{k=K} v_{kj} \left[p_{wf_j}(t_0) e^{-\left(\frac{t-t_0}{\tau_{pj}}\right)} - p_{wf_j}(t) + p'_{wf_{kj}}(t) \right] \quad \ldots (3\text{-}4a)$$

In the case where the producer BHPs are constant during the period, the Eq. 3-4a simplifies to:

$$\hat{q}_j(t) = \lambda_{pj} q_j(t_0) e^{-\left(\frac{t-t_0}{\tau_{pj}}\right)} + \sum_{i=1}^{i=I} \lambda_{ij} w'_{ij}(t). \quad \ldots (3\text{-}4b)$$

The CMP is a simplification of the "full" CM, sometimes called CMIP (Capacitance Model Injector-Producer-based effective pore volume), as the CMP has fewer unknowns to be estimated

than the CMIP. For a short time interval (or period) $t_0 < t < t_{max}$, we may have few flow rate data, which might not be sufficient for an optimization problem. In such cases, having fewer unknowns is preferred to preserve the ratio of the number of data to the number of unknowns and reduce computational effort. This simplification, however, is at the expense of assuming that one value of τ is sufficient to capture the time effect for all injectors contributing to the production of a particular well.

A summary of how the model works is provided in **Figure 3.1**. The model is written in the MATLAB©. We preassign initial values to start the optimization problem. Using the initial values and injection rates (w(t)), the model estimates production rates ($\hat{q}(t)$) at time t. Then, the model minimizes $\sum_{k=1}^{k=K}(q_k - \widehat{q_k})^2$ employing the fmincon function in MATLAB© for a timestep t. The fmincon determines the minimum of a constrained nonlinear multivariable function. It requires upper and lower boundaries (sqp and interior-point options)

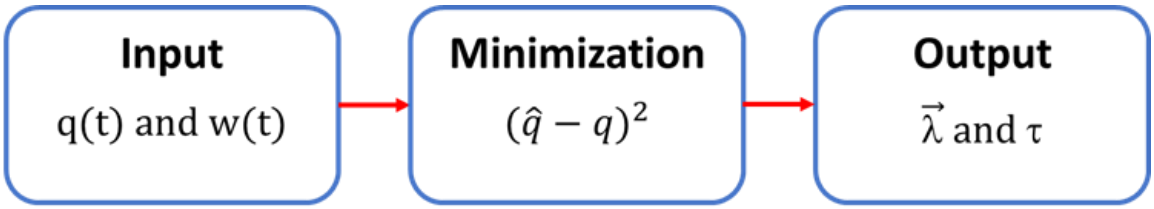

Figure 3.1 Working algorithm of the model (λ for each injector-producer pair, τ for each producer)

Having small perturbations in production profiles due to low permeability and many wells in the model reduce the possibility of the CMP obtaining physically plausible τ and λ estimates and a sufficient flow-rate quality match. For example, injectors with similar changes in rates (called "collinearity") and their highly attenuated results at the producers might lead to erroneous parameter estimates such as finding a 'connection' between an injector-producer pair which does not exist. Once these spurious connections are allowed in the problem, the CMP will have a poor match quality because the model will replace the real contribution from a connected injector to a producer with the nonexistent contribution from an unconnected injector. To address the problem, we suggest spatial windowing that reduces the possibility of identifying inappropriate connections. Using the areal windowing technique with the CMP, we can choose an injector of interest and

offset producers and perform an IWC evaluation. This way we minimize the effect of injection collinearity between nearby injectors. When we apply windowing, however, material balance is no longer preserved, which requires a further modification to avoid violating the material balance basis of the CM. Therefore, we add a pseudo well to the model, the CM-PW. The CM-PW is the CM with a pseudo well in the model, which accounts for any flow imbalance between a chosen area and outside region (**Figure 3.2**). This mechanism is introduced to ensure material balance differs from the method of Yousef et al. (2006) as that the pseudo well contribution can change with time; on the other hand, Yousef et al.'s method represents an average of the imbalance over the whole analysis period.

(A)

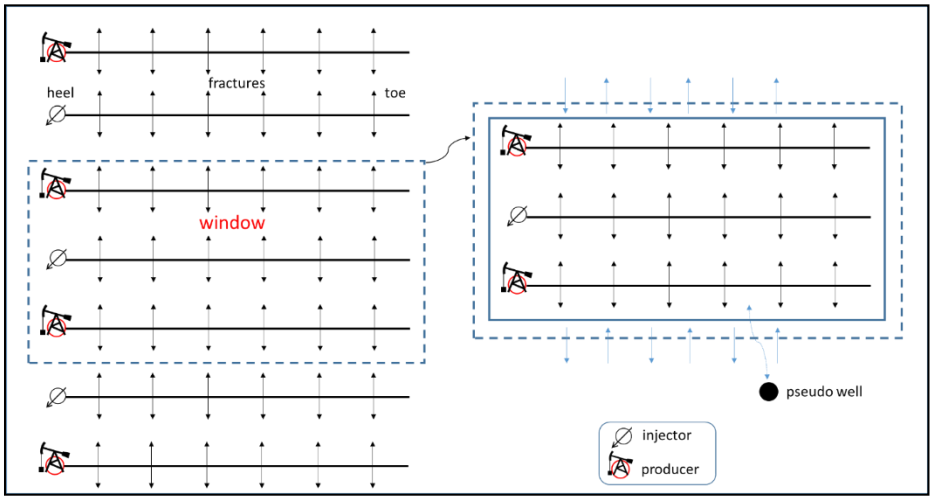

(B)

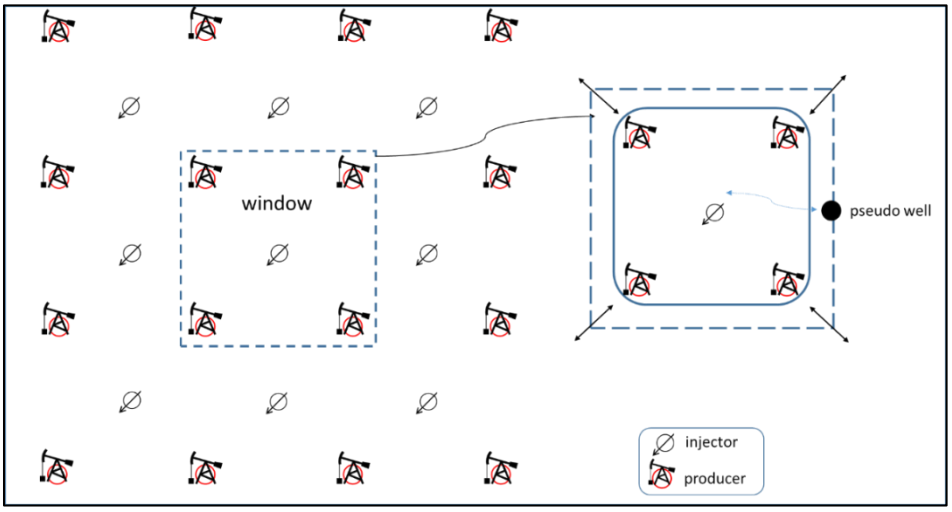

Figure 3.2 Schematic drawings showing a sample window and a pseudo well accounting for flux imbalance; (A): Horizontal wells, (B): Vertical wells. Edited from Mirzayev and Jensen (2016)

To determine the type of imbalance and treat it as a pseudo well, the following interpretation is applied. When the total injection rate of the system exceeds the total production rate, the PW is a pseudo producer (Eq. 3-5). If it does not exceed the total rate, the PW is a pseudo injector.

The production rate of the pseudo producer (q_p) is adjusted for the injection-production time delay which, in effect, means the pseudo well produces from the same locations where injectors are present; therefore, injection rates are not required to be time-shifted for q_p.

$$q_p(t) = \left|\sum_{i=1}^{i=I} w_i(t) - \sum_{i=1}^{i=I}\sum_{k=1}^{k=K} \lambda_{ik} w_i(t)\right| \quad \text{... (3-5)}$$

where $\hat{q}_p(t)$ is estimated via optimization from

$$\hat{q}_p(t) = \lambda_{pp} q_p(t_0) e^{-\left(\frac{t-t_0}{\tau_{pp}}\right)} + \sum_{i=1}^{i=I} \lambda_{ip} w'_{ip}(t) + \sum_{k=1}^{k=K} v_{kp} \left[p_{wf_p}(t_0) e^{-\left(\frac{t-t_0}{\tau_{pp}}\right)} - p_{wf_p}(t) + p'_{wf_{kp}}(t)\right]. \quad \text{... (3-6)}$$

The first term of the Eq. 3-6 is the remnant of the prior production of the pseudo well for $t < t_0$. The second and third terms represent the contribution from the injectors and the effect of possible BHP variations of producers on the pseudo well production rate at time step t, respectively.

The PW is called a pseudo injector when there is a flux into a window area (Eq. 3-7). The pseudo injection rate is time-shifted to the production wells, which means the pseudo well injection rate is already filtered.

$$w'_p(t) = \left|\sum_{k=1}^{k=K} q_k(t) - \sum_{i=1}^{i=I}\sum_{k=1}^{k=K} \lambda_{ik}\, w_{ik}'(t)\right| \quad \text{... (3-7)}$$

where the weighted w'_p adds to $\hat{q}_j$, where

$$\hat{q}_j(t) = \lambda_{pj} q_j(t_0) e^{-\left(\frac{t-t_0}{\tau_{pj}}\right)} + \sum_{i=1}^{i=I} \lambda_{ij} w'_{ij}(t) + \lambda_{pj} w_p'(t) + \sum_{k=1}^{k=K} v_{kj} \left[p_{wf_j}(t_0) e^{-\left(\frac{t-t_0}{\tau_{pj}}\right)} - p_{wf_j}(t) + p'_{wf_{kj}}(t) \right]. \quad \text{... (3-8)}$$

3.2.1 Testing the CM-PW with Vertical wells

We test the modified model with various cases encompassing input data with intentionally excluded injector/producer wells, extended period producer shut-ins, and a heterogeneous 0.1 md model. We only ran cases with permeability values similar to the halo oil East Pembina Field, where the average k_h ranges from 0.1 md to 1.4 md (Krause et al., 1987).

Case 3-1. We test the model with the simulated production rates from a 5x4 nearly-homogeneous low permeability model with constant BHPs (**Table 3.1**, **Figure 3.3**). The simulation is run for 299 months and the data are sampled every 3 months (Error! Reference source not found.**Figure 3 .4**). Injection rates are produced using the East Pembina Field wells' hydraulic fracturing pressure as a constraint. Therefore, they should be in the range of injection rates shown in **Figure 3.4,** as we attempt to preserve formation without fracking it. When we apply the CM-PW to evaluate IWC for this case, we deliberately exclude I05, so we create an imbalance in the system before running the model.

Table 3.1 Reservoir and fluid data used for the semi-homogeneous 5x4 model

Parameter	Value		Parameter	Value
Porosity, ϕ, fraction	0.18		Fluid viscosity, μ, cp	0.5

Horizontal k_{matrix}, md	0.5		Reservoir size in x-direction, ft	2480
Vertical k_{matrix}, md	0.05		Reservoir size in y-direction, ft	2480
Producer $k_{near\ wellbore}$, md	10		Formation thickness, ft	27
Total compressibility, c_t, psi^{-1}	2×10^{-6}		Reservoir depth, ft	3000
Reservoir pressure, psi	1470		Model dimensions	93x93x1
μ_{oil}, cp	2		μ_{water}, cp	0.5

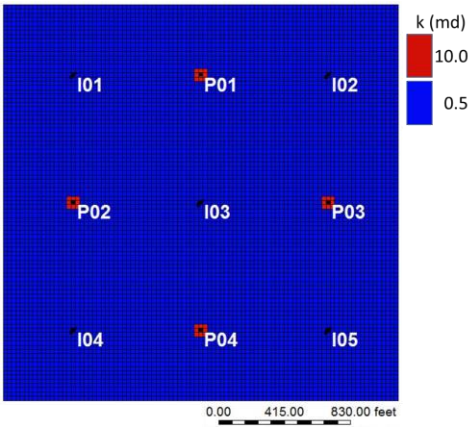

Figure 3.3 Case 1-1 5x4 semi-homogeneous model with producers stimulated (-2 skin) by an enhanced near well region (10 md); production and injection wells are denoted by P and I, respectively.

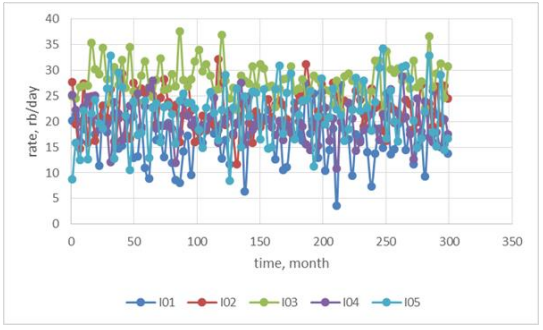

a. Injection rates

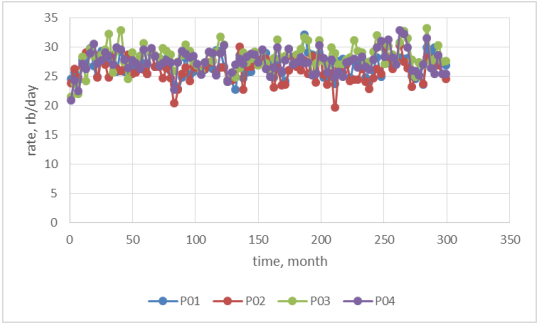

b. Production rates

Figure 3.4 Case 3-1 injection and production rates (sampled every 3 months)

The estimated connectivities of I05 in the low permeability model are similar to the corresponding connectivities from the other corner injectors (**Figure 3.5**, within 14%). The model

accuracy (ie total simulated vs total CM-predicted production rates) is very high ($R^2 \geq 0.99$, **Figure 3.6**). When compared to the conventional (40 md of Yousef et al., 2006) case results, the points lie along the 1:1 line with slightly larger variation (**Figure 3.7**). Compared to the conventional case, the support from the long-distance injectors in low permeability formations decreases by ~50%, while direct connectivities increase by ~18%. For example, the effect of a 1 bbl/day change at I01 on P03 is only 33% of the effect of the same change at I02 on P03. Because of the relatively large interwell distance and strong attenuation effect by the porous medium, the effect of the long-distance support from each injector is masked by the near-well influence, which increases the variability of the λ estimates.

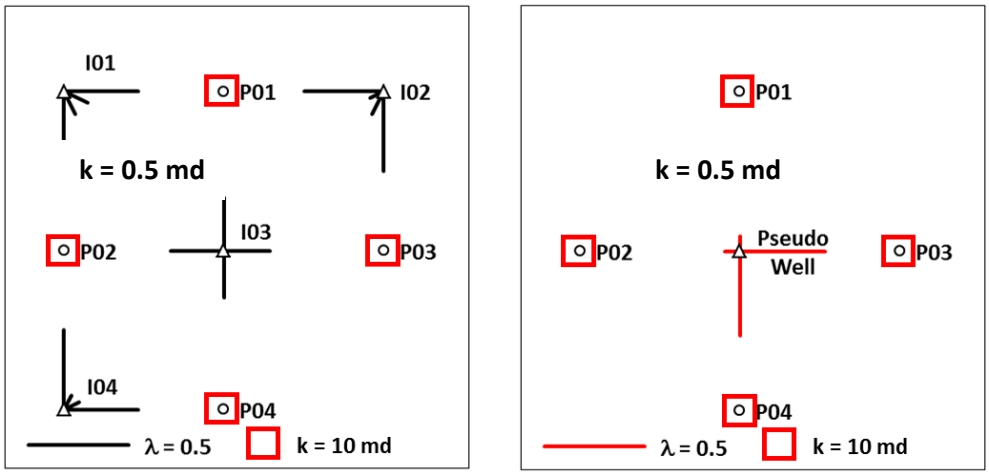

Figure 3.5 Case 3-1 Left figure: CM-PW values (λ, shown with a line indicating the direction and the magnitude of connectivity) from the model with the pseudo well (I05). Right figure: The pseudo well is placed in the center of the map where only producers are shown.

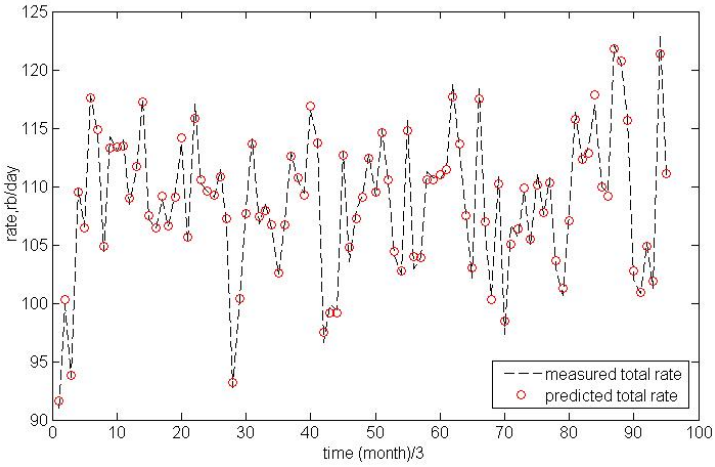

Figure 3.6 Case 3-1 CM-predicted total rate vs simulator-based total rate (R2 ≥ 0.99) – Pseudo well: I05

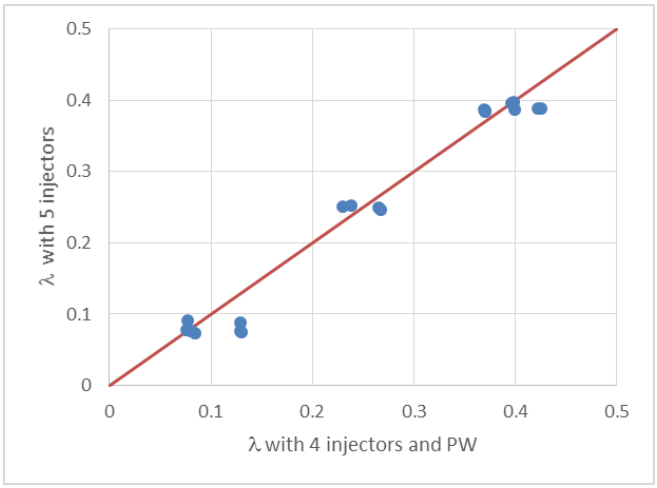

Figure 3.7 Case 3-1 connectivities from the case with I05 excluded vs. connectivities from the case I05 included

In the case when I05 is not included in the model, the history match (the simulated vs predicted production rates) using the CMP is mediocre (**Figure 3.8**-a). On the other hand, we get a good match employing the CM-PW (**Figure 3.8**-b).

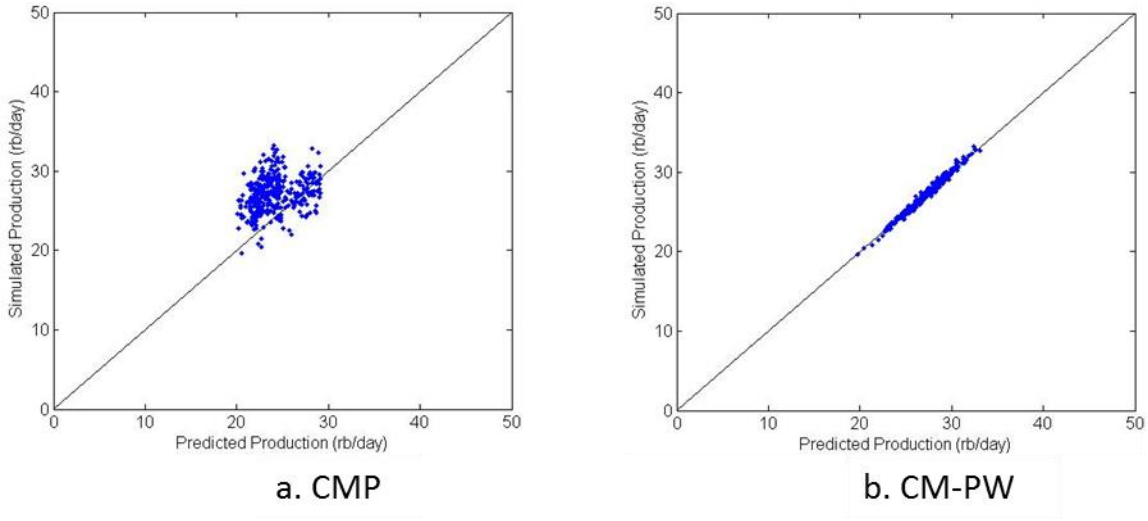

Figure 3.8 I05 not included history match plots from the CMP (left) & the CM-PW (right)

Case 3-2. Running the CM-PW when two wells are excluded from the balanced model

Here we ran the model for the more realistic case where both a producer (P04) and an injector (I05) are removed from the CM-PW model. The model estimated the connectivities with reasonable accuracy (**Figure 3.9**). The pseudo well is determined to be an injector, which strongly supports P03. This is as we would expect, because in the all-wells-included case P03 derived substantial support from the removed I05. The history match accuracy, $R^2 > 0.98$ (**Figure 3.10**). We found that the direct connectivities deviate from the all-wells-included case values with errors up to 24% (**Figure 3.11**).

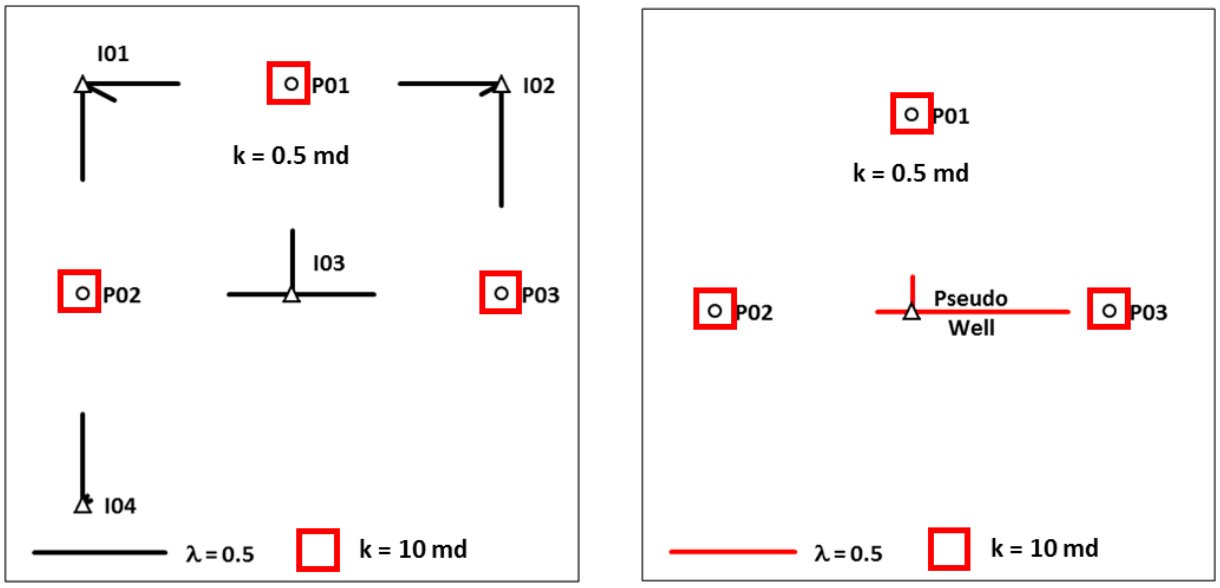

Figure 3.9 Case 3-2 λ maps of the model when P04 and I05 are removed. Additionally, the pseudo well connectivities are shown in the figure on right.

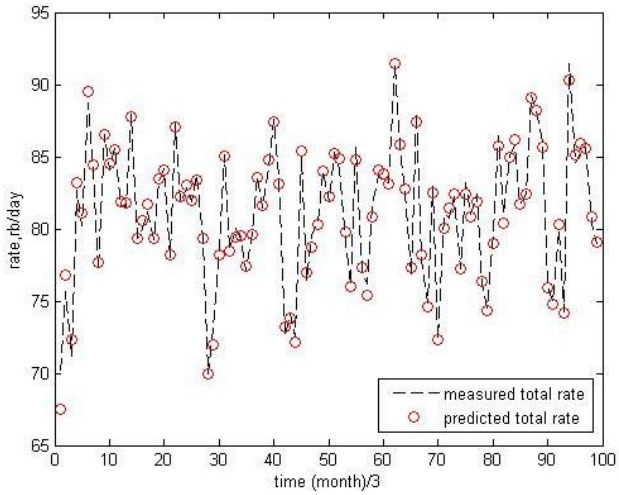

Figure 3.10 CM-predicted total rate vs measured total rate ($R^2 > 0.98$) – P04 and I05 removed from the model

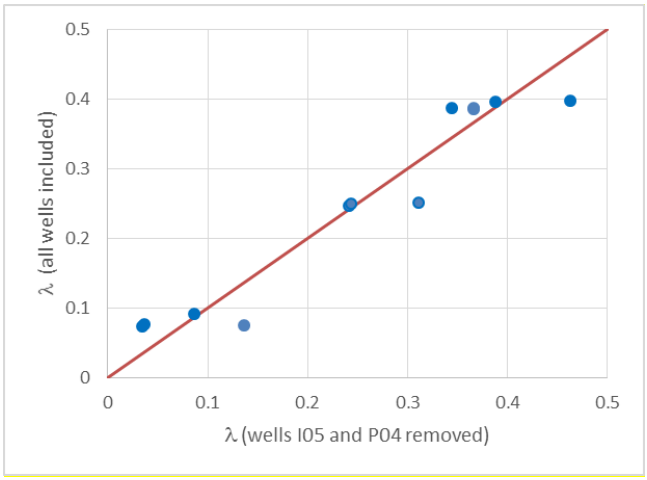

Figure 3.11 Connectivities from the Case 3-2, where P04 and I05 are removed vs. connectivities from the case where all wells are included – low permeability model.

Case 3-3. Producer Shut-in in Low Permeability Reservoirs

Shut-ins may create difficulty during the connectivity analysis done using well rates. Especially long shut-in periods are undesirable for the production rate history match. The CM is robust enough to exploit these shut-ins to evaluate producer-to-producer interactions in conventional reservoirs (compensated and segmented CM, Kaviani et al, 2012). Compared to the compensated and segmented CM (comseg-CM), the CM-PW estimates are more accurate for tight reservoirs in which a producer has a long shut-in time; $t_{shut\text{-}in}$ > 12 months. To illustrate this, we use the same 5x4 semi-homogeneous model for testing used in the Case 3-1. For this case, P01 has a shut-in time of 15 months, and the CM-PW predicted production rates had a better match with the simulated rates than the comseg-CM predicted rates (**Table 3.2 and Figure 3.12**). In particular, the comseg-CM overestimated the long-distance well pair λs (e.g., I01-P03). For the offset well pair λs, both models can estimate similar values.

Table 3.2 Case 3-3 R^2 and RMSE (root mean-squared error) of predicted rates of wells

		P01	P02	P03	P04
CM-PW	RMSE	0.002	0.003	0.005	0.002
	R^2	1.000	0.996	0.995	0.998
comseg-CM	RMSE	0.006	0.009	0.008	0.007
	R^2	0.998	0.962	0.975	0.981

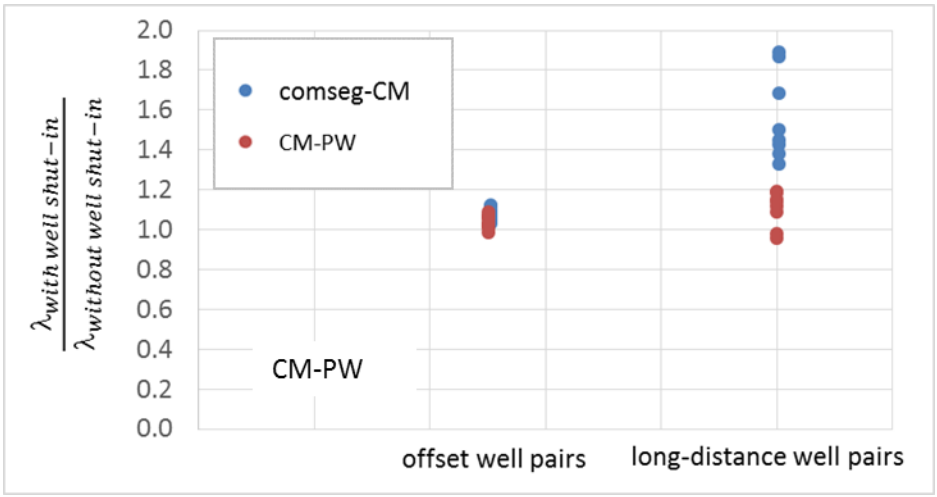

Figure 3.12 Case 3-3 CM-PW estimated λs with P01 shut-in are in good agreement with the λs obtained without the shut-in condition.

Case 3-4. Heterogeneous tight permeability reservoir

We also created a case with matrix permeability of 0.1 md (decreased from 0.5 md of the previous cases) and tested it with the CM-PW. We simulated the production rates from a 5x4 heterogeneous model (**Figure 3.15**, **Table 3.3**) and BHPs constant employing a commercial simulator. Some fractured producers were converted to injectors during field development in the East Pembina Field. We also modified the near wellbore region of injectors and producers. It allows us to inject water with higher injection rates without violating injection pressure constraint set before in the Case 3-1. The P01 hydraulic fracture crosses the barrier between P01 and I02. Hydraulic fracture properties of P01 are provided in **Table 3.4**. There is also another barrier between I04 and P02 (**Figure 3.13**).

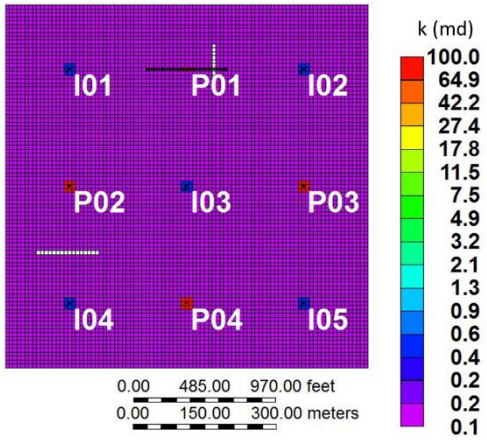

Figure 3.13 5x4 Heterogeneous model with producers stimulated (-2 skin)/fractured; production and injection wells are denoted by P and I, respectively. There are two barriers, one between P02 and I04 and the other between P01 and I02.

Table 3.3 Reservoir and fluid data used for the Case 3-4 homogeneous 5x4 model

Parameter	Value
Porosity, ϕ, fraction	0.18
Horizontal *k*, md	0.1
Vertical *k*, md	0.01
Total compressibility, c_t, psi^{-1}	2×10^{-6}
μ_{oil}, cp	2
μ_{water}, cp	0.5
Reservoir size in x-direction, ft	2480
Reservoir size in y-direction, ft	2480
Formation thickness, ft	27
Reservoir depth, ft	3000
Reservoir pressure, psi	1470
Model dimensions (x-y-z)	93-93-1

Table 3.4 P01 Hydraulic fracture properties

Parameter	Value
Primary fracture width	0.1 ft

Primary fracture permeability	1000 md
Half-length	275 ft

The simulation is run for 51 months and the data are sampled quarterly (**Figure 3.14**). The injection rates are created using the East Pembina Field injection wells' mean and standard deviation (**Figure 3.14**-a). When we apply the CM-PW to evaluate IWC for the main case, we observed that due to the very low permeability, the model does not detect the heterogeneities very well. For instance, I04 contributes only 1% more of its injection rate to P04 than P02 (**Figure 3.15**), even though there is a barrier between P02 and I04 while there is no barrier between P04 and I04. The model, however, successfully predicted the simulated production rates with the lowest $R^2 = 0.9997$ among all producers (**Figure 3.16**). The model was not able to differentiate heterogeneity (barriers) with I02 and I04 λs. From Chapter 4, we know a low injection rate signal frequency yields a high well emittance rate. We decided to retest another case (updated) with new sets of injection rates with a greater low-frequency component for I02 and I04 (**Figure 3.17**). Injection rates are phase shifted to prevent collinearity. **Figure 3.18** shows that with the updated case, the model better identifies the heterogeneity. The contribution difference of I04 in the main case was about 1%, which has increased up to 10% in the updated case. This reveals that the model is able to evaluate heterogeneities in cases with the lowest reported matrix permeability in the East Pembina Field for cases with sufficiently strong and low frequencies in the injection rate spectrum.

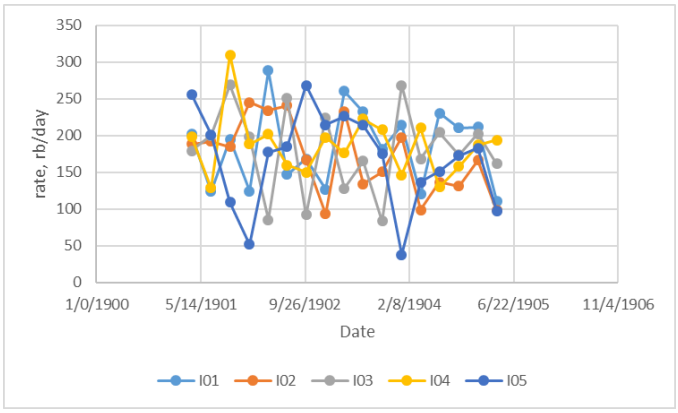

(a) injection rates

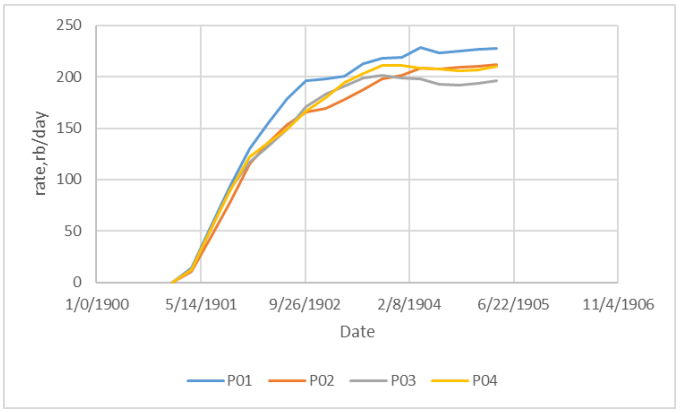

(b) production rates

Figure 3.14 (a) injection rates (sampled quarterly), (b) production rates (sampled quarterly)

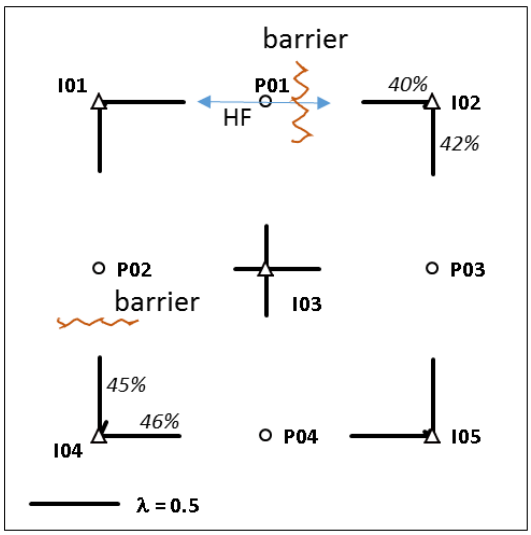

Figure 3.15 Connectivity map of the heterogeneous case with matrix permeability of 0.1md (*HF: hydraulic fractures)

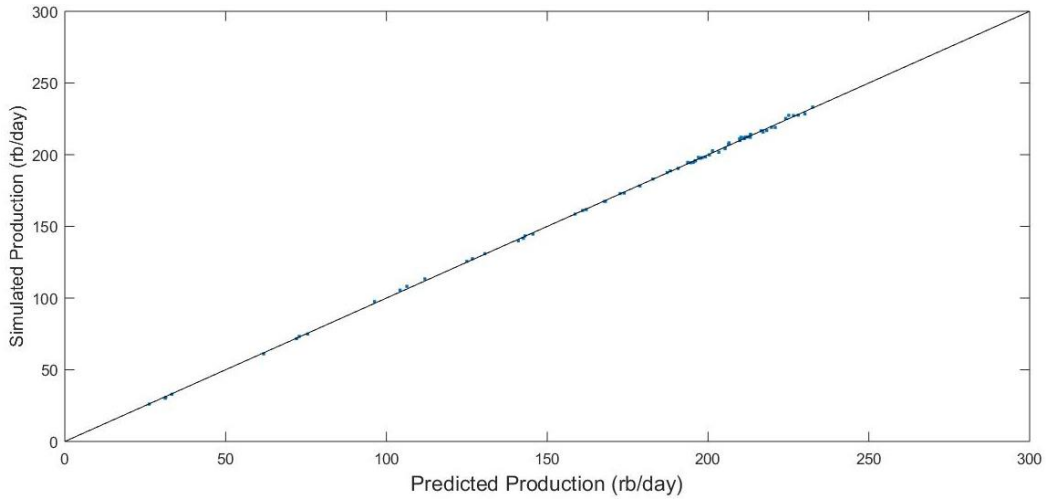

Figure 3.16 Model prediction plot.

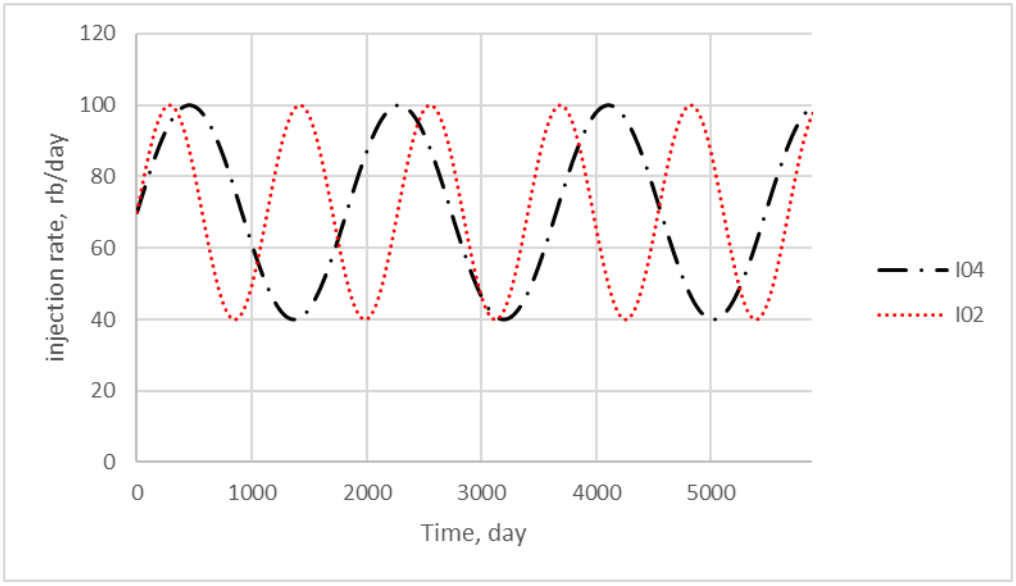

Figure 3.17 Sinusoidal injection rates of I02 and I04. Rates have amplitude of 30 and f = 0.317 cycle/years. They are also phase shifted to prevent collinearity.

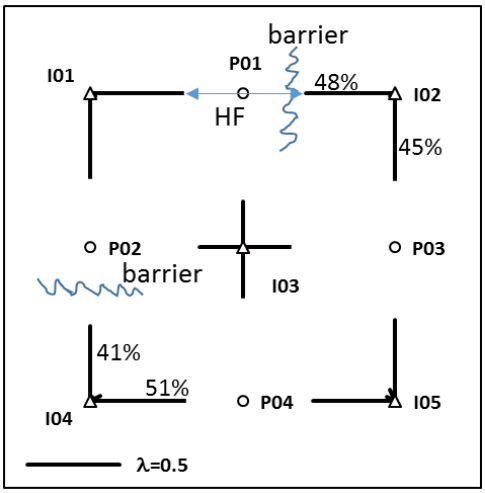

Figure 3.18 Connectivity map of the heterogeneous case with matrix permeability of 0.1md and I02 and I04 with greater low-frequency (*HF: hydraulic fractures)

In conclusion, above case results showed that the CM-PW can estimate connectivity of removed wells with slightly large variation depending on direct/indirect connectivity. In case of well shut-in, the model can also estimate similar λs as in case of well shut-in absent. We found that with a heterogeneous model with 0.1 md, the model performs well in the case of the injection signal having greater low-frequency spectrum.

3.2.2 Testing with Horizontal Wells

We test the CM-PW with a homogeneous model (**Table 3.5**), simulated with CMG IMEX© software (the method we follow to determine the final version of a simulation model is presented in **Appendix 1**). The model has 7 horizontal wells with hydraulic fractures, 3 injectors and 4 producers (**Figure 3.19**). Each well has 11 hydraulic fractures (**Table 3.6**) and the fractures penetrate both upper and lower layers. Two cases were created by excluding either an injector (Case 3-5) or a producer (Case 3-6) after running the simulation, which means the CM-PW receives rate data for 6 wells although there are 7 in the simulation model. The model is simulated for a water flooding period of 195 months (**Figure 3.20**).

Table 3.5 Reservoir and fluid data used for the homogeneous 3x4 model.

Parameter	Value
Porosity, ϕ, fraction	0.12
Horizontal k, md	0.25
Vertical k, md	0.5
Total compressibility, c_t, psi^{-1}	7×10^{-6}
μ_{oil}, cp	0.97
μ_{water}, cp	0.96
Reservoir size in x-direction, ft	4500
Reservoir size in y-direction, ft	9540
Formation thickness, ft	21
Reservoir depth, ft	3600
Reservoir pressure, psi	1200
Model dimensions (x-y-z)	225-477-3

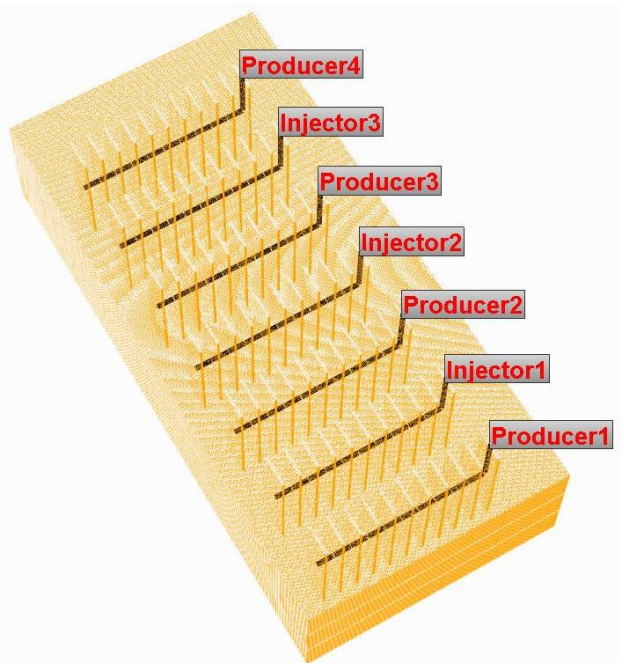

Figure 3.19 Simulation model with 7 horizontal wells; 3 injectors and 4 producers

Table 3.6 Hydraulic fracture parameters

Parameter	Value
Primary fracture width	0.1 ft
Primary fracture permeability	300 md
Half-length	275 ft

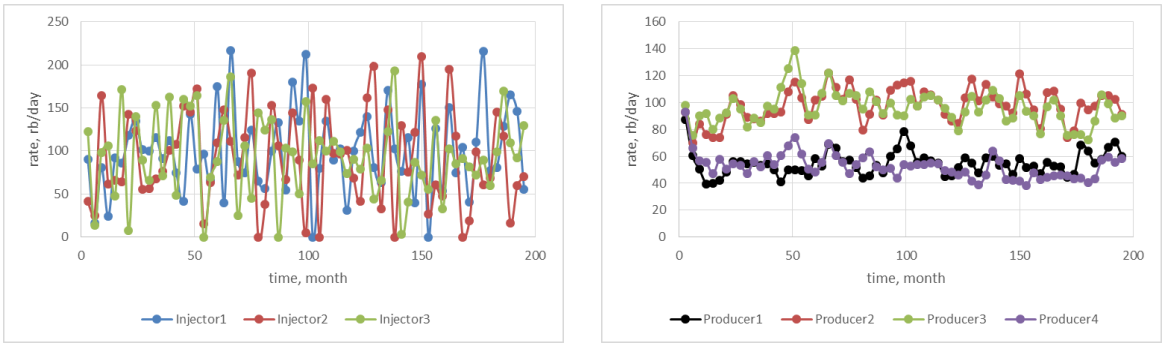

Figure 3.20 Injection (left) and production (right) rates of the 3x4 model (rates sampled every 3 months)

The CM-PW estimated the connectivities of two cases, Case 3-5, which has Injector3 missing, and Case 3-6 where Producer3 is not in the CM-PW, with good agreement compared with the full (7-well) case estimates (**Figure 3.21**). We have observed that the CM-PW predicts the estimates more accurately by 7% error when there is a flux out (**Figure 3.21**– right).

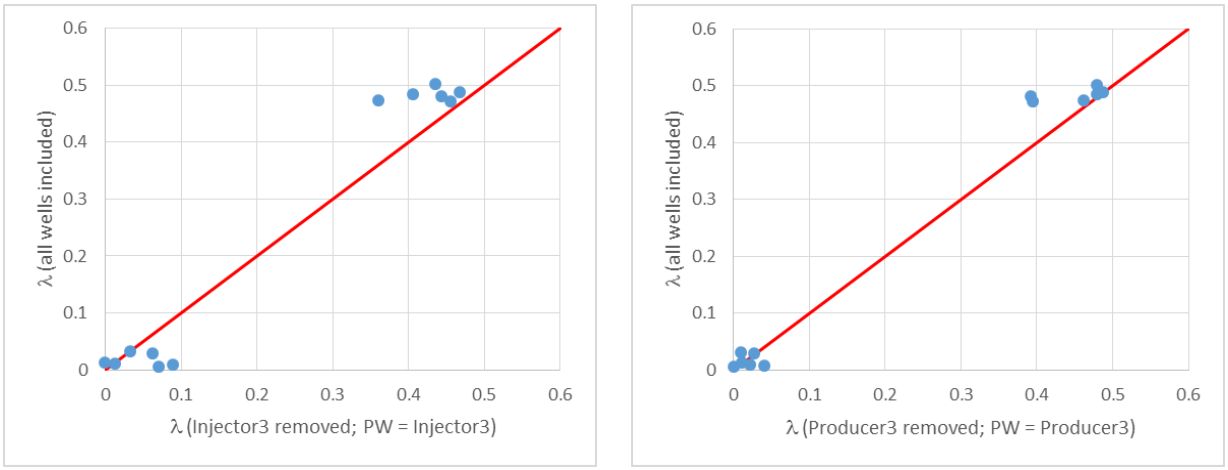

Figure 3.21 Injector3 – not in the CM-PW model (Case 3-5 – left) and Producer3 – not in the model (Case 3-6 – right)

A further test case where both a producer (Producer4) and an injector (Injector1) are removed from the CM-PW model was run (**Figure 3.22**). The flux type gets more complicated in this case, Case 3-7. The estimates for long distance connections, where the IWC values are small, are inferior to the ones in the previous two cases. We tested the model with the low permeability range of 0.1 – 1 md and injectors having a BHP constraint; the total rate match quality (measured with R^2) is not quite as good as the cases when the horizontal permeability is 5 md (**Table 3.7**). Both injection pressure constraints and low permeability lead to highly attenuated production rate profiles, which makes it difficult for the model to better predict the simulated rates.

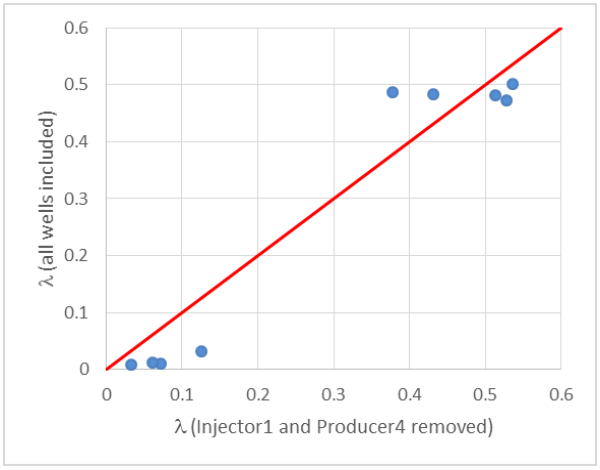

Figure 3.22 Case 3-7 connectivities from the case Injector1 and Producer4 – not in the model vs. connectivities of all wells included case

Table 3.7 Coefficients of determination, R^2, of Cases 3-5, 6, and 7, measuring agreement of simulated vs. CM-PW predicted production

Cases	R^2
all wells in the model (permeability range of 0.1 – 1 md)	≥ 0.87
either an injector or a producer not in the model (Cases 3-5 and 3-6)	≥ 0.85
two wells – an injector and a producer – not in the model (Case 3-7)	≥ 0.83
all wells in the model (k = 5 md)	≥ 0.97

Testing the model with horizontal well cases, we demonstrated that the CM-PW could estimate HW IWC in case of either an injector or a producer absent in the model. When we look at R^2 of the simulated vs. CM-PW predicted production, the model performs poorly in the case of two wells removed from the model (**Table 3.7**).

In the preceding models, we have assumed all fractures contribute equally to flow from the wellbores. For the case of fractures not contributing equally, we expect that the producer with the higher fracture conductivity will have the stronger connection with an offset injector. This issue will not be further analyzed here.

3.2.2.1 CM-PW Performance during Early Flow Period

In tight formations, the transient flow period is long enough to violate the pseudo steady state flow regime assumption of the CM. Because of low permeability, a long production decline profile is present. There should be an appreciable time before the breakthrough of the injected fluid and injection signal to be felt continually at the producer. Initial flows are more a function of the surrounding fluid and rock compressibility than injection energy. The time constant (τ) used in the shifting injection rate is longer than the delay in conventional reservoirs. Thus, the attenuated injection signals reach the producers while primary depletion effects are still significant, which makes analysis highly complicated. When the objective function of the CM is optimized for cases with highly attenuated injection signals, the chances of getting stuck in potential local minima increases.

On the other hand, in conventional reservoirs, the transient flow period tends to be only a short part of the production history. To evaluate the effect of the transient period on the CM-PW connectivity evaluations, we simulated a reservoir case having 1 md matrix permeability with two

horizontal producers, Producer1 and Producer2, a horizontal injector, and a well-length barrier between Producer1 and the injector (**Figure 3.23**). We evaluated the CM-PW performance as the period changed. To evaluate IWC during early production times, we run the CM-PW from the shortest time span, $t_{max} = t_0 + 8$ months, to up to $t_{max} = t_0 + 96$ months (**Figure 3.24**). For the first 8, 10 and 12 months, the model does not correctly evaluate the λs and τs. The cause for this failure is due to the insufficient number of flow measurements. Kaviani et al. (2014, op.cit) discuss this issue and introduce the term L, the ratio of the number of flow-rate data to the number of model parameters, and observe that at L = 2.5, the τ values are highly variable for permeability values ranging from 0.1 md to 100 md. For the 12 month period in this case, L = 2.4 which explains the inconsistency in parameter estimates. In addition, given that there exists only a decline profile during the first 15 months of production, the λs increase with increasing period size. Once the decline period switches to the predominantly steady state period in which short-time transient effects still occur, the estimates stabilize with small variations caused by repetitive minor transient periods.

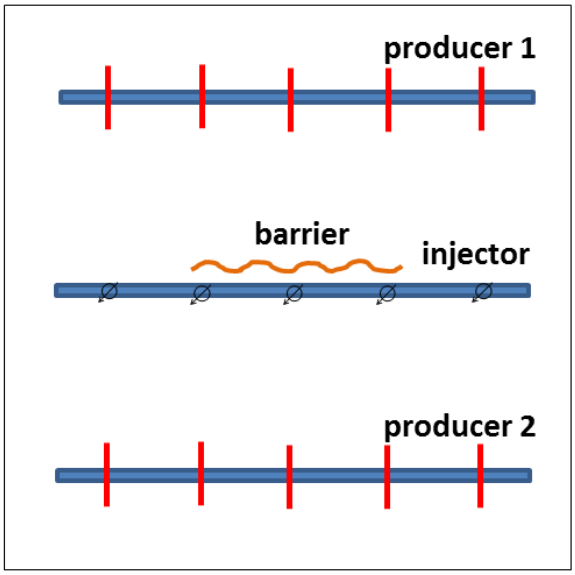

Figure 3.23 Schematic view of the heterogeneous model having 2 horizontal producers and an injector

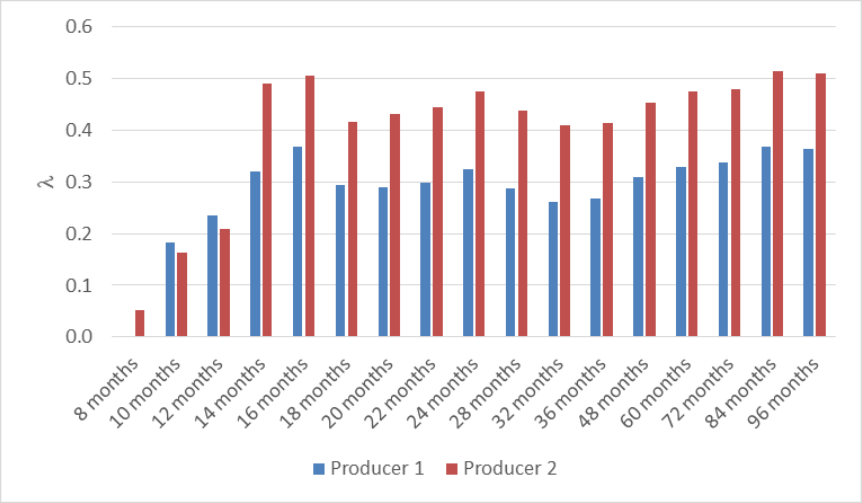

Figure 3.24 λs from the first 8 months to 96 months intervals

After 12 months, the τs reflect the heterogeneity in the system with fluctuating proportions. The period of fluctuating estimates is also observed in τ-ratio (= τ_1 / τ_2) plot (**Figure 3.25**). We can determine that even if a decline profile is included in the analysis, a single flow-rate change right after the decline period in a production profile caused by an injection perturbation is enough to detect the interwell heterogeneity.

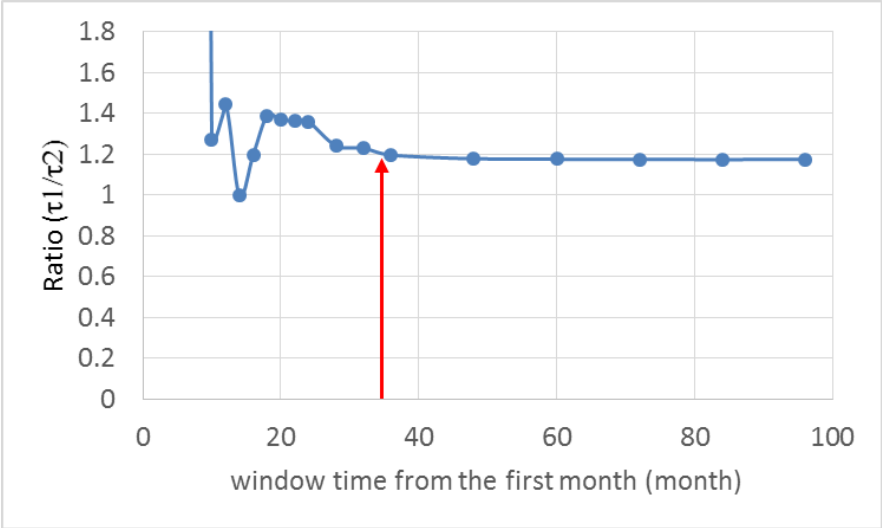

Figure 3.25 τ-ratio from 8 months to 96 months intervals

To test the effect of injection signal and area on the early period τs and λs, we ran two more cases: one with a different injection rate profile (**Figure 3.26**) and one with the system area doubled but with the well spacing is kept constant (**Figures 3.27 and 3.28**). In the case with the injection signal having an average rate of 200 rb/day, the λ values stabilize after 14 months (**Figure 3.27Error! Reference source not found.**-left). The λ values stabilize after 36 months in the area d oubled case (**Figure 3.27-** right). The τ ratios plot with the different injection signal reveals that the model was only able to detect heterogeneity once (**Figure 3.28-**left; red circle). Thus, using λs for heterogeneity evaluation during the early flow period can give reliable indications of connectivity. Nevertheless, these results show that a period possessing a decline profile must be longer than the decline period. This suggests a rule-of-thumb level for the minimum period duration. After the decline period, L > 4 should be met to have stable estimates, which is similar to Kaviani et al.'s (2014) findings.

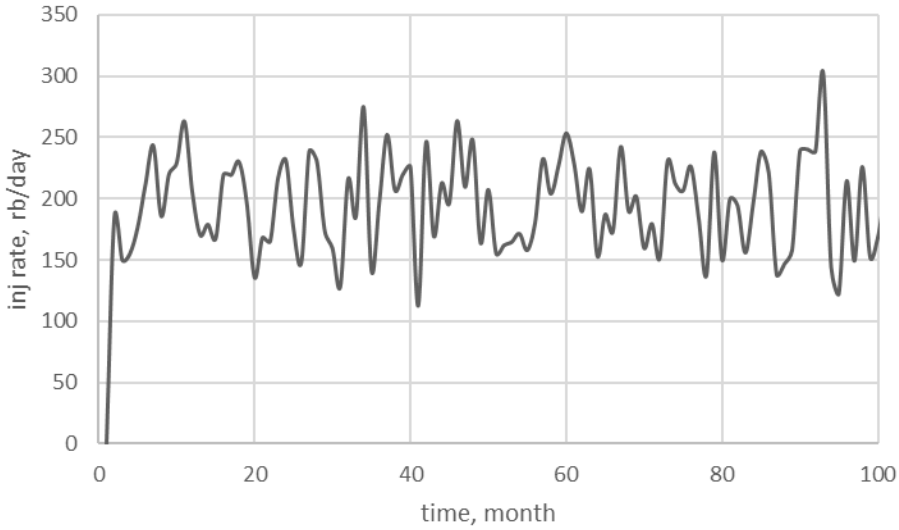

Figure 3.26 Injection rate of the injector with revised injection rates, which are similar values to the Bakken Field example described later.

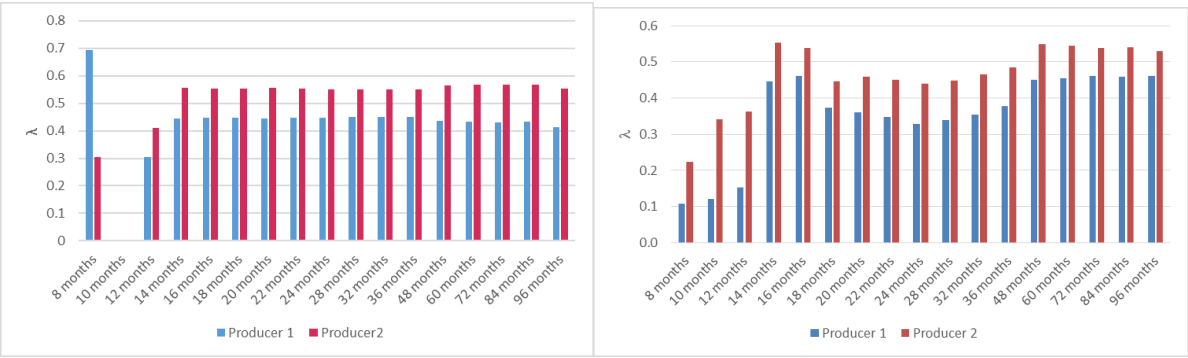

Figure 3.27 λs from two cases; different injection rate (left) and area doubled (right)

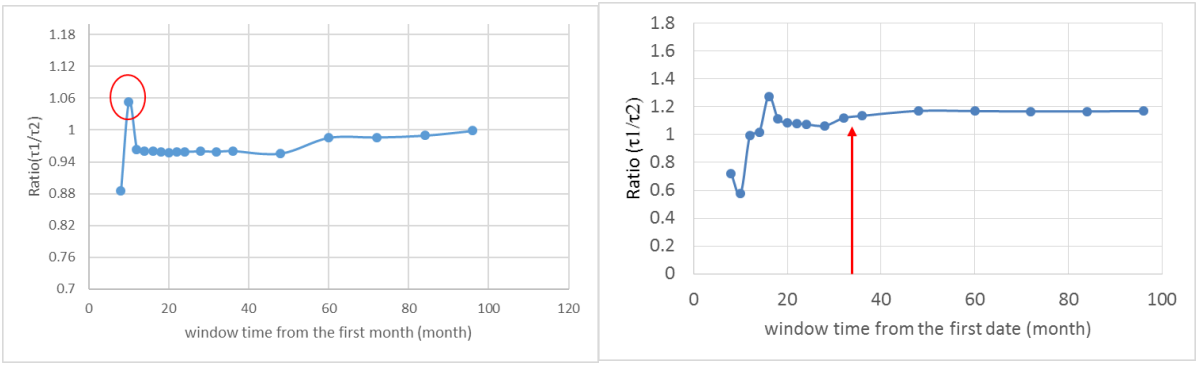

Figure 3.28 τ-ratios from two cases; different injection rate (left) and area doubled (right)

3.3 Conclusions

Case studies showed the CM-PW could estimate connectivity of wells with commingled source outside spatial window of interest. Compared to high permeability case, the long-distance connectivities in low permeability formations decreases by ~50%, while connectivity with offset wells increases by ~18%. In the tight permeability model, the model performs well to detect heterogeneity in case where the injector has a greater low frequency component. The CM-PW evaluates the heterogeneity between horizontal wells during the early flow period if the ratio of the number of sampled data to a number of unknowns (L) is greater than 2.5 and few injection-caused perturbations exist in production profiles.

CHAPTER 4: DETERMINING WINDOW SIZE FOR THE CM-PW

4.1 Introduction

Estimating a large number of unknowns using optimization with the CM application to tight oil reservoirs is challenging. Kaviani et al. (2014) report that when the number of samples per model parameter increases, estimate (λ and τ) accuracy increases as well for CM analyses in conventional reservoirs. Hence, to achieve a good estimation accuracy with a limited number of measurements, we apply spatial windowing for the model application.

Connectivity analysis for an areal window reduces the number of unknowns to be estimated in the optimization problem. We want the window to be large enough to capture the important injector-producer interactions, but small enough to remove weakly connected wells from the computation. Determining the appropriate size of the window in a given reservoir is, however, not clear. For any pilot study, we usually choose a sample area of interest based on geological, geographical, or logistical considerations. Therefore, developing an estimate of the window size is a useful tool to help implement CM analysis efficiently. To do that, we use the analogy between heat flow and fluid flow. Specifically, we used Carslaw and Jaeger's (1959) heat conduction equations for the periodic line and point sources in a homogeneous mode. For the porous medium case, we assume injection and production wells can represent the source and sink, respectively. We can mimic similar physical conditions through the corresponding equations. Both the vertical and horizontal well cases will be considered.

4.2 Use of heat equation analogy to reservoir parameters and analysis of key parameters

Interwell region heterogeneity affects IWC but heterogeneity is not the only factor affecting IWC measurements. We intuitively can make a list of these factors: diffusivity, source spectrum (frequency), interwell distance (IWD) and data sampling time. One could argue that the source frequency spectrum is not "intuitive". For example, Kaviani et al. (2014) do not consider the effects of frequency in their results. However, their results assume larger permeability

conditions, so that frequency is not an issue. As we show below, the injection rate frequency content is an important factor in low permeability reservoirs.

To assess these factors, we examine the effects of surrounding injectors on a producer of interest (**Figure 4.1**) in terms of these parameters. Depending on source type, we have different equations.

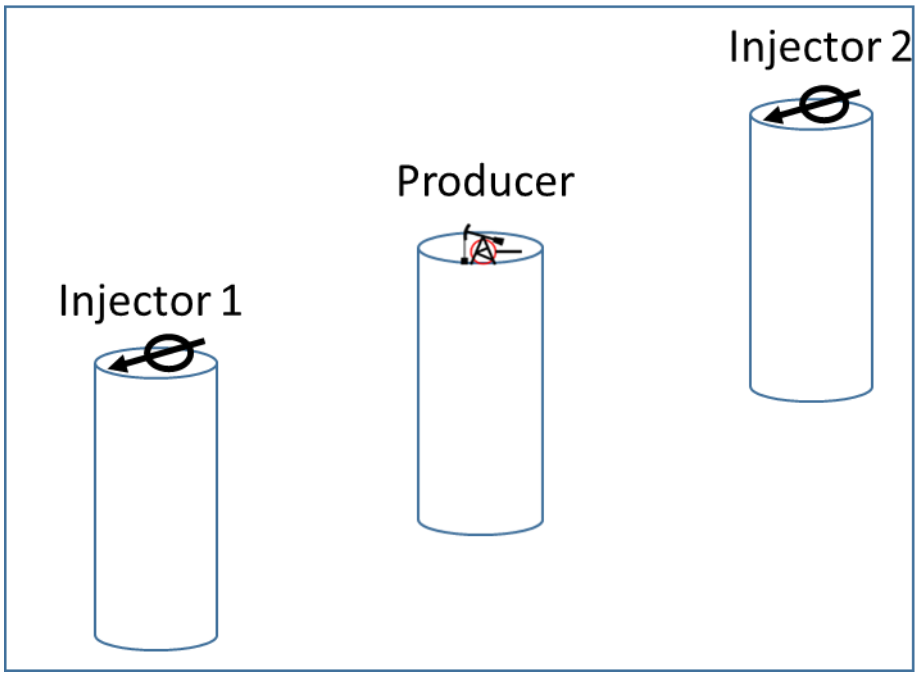

Figure 4.1 A schematic view of the 2x1 model

4.2.1 Vertical wells

Most vertical wells in a low permeability formation have a single stage hydraulic fracture. We assume vertical wells are completed for a single layer. Therefore, we treat vertical wells whether fractured or open hole as a periodic point source. Although fractured vertical wells might have an elliptical shape, we assume it to be a point source in an infinite model size. (We are aware that an elliptical shape source has a different solution than Eq. (4-1). As discussed in Durand's (1966) study involving electrical flow, problems involving circular cylinders have solutions in terms of Bessel functions; the elliptical cylinder cases will have solutions in terms of Mathieu functions. For now, we leave further investigation as a topic for future work.) We used Carslaw and Jaeger's (1959) solution for the temperature with a periodic point source (Eq. 4 – 1, similar to

well injection rate) emitting heat into an infinite homogeneous solid where heat is liberated at rate $\rho ce^{i\omega t}$ (similar to injection rate) from time $t = -\infty$ to $t = t$,

$$v' = \frac{\exp\{-\kappa r + i(\omega t - \kappa r)\}}{4\pi K^* r} \qquad \text{... (4-1)}$$

where $\kappa = \sqrt{\frac{\omega}{2K^*}}$, K^* is the heat conductivity, and ω is the angular frequency of the heat source.

Eq. (4-1) does not show the source strength, as it is not constant. If $\rho ce^{i\omega t} = a$; constant, the Eq. (4-1) would be

$$T = \frac{a * \exp\{-\kappa r + i(\omega t - \kappa r)\}}{4\pi K^* r} \qquad \text{... (4-2).}$$

T is the temperature at some location r units away from the source. We replaced the heat conductivity K^* with diffusivity **D** and presumed injection bottomhole pressure constant for a single time step representing the source strength, which should give us the injection well emittance rate ε (similar to pressure change) at a well a distance r away as a function of the diffusivity D = k/(948ϕμc) and source frequency f,

$$\varepsilon = \frac{\exp\{-\kappa r + i(\omega t - \kappa r)\}}{4\pi D r} \qquad \text{... (4-3)}$$

where $\kappa = \sqrt{\frac{\omega}{2D}}$. The well emittance rate ε is a coefficient to be multiplied with an injection bottomhole pressure for a single time step, which would give us the approximate pressure disturbance created by the injection source a distance r away. We normalize the well emittance rate with respect to an injection well of distance r = 1 ft away which has same ω as Injector 1, and call this ratio the emittance ratio R_ε,

$$R_\varepsilon = \left| \frac{\exp\{(1-r)\kappa - i(\kappa r - \kappa)\}}{r} \right| \qquad \text{... (4-4)}$$

Eq. (4-4) is the normalized version of the Emittance rate. This form of the equation helps us easily to analyze an injection well effect compared to the closest well effect on any producer of interest. We have plotted R_ε to see the effect of two parameters, frequency f (in lieu of ω) and D. We use the parameters for estimating model diffusivity listed in **Table 4.1**. For D = 210.97 md*psi/

cp, the R_ε versus distance between Injector 1 and Producer of interest has a decreasing trend as interwell distance increases, as expected (**Figure 4.2**). The plot reveals that the effect of injector 1 with f = 1 cpy (cycle per year) decreases from 1 to 0.01 within the radius of 60ft.

Table 4.1 Model parameters used for diffusivity estimation

Parameter	**Value**
Porosity, ϕ, fraction	0.1
Total compressibility, c_t, psi^{-1}	1×10^{-6}
Fluid viscosity, μ, cp	0.5

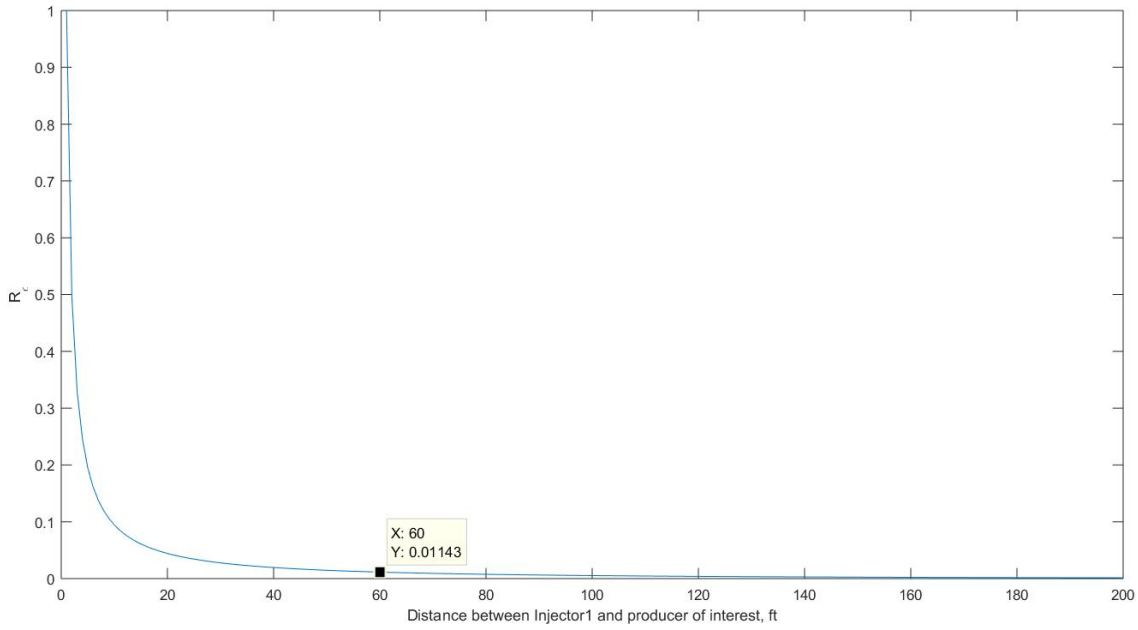

Figure 4.2 Emittance ratio R_ε versus interwell distance plot

We compared the R_ε for D = 2109.7 and 21097 md*psi/ cp. When we increase diffusivity 10 times, we observe the R_ε ratio varies from 1 to 11 as interwell distance increases from 0 to 500 ft (**Figure 4.3**). The R_ε increases with increasing diffusivity (**Figure 4.4**). We observe an opposite trend as we increase injection well frequency (**Figure 4.5**). R_ε decreases from 1 to 0.2331. This is expected, since higher frequency means the fluid compressibility better absorbs the energy and thereby makes pressure wave lose more energy. Hence, we observe a reduction in source impact on the producer of interest. R_ε decreases with increasing source frequency (**Figure 4.6**). We use R_ε ratio to observe what will be the effect of a parameter change on well emittance. Rather than

plotting a large series of curves to see the parameter change effect on well emittance, we can simply use R_ε ratio. With R_ε ratio, we can directly observe how a change in a parameter of interest affects the well emittance as interwell distance increases.

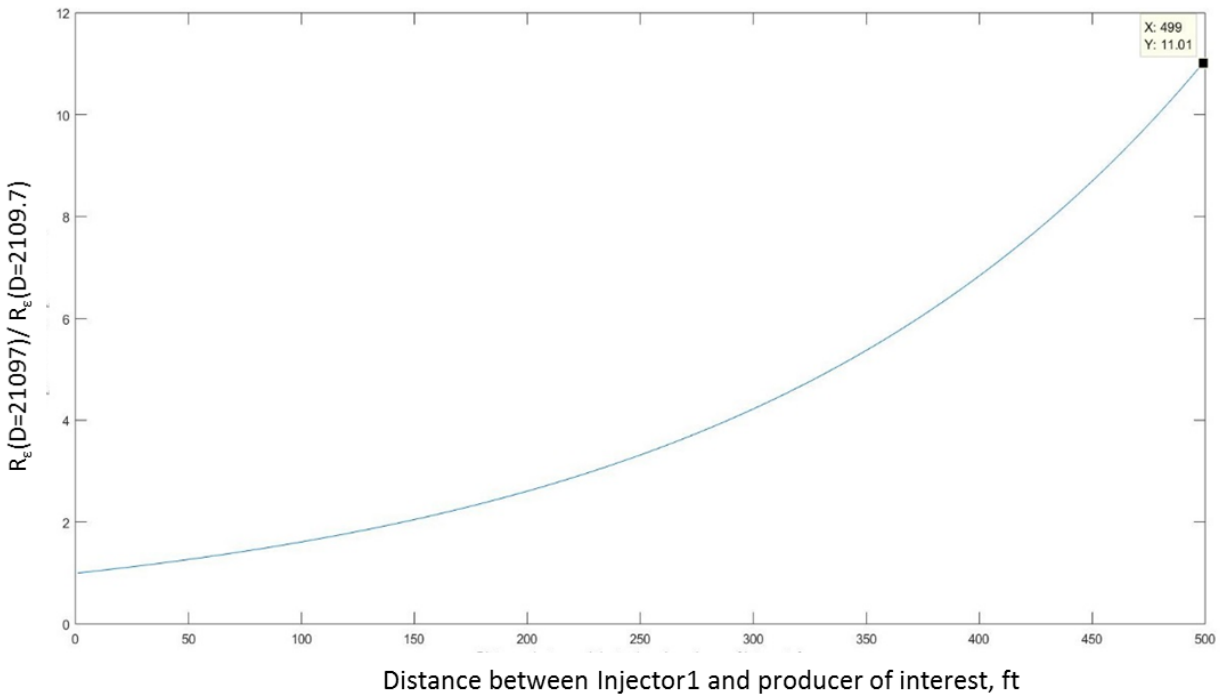

Figure 4.3 The R_ε ratio for D = of 21097 and 2109.7md*psi/ cp versus interwell distance.

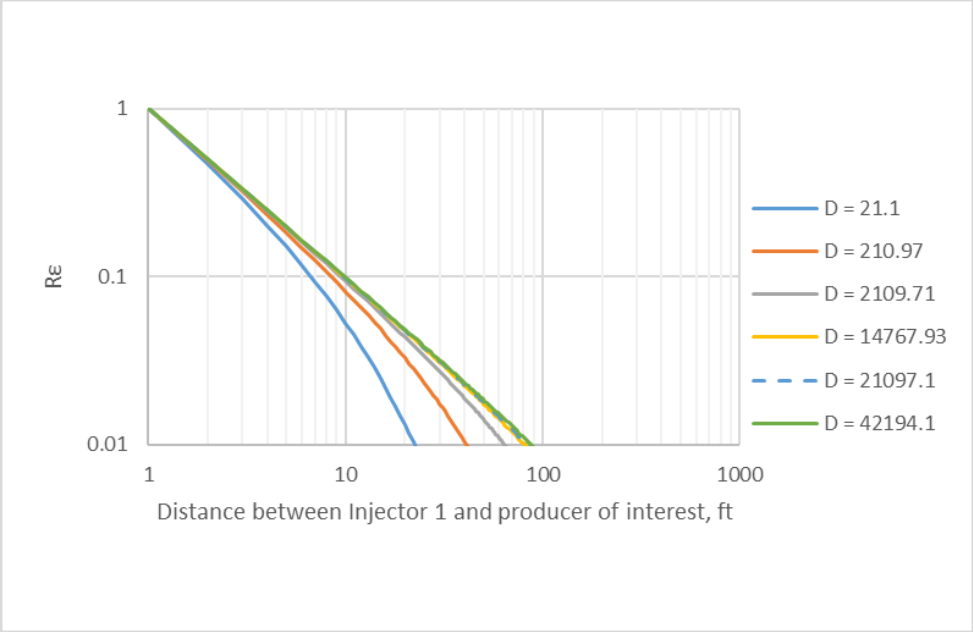

Figure 4.4 The R_ε plot for different diffusivities

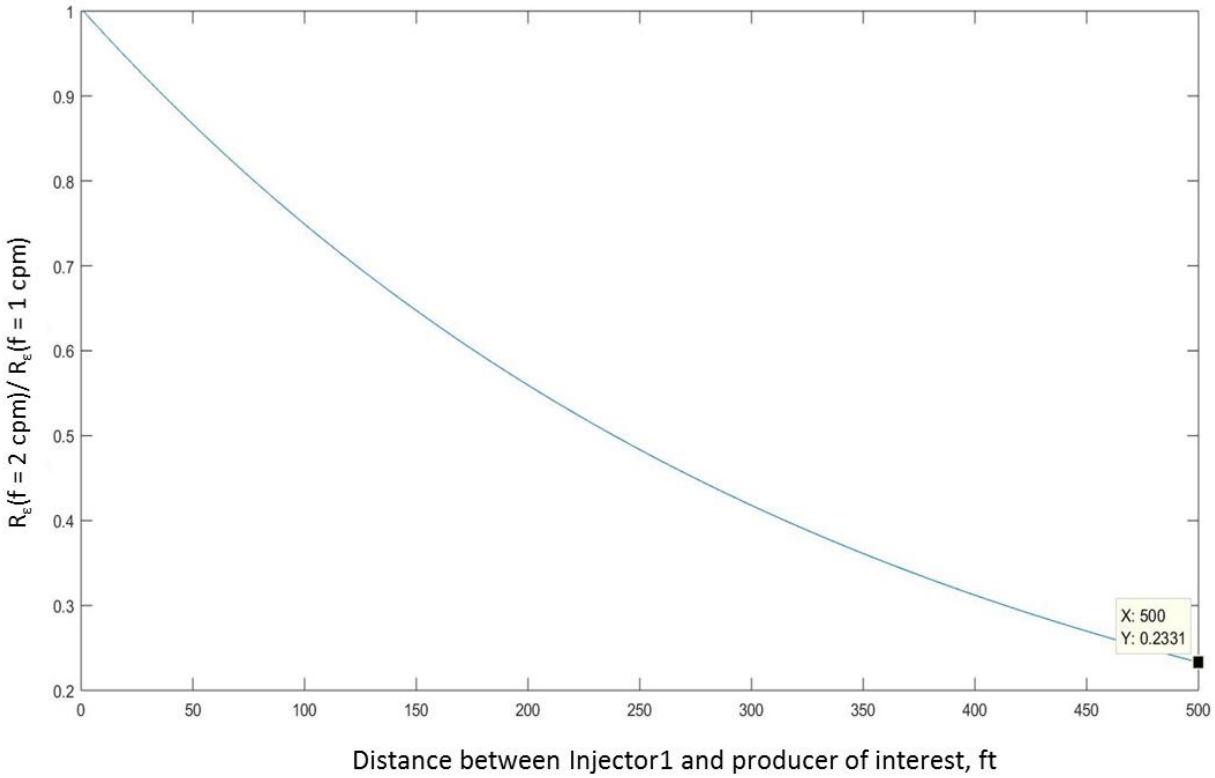

Figure 4.5 R_ε ratio for frequencies of 1 and 2 cpm versus interwell distance plot

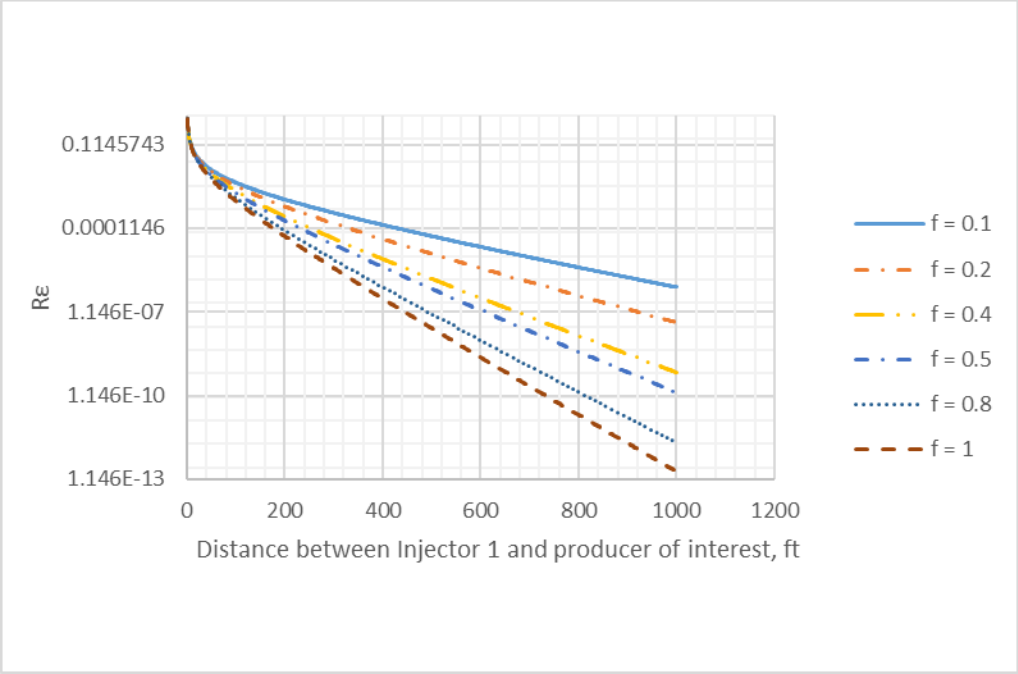

Figure 4.6 For D=211 md*psi/ cp, the R_ε plots for the frequency range of 0.1 and 1 cycle per month (cpm)

In very low permeability reservoirs, vertical wells are inferior to multi-fractured horizontal wells. Still, we consider the vertical well case in these reservoirs. Therefore, we analyzed cases for permeabilities of 1 µd (D = 21.1E-3 md*psi/ cp) and 10 µd (D = 210.97E-3 md*psi/ cp) to emulate very tight and tight reservoirs, respectively. For k = 1µd and D = 21.1E-3 md*psi/ cp, we observed that a decreasing signal frequency causes a large increase in the ratio of R_ε (**Figure 4.7**). The ratio of R_ε starts to increase when the interwell distance exceeds 1000 ft. For D > 2109.7 md*psi/ cp, the effect of decreasing signal frequency on the R_ε ratio decreases as model diffusivity increases (**Figure 4.8**). To conclude, for vertical wells, decreasing model diffusivity boosts the impact of decreasing source signal frequency tenfold on the ratio of R_ε.

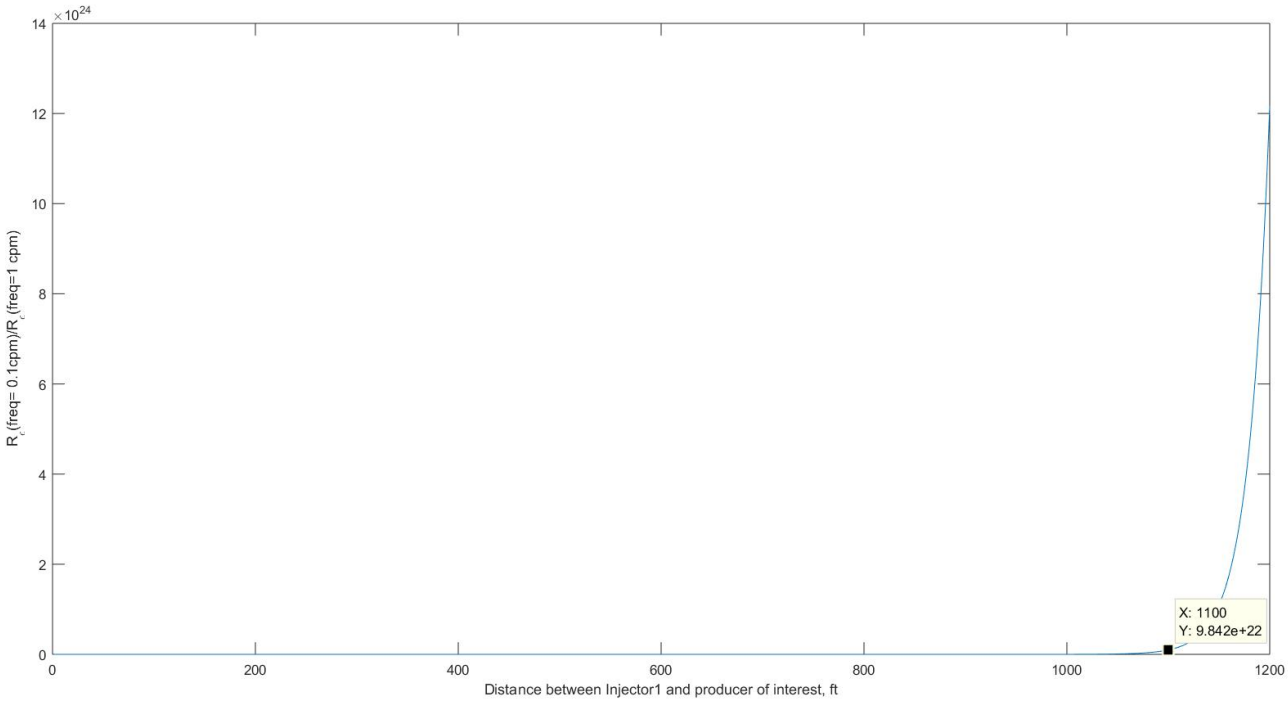

Figure 4.7 R_ε ratio plot for k=1μd (D=21.1E-3 md*psi/ cp)

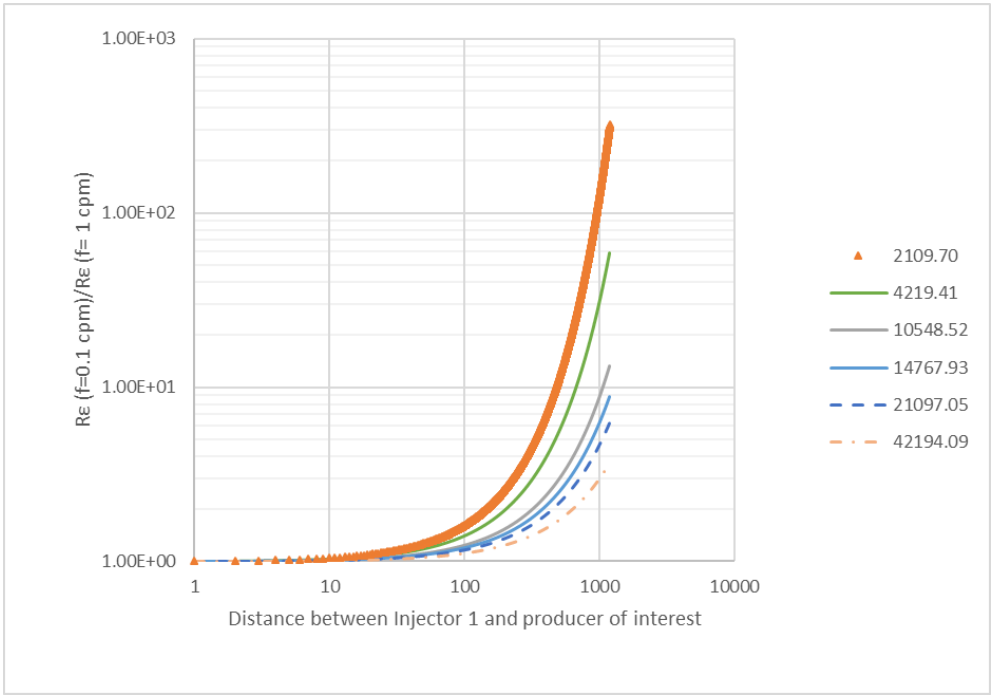

Figure 4.8 For vertical wells, the R_ε ratio for diffusivity range of 2109.7 to 42194.1 md*psi/ cp.

4.2.2 Horizontal wells

Multi-fractured horizontal wells are used to exploit low-permeability reservoirs. During secondary recovery, horizontal wells may be arranged to form a sequence of injectors and producers. We can regard fractured/open hole horizontal wells as line sources (injector) and sinks (producer) with periodic heat liberation at rate $\rho c e^{i\omega t}$ per unit length. Integrating from time $t = -\infty$ to $t = t$ gives us the temperature at the distance r away from the line source (Carslaw and Jaeger, 1959):

$$v' = \frac{1}{2\pi K^*} e^{i\omega t} K_0[r\sqrt{\frac{i\omega}{K^*}}] \qquad \ldots (4\text{-}5)$$

where K^* *is heat conductivity.* After replacing K^* with diffusivity, we can calculate the well emittance rate similar to Section 4.2.1:

$$\varepsilon = \frac{1}{2\pi D} e^{i\omega t} K_0[r\sqrt{\frac{i\omega}{D}}] \qquad \ldots (4\text{-}6)$$

In the case of line source, the well emittance rate ε is a coefficient, which, upon multiplying with an injection well bottomhole pressure change for a single time step, gives us the approximate intensity per unit injection rate created by the injection well a distance r away. If we normalize the Injector 1 ε with respect to the ε of the Injector at a distance of 1 ft (highest emittance) from the target producer, we get

$$R_\varepsilon = \left| \frac{K_0[r\sqrt{\frac{i\omega}{D}}]}{K_0[\sqrt{\frac{i\omega}{D}}]} \right| \qquad \ldots (4\text{-}7)$$

R_ε is the ratio to analyze the effects of frequency f (in lieu of ω) and D on the injection well impact on any producer at a distance r away. R_ε for horizontal wells increases with increasing diffusivity (**Figure 4.9**). Unlike diffusivity, R_ε decreases with increasing frequency (**Figure 4.10**). This is similar behavior to that observed for vertical wells. The plots reveal that R_ε has a decreasing trend with respect to the interwell distance.

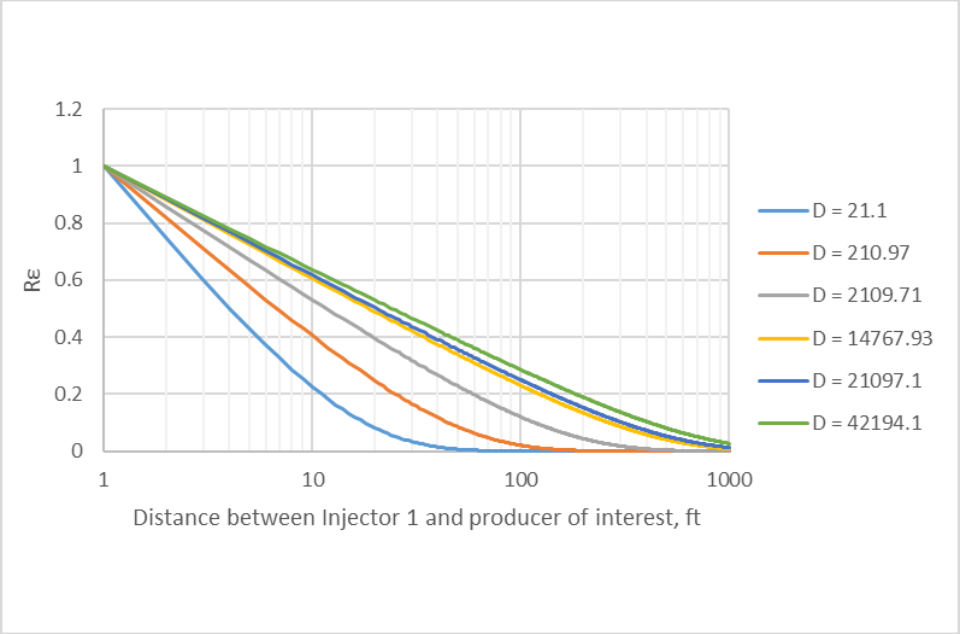

Figure 4.9 R_ε plots for diffusivity range of 21.1 and 42194.1 md*psi/ cp

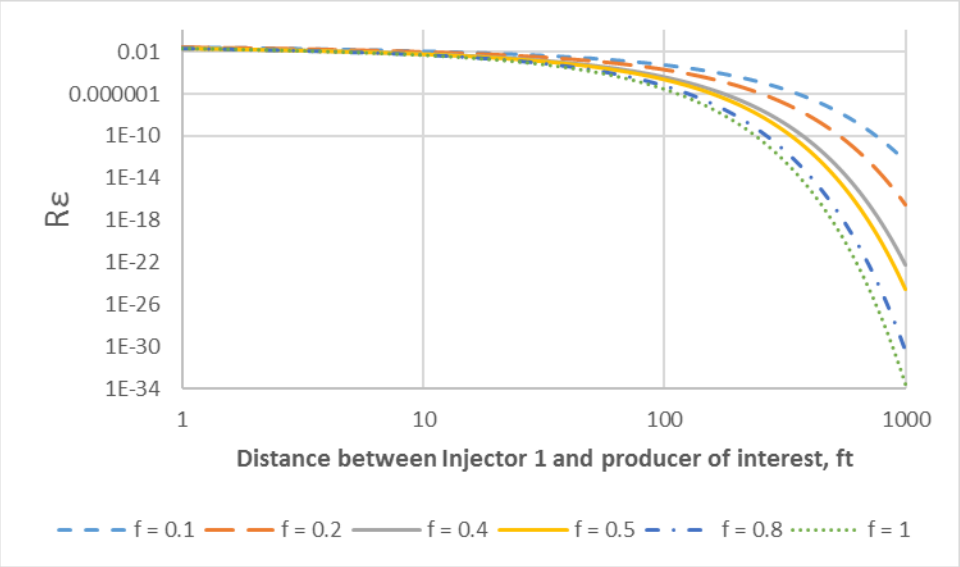

Figure 4.10 For D = 21.1 md*psi/ cp, R_ε plots for frequency range of 0.1 and 1 cycle per month (cpm)

For D > 2109.7 md*psi/ cp, the effect of decreasing the signal frequency by tenfold upon the R_ε ratios decreases as model diffusivity increases, which is similar to the vertical well case (**Figure 4.11**). The difference between R_ε ratios becomes higher as interwell distance increases.

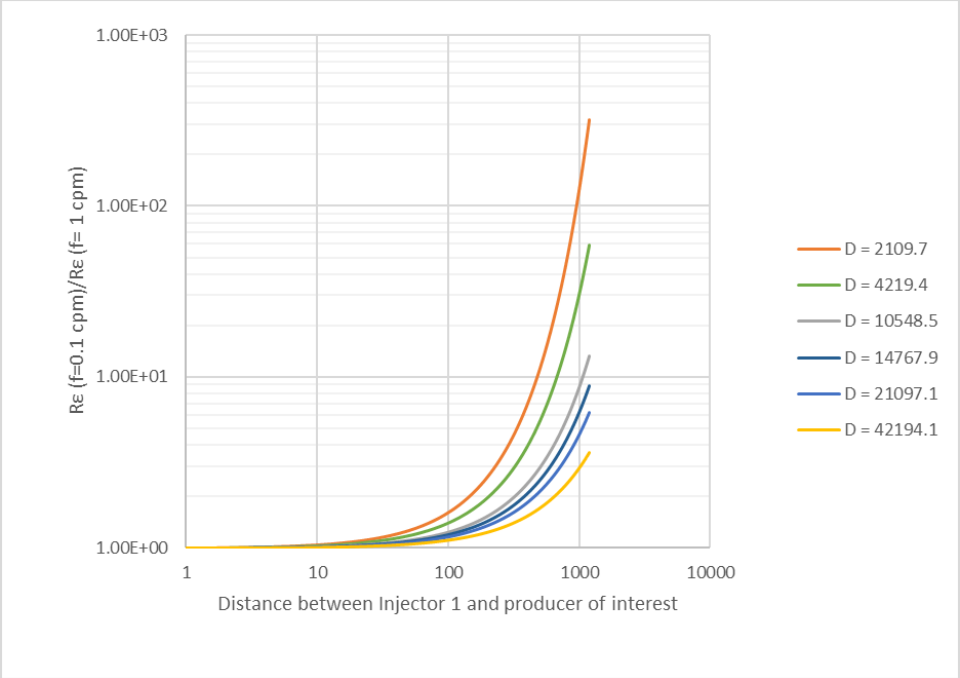

Figure 4.11 For horizontal wells, the R_ε ratio plots for diffusivity range of 2109.7 and 42194.1 md*psi/ cp.

4.3 Procedure for determining window size for the CM-PW application

Both in horizontal and vertical cases, we observe that the diffusivity and frequency have similar effects on R_ε. Here, we confine our attention to the horizontal well scenario, as this will be a common situation in tight reservoirs. To determine an optimum window size employing this plot, we need to find a critical value for R_ε. Then, we can read the corresponding interwell distance. The procedure is as follows:

1- Create a homogeneous simulation model having similar reservoir properties as the field of interest (in our case, we use real field example of the Bakken Forget North pilot waterflood study) (**Table 4.2**). The model has the same field interwell distance (IWD). In the model, there will be an injector and line of producers (**Figure 4.12**).

2 – Create a sinusoidal injection signal with the selected injector frequency spectrum. The Injector1 has a frequency of 1/3 cycle per months (cpm) (**Figure 4.13**).

3 – Simulate the model and acquire flow rates.

4 – Estimate λs using simulated flow rates in the CM-PW application and plot λ vs IWD (**Figure 4.14**). We set $\lambda_{\text{cut off}} = 0.1$ which can be assumed as representing a negligible interaction with other producers in the field. Then, we read the corresponding IWD for this cut off value (**Figure 4.15**). For $\lambda_{\text{cut off}} = 0.1$, IWD = 1080 ft.

5 – Estimate frequency spectrum of surrounding injectors around the injector of interest using the Fast Fourier Transform.

6 – Prepare area R_ε plot employing area diffusivity and median frequency.

7 – In the area R_ε plot, read the critical R_ε at IWD found in Step 4 (**Figure 4.16**). The area has median f = 0.01 cpm. For IWD = 1080, $R_{\varepsilon\,\text{crit.}} = 2.0*10^{-16}$.

8 – With $R_{\varepsilon\,\text{crit}}$, find areal window size using the injector R_ε plot (**Figure 4.17**). The window size/radius of influence of the Injector1 is approximately 1857 ft.

The distance between Injector1 and Producer1 is 660 ft. The producers also have IWD = 660. For the radius of influence of 1857 ft, we should include Producers 1 and 2 in our analysis. The wells beyond 1857 ft are expected to have $\lambda < 0.1$. Therefore, we exclude those wells from our analysis.

Table 4.2 Reservoir Simulation model parameters

Parameter	Value
Porosity, ϕ, fraction	0.1
Horizontal k, md	0.09
Total compressibility, c_t, psi^{-1}	3×10^{-6}
Water viscosity, μ, cp	0.96
Oil end point k_r	1
Water end point k_r	1
Reservoir size in x-direction, ft	4500
Reservoir size in y-direction, ft	6500
Formation thickness, ft	21
Reservoir depth, ft	1960
Reservoir pressure, psi	2822
N_x	225
N_y	325
N_z	3

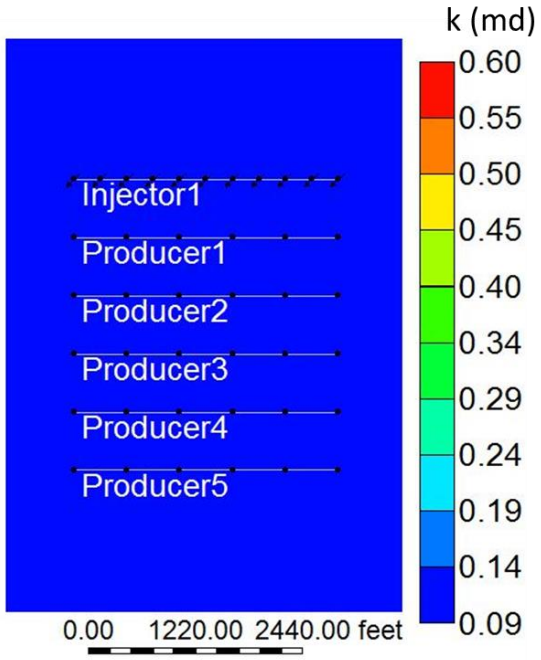

Figure 4.12 Schematic view of a homogeneous simulation model with an injector and 5 producers

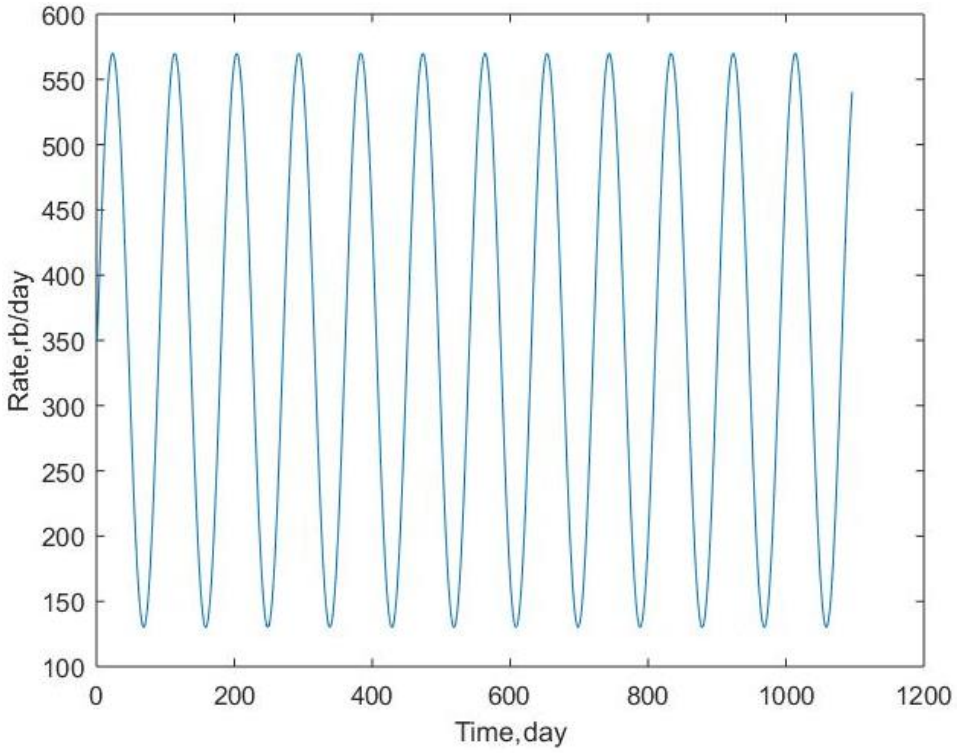

Figure 4.13 Injector1 sinusoidal injection rate with f=1/3 cpm

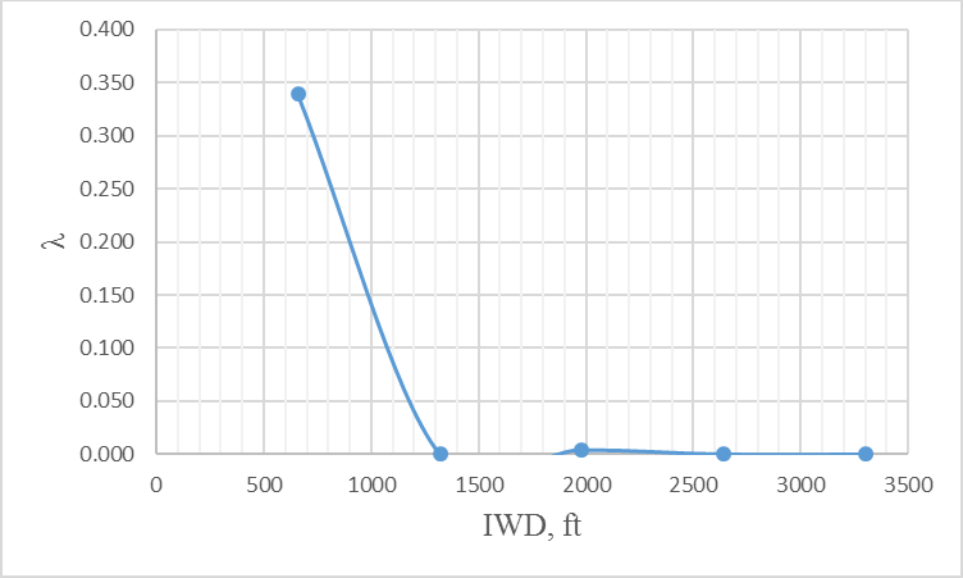

Figure 4.14 λ vs IWD plot

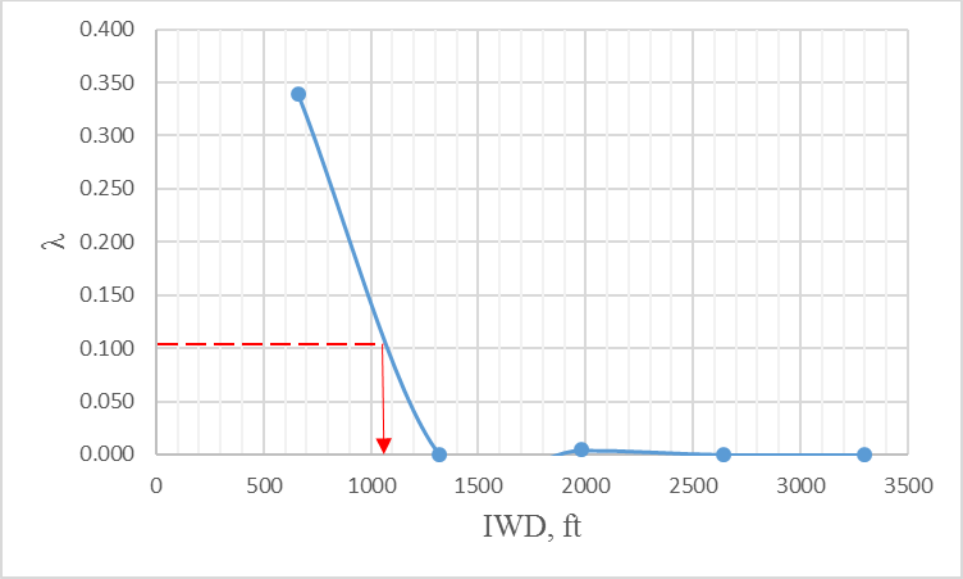

Figure 4.15 Corresponding IWD at $\lambda_{cut\ off}$ = 0.1. IWD = 1080 ft.

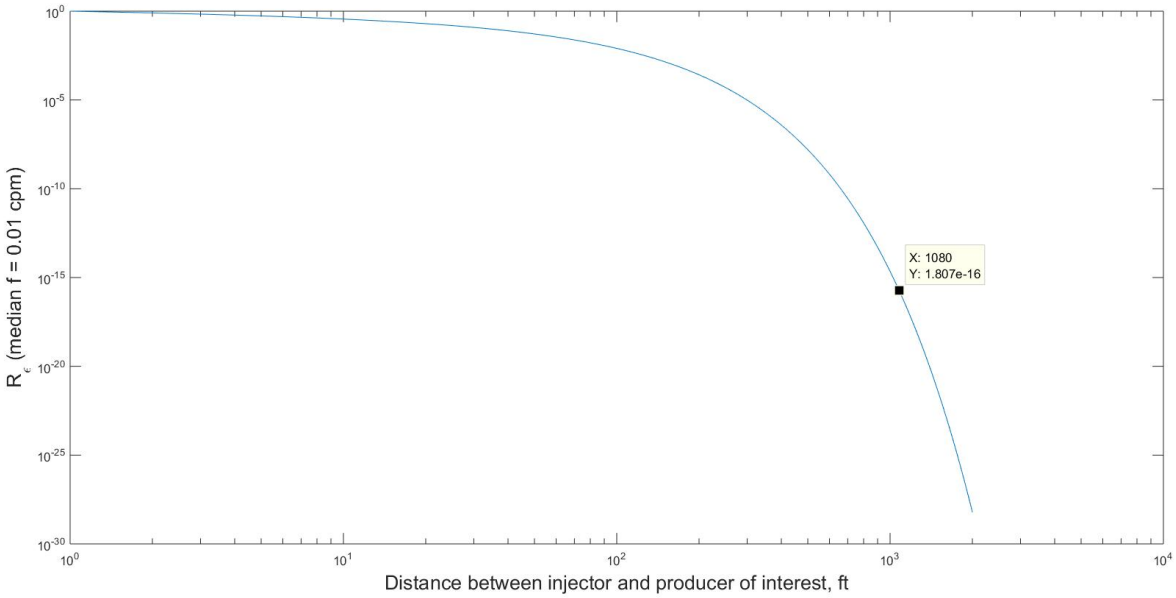

Figure 4.16 Area Rε plot. The critical Re at IWD = 1080ft

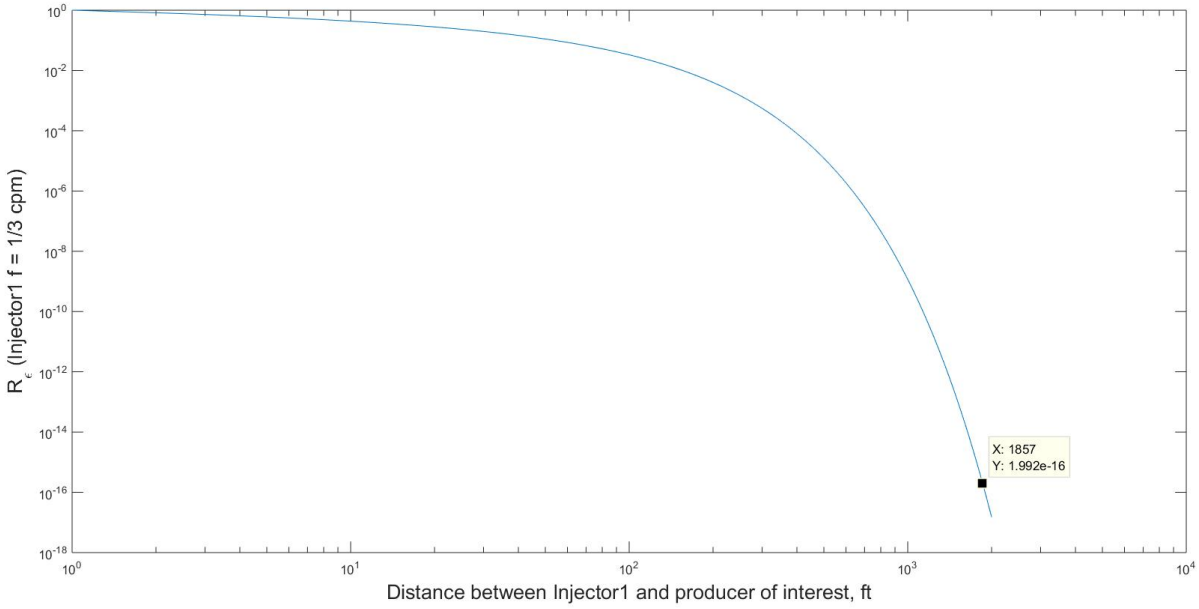

Figure 4.17 Injector1 Rε plot. For the critical $R_\varepsilon = 2.0*10^{-16}$, IWD = 1857ft

To test how the analogy is affected with noise, we added noise starting from 5% up to 40% to flow rates. We observed the analogy works well with up to 30% noise. The analogy fails when noise reaches 40% (**Figure 4.18**).

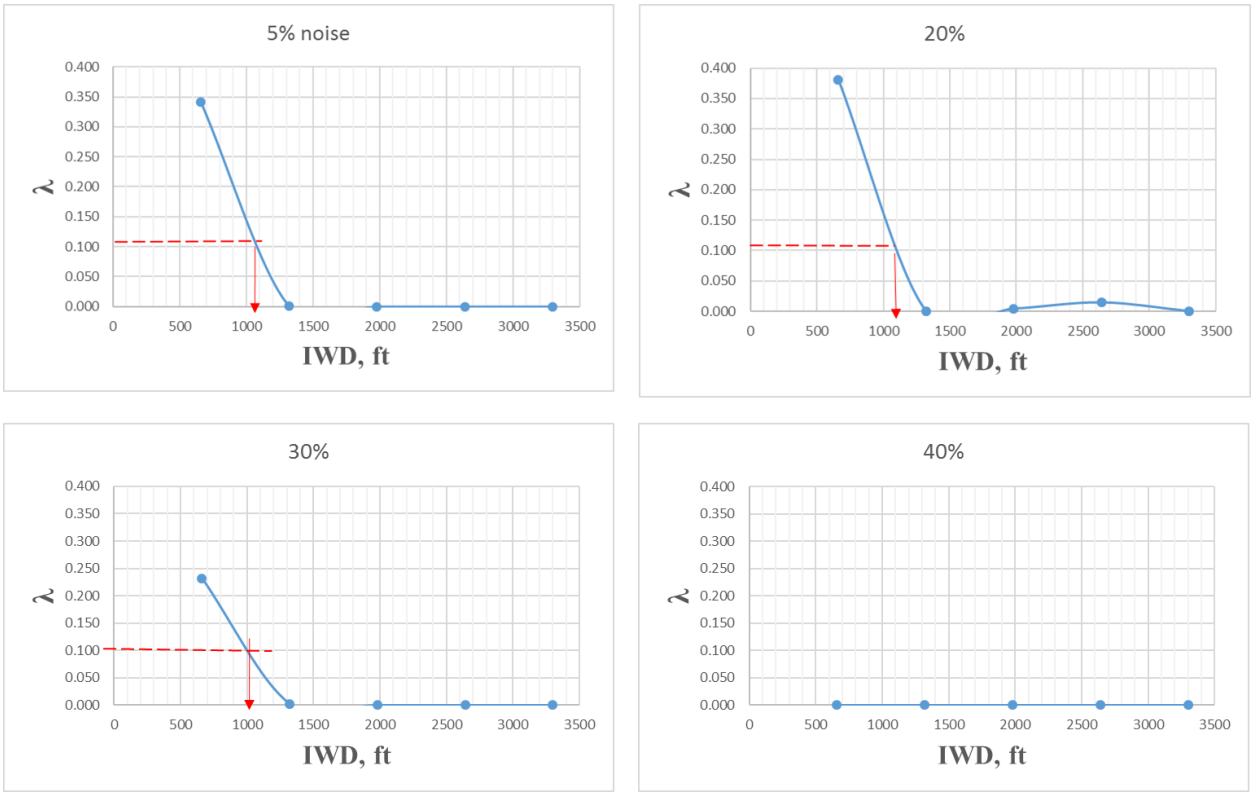

Figure 4.18 λ vs IWD plots when noise added to production rates. The model fails when 40% noise added to production rate. λs are zero for all IWDs.

The particular value of $R_\varepsilon = 2.0*10^{-16}$ represents the degree of the disturbance felt at the target well due to the disturbance created in an injection well with frequency f. In other words, for IWD = 1857 ft, R_ε shows what will be the normalized well effectiveness on the target well.

4.4 Conclusions

The diffusivity and injection rate frequency have a large effect on the successful application of the CM in tight reservoirs. We analyzed the effects of these variables on well emittance rate and its ratio R_ε. The well emittance rate decreases as interwell distance (IWD) increases. R_ε increases with increasing diffusivity, which shows injector impact on producer increases in high diffusivity model. Increasing frequency results in a decrease of R_ε. With R_ε ratio, we can find a diffusivity value at which frequency change will not affect well emittance rate. Both vertical and horizontal

wells have similar behavior with respect to diffusivity and frequency. Use of R_ε and λ plots with respect to the IWD helped us to determine approximate injector radius of influence/window size.

CHAPTER 5: FIELD CASE STUDY OF THE HALO OIL FIELD EAST PEMBINA: CARDIUM FORMATION

The Cretaceous Cardium Formation was named by Scottish geologist James Hector because of the fossilized cockle (Cardiidae) shells it contains (Braunberger et al., 2001). Looking at a regional map at 90 million years (MA) ago, we see the conditions present when the Cardium Formation was formed (**Figure 5.1**). The Western Interior Seaway divided the continent from north to south and with an arm extending to the east. The area later known as the Alberta province shows a majority of the province belonged to this Western Interior Seaway region. Cardium Formation paleogeographic maps depicted by Krause et al. (1994) (**Figure 5.2**) indicate that probably the whole Cardium Formation and the oil it contains are due to the Western Interior Seaway. From these maps, we observe that a large majority of the formation has been deposited within the sea covered areas.

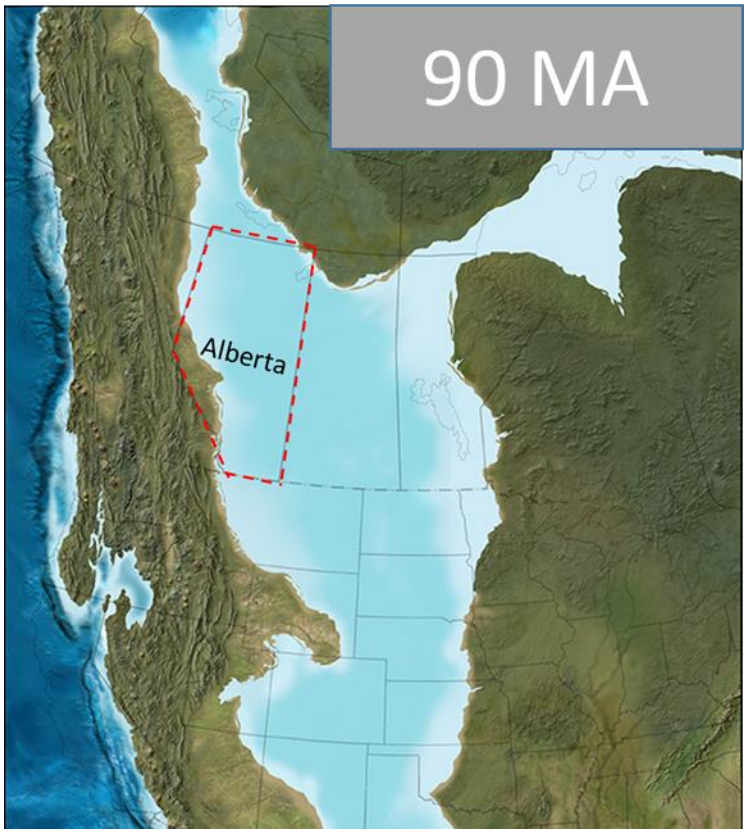

Figure 5.1 Map of Western Interior Seaway from the North America Continent before 89 MA. The current border of Alberta is shown with red dashed lines. Figure adapted from Blakey (2017).

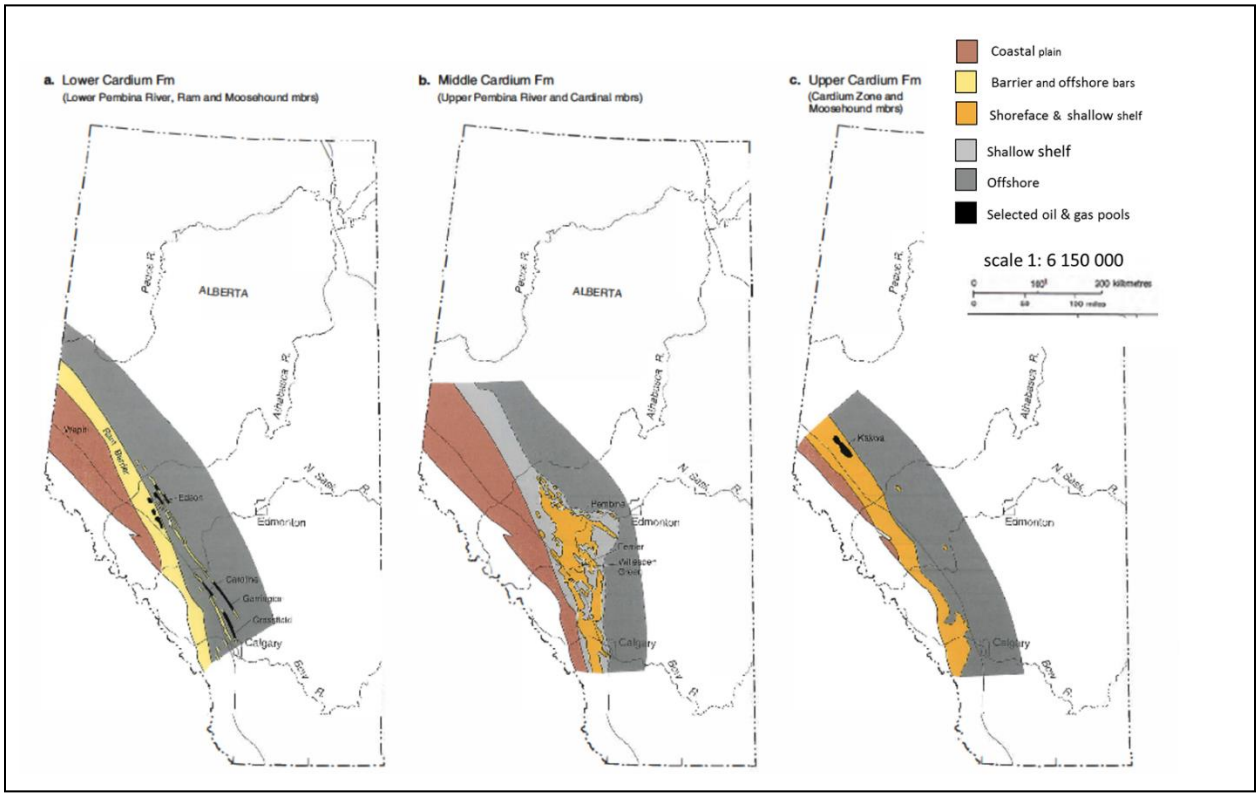

Figure 5.2 Cardium Formation paleogeographic maps: a. Lower Cardium formation, b. Middle Cardium Formation, c. Upper Cardium Formation (Modified from Krause et al., 1994).

Krause and Nelson (1984), as cited in Krause et al. (1994), divided the Cardium Formation into 2 stratigraphic subdivisions: the Cardium Zone and Pembina River Members (**Figure 5.3**). The Pembina River Member comprises the reservoir and underlying sealing shales. The reservoir is heterogeneous and weakly stratified. Krause et al. (1987) reported the Pembina Member contains 82% of initial oil-in-place of the major Cardium Formation pools. The Cardium Zone Member is characterized by capping siltstones and black shales.

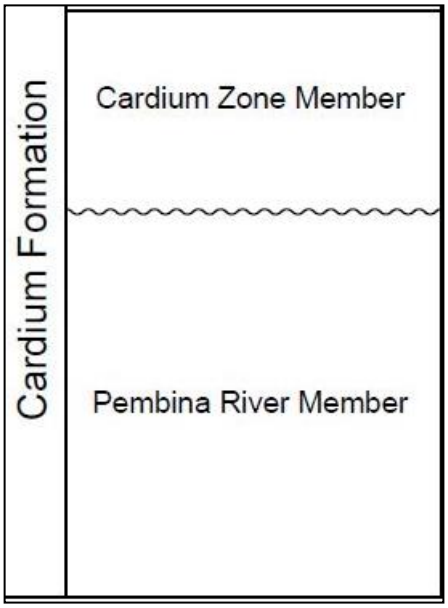

Figure 5.3 Cardium Formation stratigraphic subdivisions in the subsurface (Modified from Krause et al., 1994)

Reservoirs in the Cardium Formation have been found in the depth range of 1200 – 2700 m (Krause et al., 1994). Neighboring source rocks generated the light and sweet hydrocarbon found in these reservoirs (Krause et al., 1994). The Cardium Formation has been exploited since the 1950s, with exploitation moving from conventional, high-permeability areas to tighter, low-permeability regions. Today, the low permeability deposits of the Cardium Formation have become attractive zones to target as technological advancements (e.g., horizontal wells with multistage fractures) have made it economically viable.

Krause et al. (1987) indicated that five lithofacies characterize the field (**Tables 5.1 and 5.2**). The conglomerate is distributed discontinuously and is seen as one of the most troublesome lithohydraulic units in the reservoir as injected fluids are likely to channel through it, leading to early water breakthrough and small oil recoveries (Krause et al., 1987; Kloepfer and Griffith, 1965; and Gillund, 1969).

Fic's (2013) permeability study for each lithofacies from three selected representative cores in the East Pembina Oil Field shows that permeability ranges from 0.1 md up to 330 md, excluding the conglomerate interval. Average permeability in the conglomerate is 160 md (Krause et al., 1987).

Table 5.1 Lithofacies in Cardium Formation (Krause et al., 1987)

Lithofacies	Lithology	Subfacies
Lithofacies 5 (top)	Conglomerate	5A, 5B, 5C
Lithofacies 4	Medium to thick-bedded, very fine and fine-grained sandstone	-
Lithofacies 3	Thin and very thin-bedded shale, siltstone, and very fine and fine-grained sandstone	-
Lithofacies 2	Bioturbated, thin and very thin-bedded shale, siltstone and very fine and fine-grained sandstone	-
Lithofacies 1 (bottom)	Dark-gray shale and siltstone	1M, 1L, 1B

Table 5.2 Subfacies of main lithofacies (Krause et al., 1987)

Subfacies	Lithology	It contains...
1M	Massive gray shale and siltstone	less than 10% sand content
1L	Laminated dark-gray shale and siltstone	10-30% silt- and sand-size material
1B	Bioturbated dark-gray shale and siltstone	10-30% silt- and sand-size material, bioturbated more than 30%
5A	Sandstone and sandstone matrix-supported framework. It forms clast.	less than 10% shale, and 30% of particles greater than 2 mm
5B	Shale, silt, and conglomerate. Evident bioturbation in shale and silt fraction	more than 10% shale and silt, and conglomerate may represent 5-90% of particles
5C	cemented by poikilotopic calcite and coarse-grained siderite	Granule to pebble-sized chert and quartz clasts with varying matrix compositions

Sandbody continuity is a major concern for the Cardium Formation. Krause et al. (1987) observed that in their study area, from south-central Pembina field (T47, R7 W5M) with good core coverage, lithofacies are formed as mosaic and lack continuity i.e., labyrinth in the terminology of Weber and van Geuns (1990). Interbedding, lensing, and shingling prevail in lithofacies and lithohydraulic units. Krause et al. (1987) assume that the lithofacies extend halfway between wells, a distance of approximately 285m, for their analysis. Butrenchuk et al. (1995) noted that high lateral continuity would be anticipated in the sandstones and shales with their suggested depositional model of a prograding shoreline stepping out into the basin, suggesting a more continuous system (i.e., jigsaw puzzle in the Weber and van Geuns (1990) characterization) than Krause et al. (1987) do. Repeat Formation Tester pressure data from infill drilling revealed that

the tested sands were being drained by the surrounding producing wells at 80-acre spacing (i.e., about 570m). Plint et al. (1986) reported that sedimentation during depositional environments was periodically disturbed by episodes of lowered sea level, which resulted in the regional erosion of both the shoreline and offshore sediments, reducing lateral continuity. Amid these lowstand periods, conglomeratic sediments were deposited. Gillund (1969) observed that 86% of the injected fluid flowed into the conglomerate layer (as cited in Krause et al., 1987). When it comes to fluid preferential flow, in addition to the conglomerate, natural fractures also play an important role.

Fractures

Determining fluid production trends has been a significant challenge in the Cardium Pool. Many authors (Hassan, 1982; McLeod, 1978; Gough and Bell, 1981; Krause et al., 1987) have studied this topic. It was the prevailing opinion that either a capping conglomerate layer or fractures controlled these trends. Nevertheless, it was not clear which one of these was affecting production on a well basis. Gough et al.'s (1983) study of stress provinces depicts the Mid – Continent Stress Province of North America. They employed borehole breakouts determined from four-arm dipmeter logs to identify the maximum stress (S_{Hmax}) orientation. They determined that the NE – SW orientation of S_{Hmax} extends throughout the Western Canadian Sedimentary Basin (WCSB), northeast of the Rocky Mountains of Alberta and British Columbia. Additionally, Bell et al. (1994) stated that "fractures running NE-SW, which are subparallel to S_{Hmax} in the Western Canada Sedimentary Basin, are likely to be more resistant to closure than those oriented NW-SE, parallel to S_{Hmin} trajectories". Krause et al. (1987) determined that fractures control the NE – SW-oriented water breakthroughs occurring over short periods.

As we will demonstrate, with the help of interwell connectivity analysis and maps, we can determine the dominant fluid production trends in a specified area and assess lateral continuity, which can help us to exploit an area of interest and compare with the geological findings. Connectivity assessments can help to identify the major geological controlling factors and provide a guide to well spacing for infill drilling campaigns. IWC can also help to understand how connectivity changes when wells are stimulated.

5.1 East Pembina Field Description and Geology

Our study area is the East Pembina Oil Field (**Figure 5.4**), where the average permeability is less than 1 mD**.** The field was initially drilled on 80- and 160-acre well spacings for wells in the Range 7 – Township 50 and Ranges 6-5 – Township 49 areas, respectively. Most of the wells in the field (**Figure 5.4-B**) were vertical wells. More recently, horizontal wells have been added. Most of the vertical wells were fracture stimulated during initial completion. A majority of the wells have been periodically retreated.

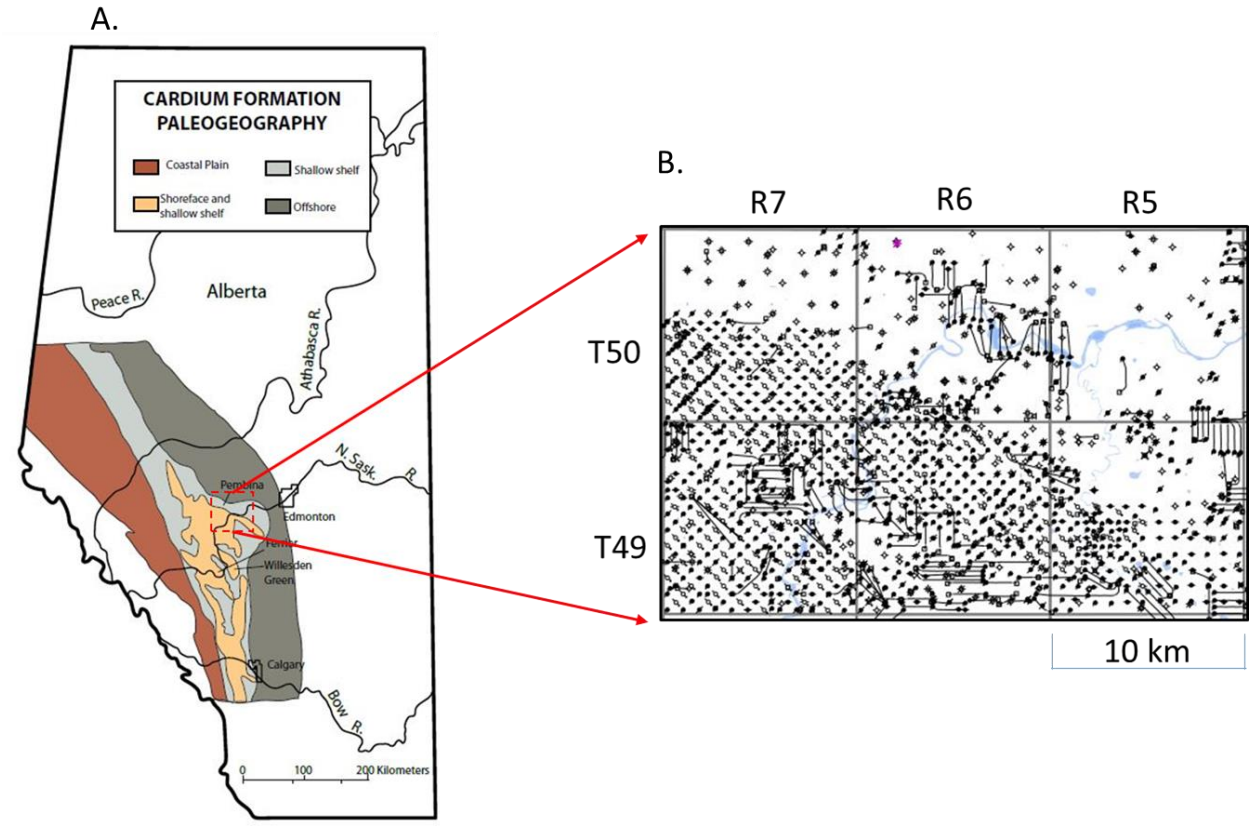

Figure 5.4 (A) Alberta map showing Cardium Formation paleogeography (Modified from Krause et al. (1994) as cited in Fic, 2013) and (B) Enlarged map of the East Pembina Oil Field well locations.

Krause et al. (1994) provide a conglomerate isopach where conglomerates are generally orientated NW-SE and the indicated thickness varies from less than 0.1 to more than 9m in this area (**Figure 5.5**). Krause et al. (1987) report that the conglomerate-bearing zone has thickness ranging from one pebble to 12m. They observed that conglomerates thinner than 1m are packed with shale or siderite matrix and do not have a large influence on fluid flow.

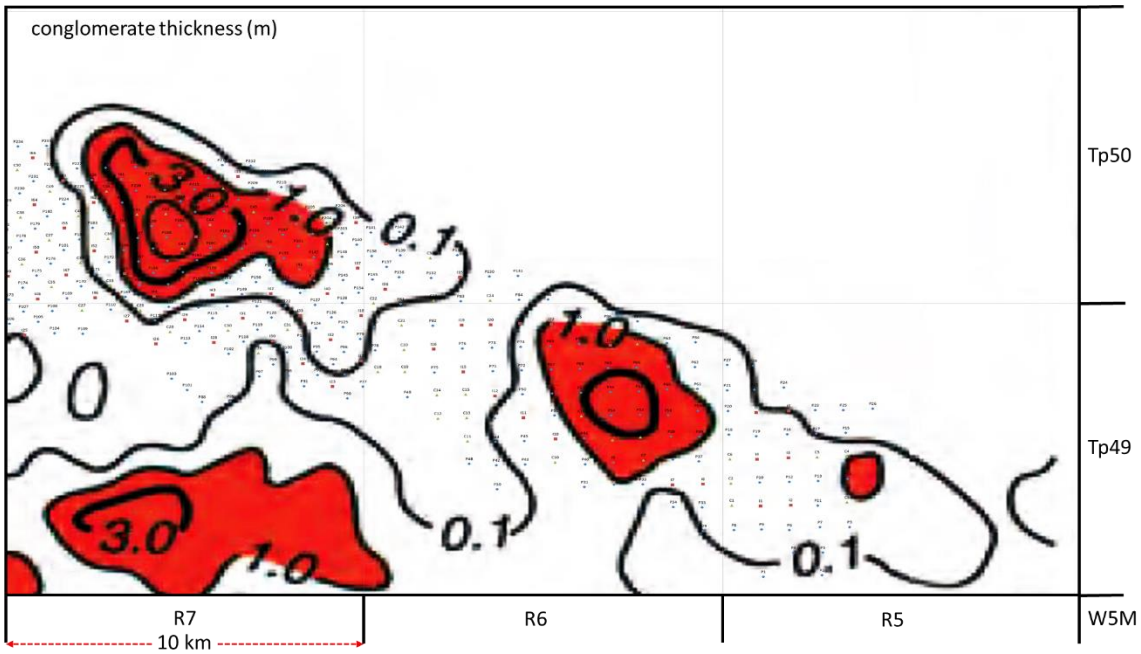

Figure 5.5 Conglomerate thickness map of the East Pembina Oil Field (Edited from Krause et al., 1994). Conglomerate thickness varies from 0.1 to 9 meters in this area. Contours are in meters: 0.1, 1.0, 3.0, and 9.0.

5.2 IWC Evaluation in Selected Window Areas

In this section, we use the CM-PW to evaluate IWC in two areas from the East Pembina Field (**Figure 5.6**). The field was under primary depletion until 1967, when waterflooding began. **Table 5.3** (Clarkson et al., 2011) summarizes some of the important reservoir and fluid properties. Two areas (windows) were chosen to study the effects of geology and well treatments on IWC.

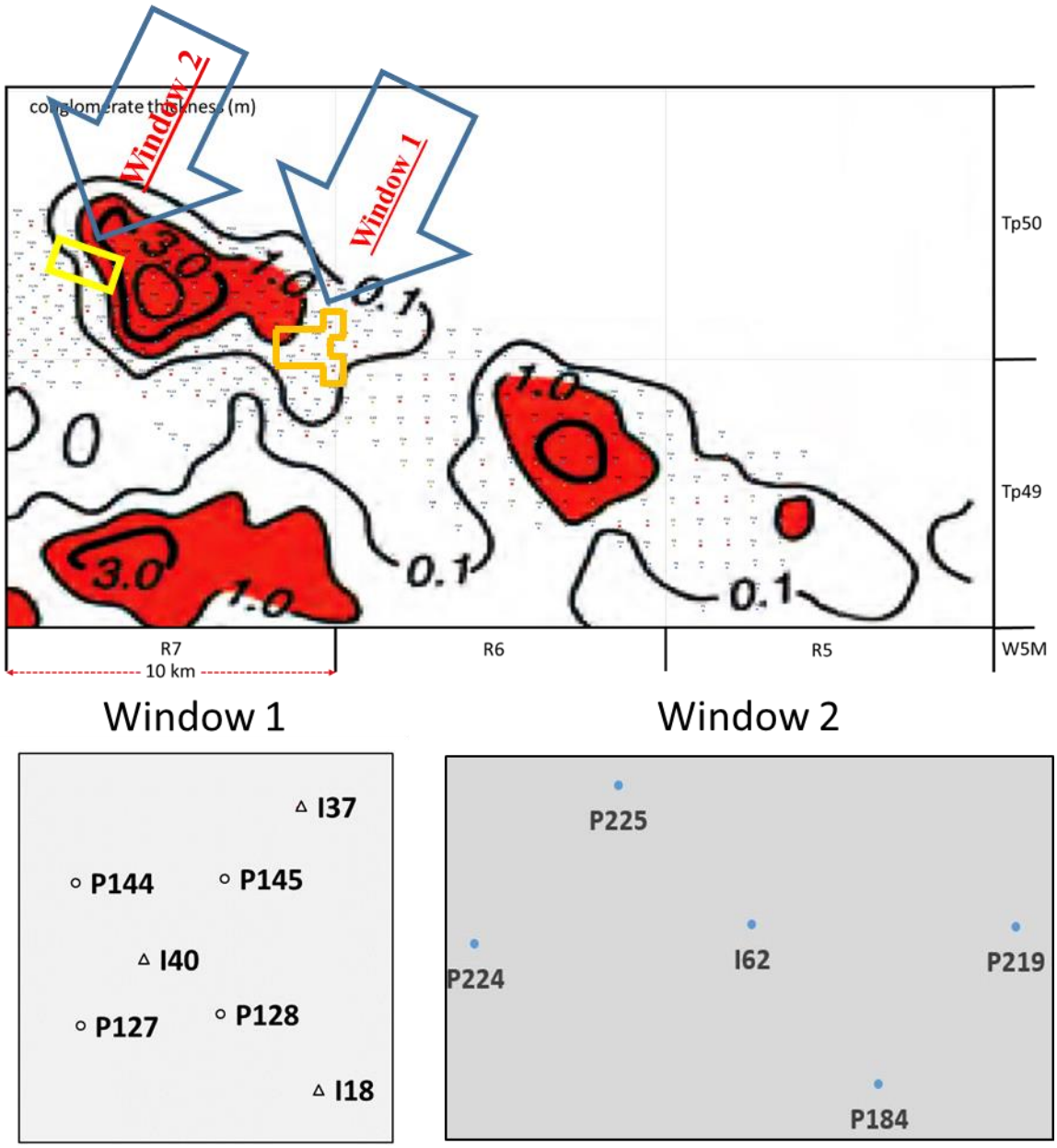

Figure 5.6 The East Pembina Oil Field – conglomerate thickness map (edited from Krause et al. 1994); Contours are in meters: 0.1, 1.0, 3.0, and 9.0. Orange colored outlines are the chosen window areas.

For the connectivity evaluation presented below, we use a normalized connectivity measure, λ', instead of λ. The normalized connectivity λ', $\lambda' = \lambda_{hetero} - \lambda_{homo}$, where λ_{homo} is the connectivity if the reservoir is homogeneous and λ_{hetero} is the connectivity for the actual reservoir, reduces the effects of well distance and reservoir boundaries from the connectivity, as both λ_{hetero} and λ_{homo} contain these effects (Kaviani and Jensen, 2010; Soroush et al., 2014). λ_{homo} is calculated

analytically using the Multiwell Productivity Index method (Kaviani and Jensen, 2010). Hence, interpreting λ' is easier than using λ for the evaluation of reservoir heterogeneity because 1) it facilitates connectivity comparisons for wells with differing injector-producer spacing, and 2) it provides a measure of connectivity relative to that obtained in a homogeneous reservoir. Positive λ' represent flow conduits (more connectivity than a homogeneous reservoir) while negative λ' suggests flow barriers (less connectivity than a homogeneous reservoir).

Table 5.3 Some important East Pembina Field reservoir and fluid properties (Clarkson and Pedersen, 2011).

Reservoir Rock	Cardium sst and Conglomerate
Age	U. Cretaceous
Net Pay (Avg.)	19.3 ft
Porosity (Avg.)	13.9%
Permeability (Avg.)	0.7 md
Gravity	37° API
Initial oil viscosity	1.4 cp
Initial oil FVF	1.19 RB/STB
Initial reservoir pressure	~1900 psi

5.2.1 Window 1

5.2.1.1 Optimum window size for the CM-PW application

To determine an estimated window size, we follow the procedure described in Chapter 4 (Section 4.3) and calculate the injection rate frequency spectrum, using the FFT. The injection signal frequency of the central injection well I40 from Window 1 has the strongest component at 0.06 cycle per month (**Figure 5.7**). We choose the peak amplitude in the FFT spectrum, since a sinusoidal component with a large amplitude and small frequency is expected to dominate the signal arriving at a producer well. Selecting the component with peak amplitude as a representative frequency of the signal might not be the best choice because lower frequencies with smaller

amplitudes might actually have more effect at the producer. Nonetheless, we are choosing the largest amplitude component for simplicity in this study.

We also calculated frequency spectrum of surrounding injectors (**Figure 5.9**) to obtain the median frequency that will be used for the sinusoidal injection rate. I37 and I18 have the strongest components at 0.1 and 0.08 cycle per month, respectively. The median frequency is 0.06 cycle per month which is to the same as the I40 frequency. In this case, we skip steps 6, 7, and 8 from Section 4.3 (Chapter 4), since the median frequency equals the I40 frequency. $\lambda_{cut\ off}$ will give us the interwell distance (IWD) for the window size. The simulation model is prepared using properties listed in **Table 5.3**. The homogeneous model has an injector and 5 producers in sequence (**Figure 5.9).** After running the simulation, we estimate the λs. For $\lambda_{cut\ off}$ = 0.1, the IWD is 3620 ft (**Figure 5.10**).

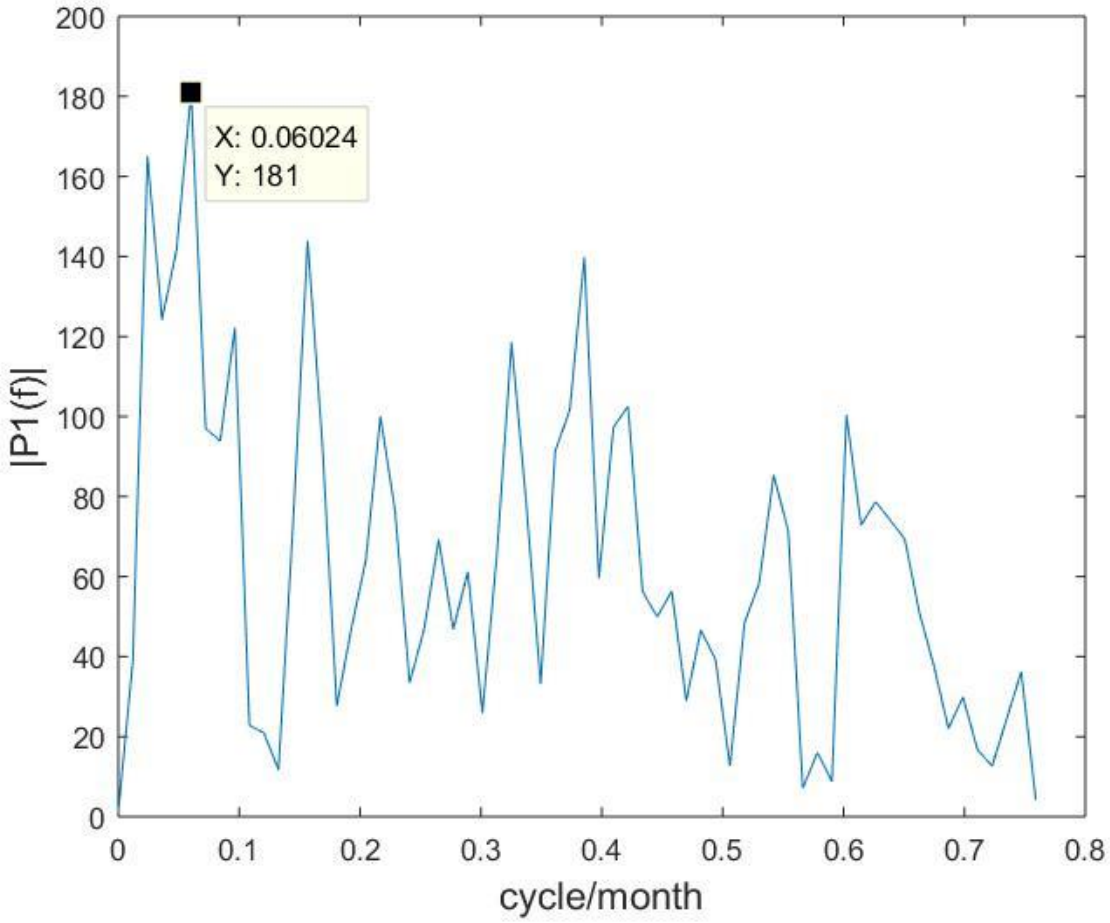

Figure 5.7 FFT periodogram of I40 injection rate

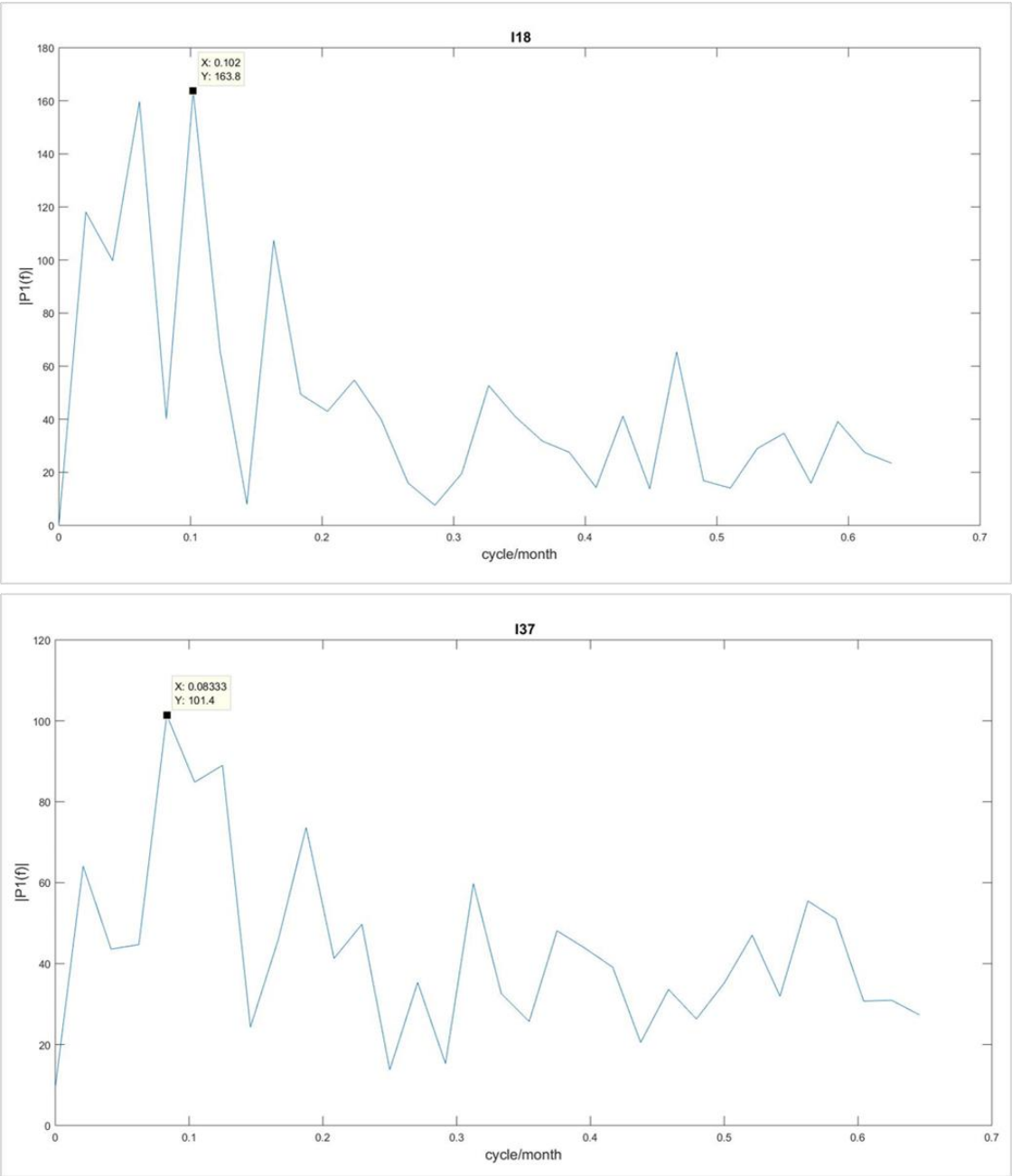

Figure 5.8 I18 and I37 FFT periodograms

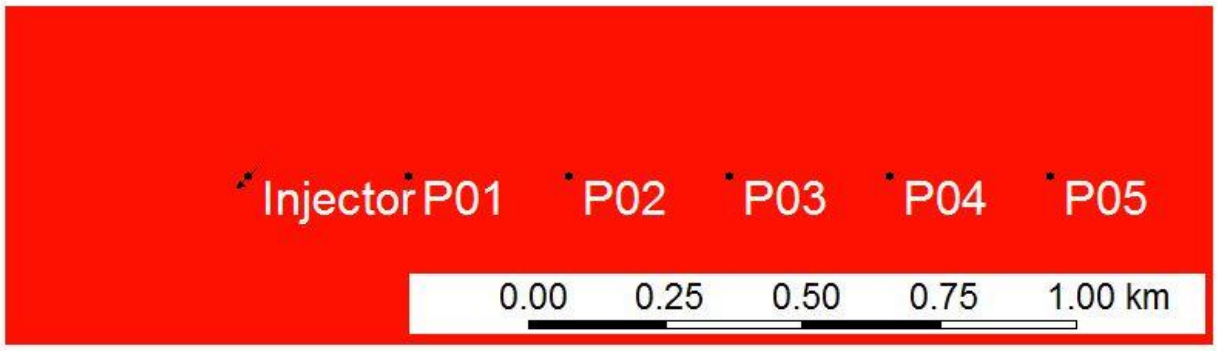

Figure 5.9 Schematic view of a homogeneous simulation model with one injector and 5 producers. The model permeability is 0.7 md.

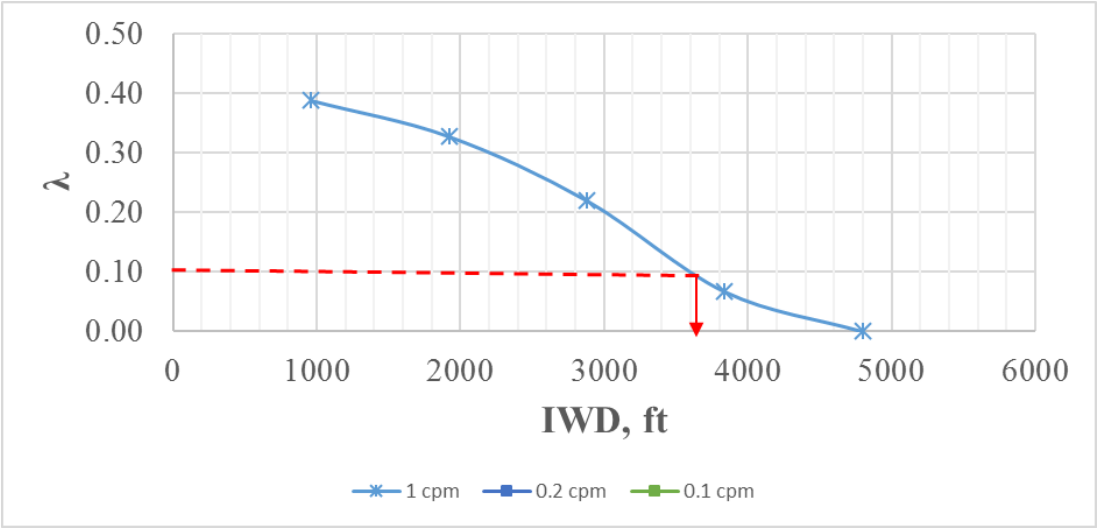

Figure 5.10 Corresponding IWD at λcut off = 0.1

The window size for well I40 could be as large as approximately 3620 ft. The distance of 3620 ft is larger than 160-acre well spacing (2640 ft.). All producers therefore fall within the I40 radius of influence. Beyond this distance, we might expect the injector will have a reduced impact on a producers.

5.2.1.2 CM-PW Analysis

This area is chosen from a location where the conglomerate is thinner than 1 meter. We chose an area including surrounding producers and two injectors I18 and I37, and the CM-PW was applied for three periods (**Figure 5.11**). The R^2 values of all three periods are fair to good (**Table 5.4**). Due to a limited number of measurements for the number of parameters to be evaluated (L = 4.5), the median C_v of λs in the first period are expected to be greater than 0.1 (Kaviani et al., 2014), which might be a reason for the relatively low R^2. Although the second period L = 3.1, we still get better R^2 than that of the first period.

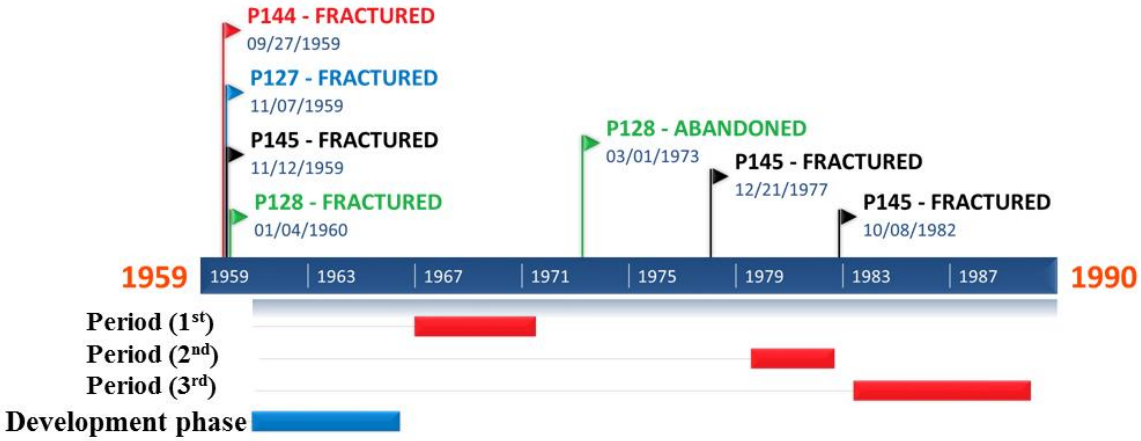

Figure 5.11 Timeline of the Window I40-I37-I18

Table 5.4 Window 1 periods – R^2 values based on total predicted vs total measured production rates during each period

Period	Start Date (dd/mm/yyyy)	End Date (dd/mm/yyyy)	R^2	L
1st	01/01/1967	01/07/1971	0.76	4.5
2nd	01/08/1979	01/09/1982	0.83	3.1
3rd	01/06/1983	01/01/1990	0.91	6.6

Prior to the first period, all four producers were fractured (**Figure 5.11**). The CM-PW analysis (**Figure 5.12**) reveals that the largest connectivities are oriented in the NE-SW direction, which is consistent with the S_{Hmax} direction in the region (Bell et al., 1994). The pseudo well

connectivity is also directed in the NE-SW direction and contributes only to P127 (**Figure 5.13**). According to AER reports, the operator fractured P127 with 37.5 tons of 20/40 sand, which is the largest amount of pumped proppant tonnage when compared to the other wells in Window 1.

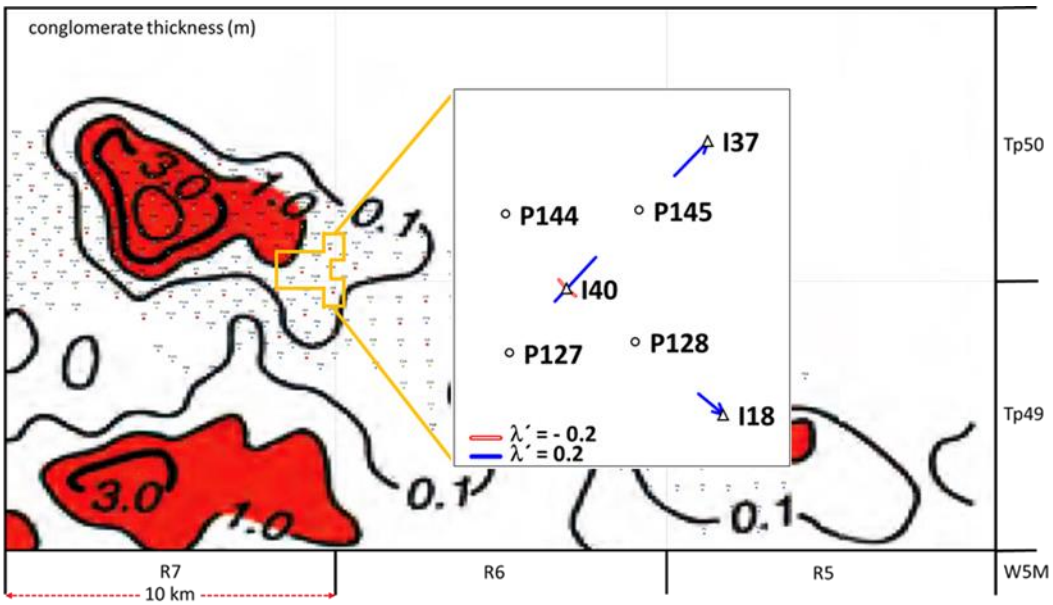

Figure 5.12 Window 1 – normalized connectivity map of the first period. Connectivities are larger in the NE-SW direction, consistent with the direction of larger horizontal principal regional stress.

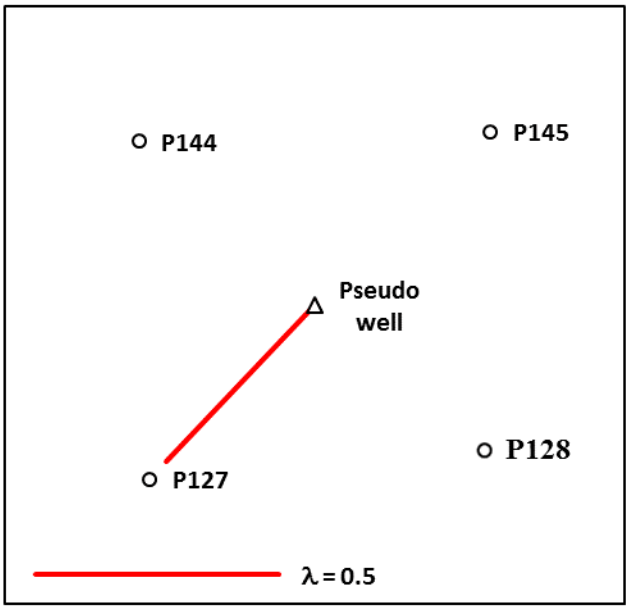

Figure 5.13 Pseudo well connectivity during first period, showing strong connectivity from wells outside the area with well P127.

It appears that fracture stimulation of the high permeability well P128 (core k_{avg} = 190 md) was not productive; it was abandoned (**Figure 5.11**) with a water cut of 95% after 6 years of waterflooding. Before the second period, P145 was fractured again, although the reasons are unclear because the CM-PW analysis suggests this well was adequately supported by both I37 and I40. After the P145 restimulation, the connectivity with I37 and I40 decreased and P127 is the only well having $\lambda' > 0$ (**Figure 5.14**). The connectivity of I40 – P127 may be larger because P127 was fractured initially with 37.5 tons of proppant, which is 12.5 tons more than the amount used to treat P145 during the same period. We cannot further analyze the connectivity change of P144, as we have no information about the fracturing job of that well.

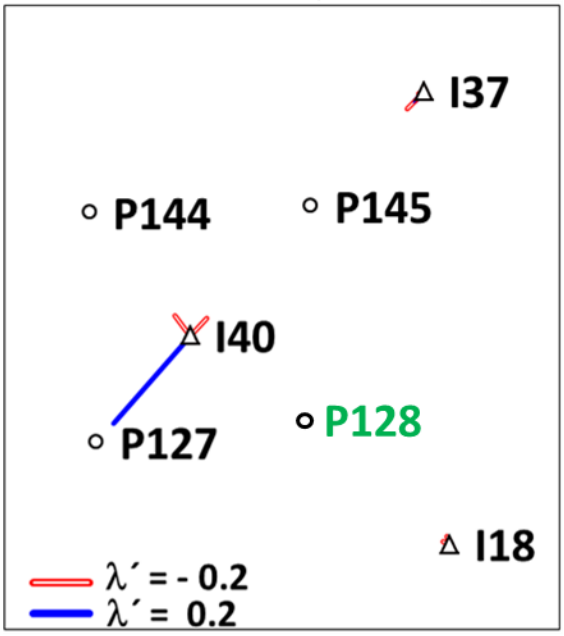

Figure 5.14 Window 1 – normalized connectivity map of the second period (P128 abandoned, P145 refractured in 1977)

The second period analysis, after P128's abandonment and P145's restimulation, shows that P145 does not benefit from the nearby injectors. P145 was fractured for the third time prior to the third CM-PW analysis period (**Figure 5.11**). Further refracturing of P145 does not appear to have been effective (**Figure 5.15**); I40 decreased connectivity with all the surrounding producers.

The slope of a cumulative injection vs. time plot shows the I40 injectivity changes across the three periods and suggests that injection-induced fractures may have been important (**Figure 5.14**). Period 1 shows the steepest slope in **Figure 5.16**, indicating the largest injectivity and exhibits the largest connectivities oriented in the S_{Hmax} direction. The Period 1 slope is approximately 500 bbl/day, which is much larger than the constrained injection rates typical of this field. Hence, injecting water at this rate creates pressures exceeding the formation breakdown unless there is a significant fracture already present. When the slope of the plot decreases in the second period, we observe that the connection with P145 was lost. However, I40 established a strong connection with P127, which was initially fractured with a larger amount of proppant compared to P145. The increased slope in the third period appears to occur in the fracture shear

failure time. Therefore, I40 lost all connections with the surrounding wells. During all three periods, P127 is the only well having strong support from areas outside of the window.

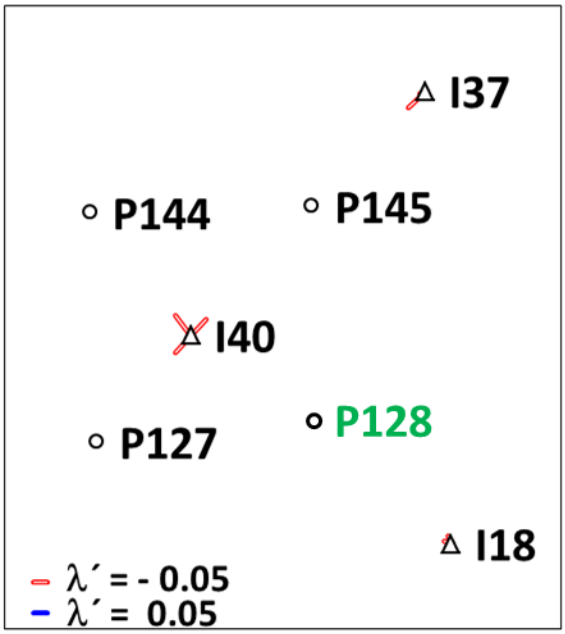

Figure 5.15 Window 1 – normalized connectivity map of the third period (P145 fractured, P128 abandoned)

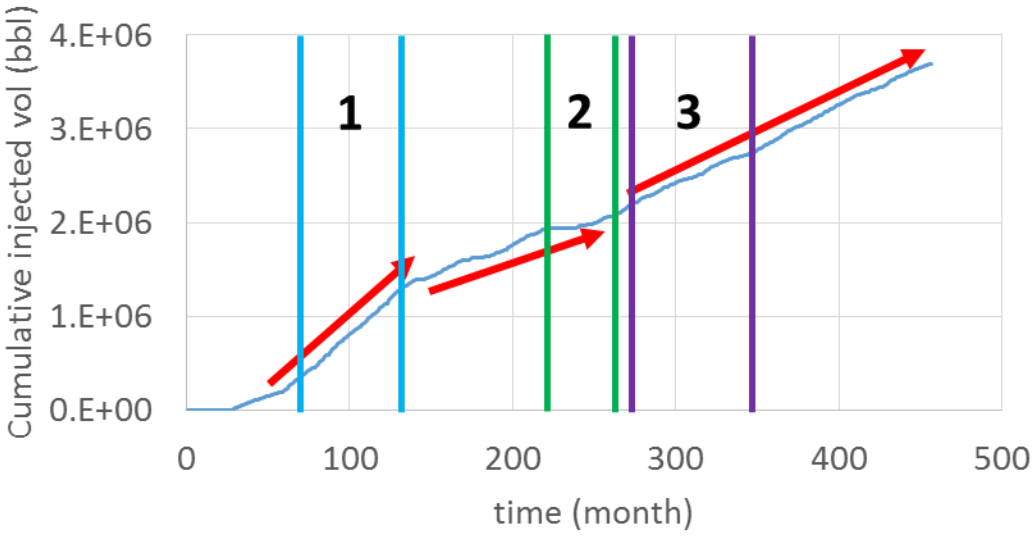

Figure 5.16 Cumulative injected volume with respect to time for injection well I40 (the numbers 1, 2 and 3 show the corresponding periods).

5.2.2 Window 2

5.2.2.1 Optimum window size for the CM-PW application

Similar to the procedure for Window 1, we estimate the most significant component of the I62 spectrum as 0.02 cycle per month (**Figure 5.17**). The median frequency in the area is 0.075 cycle per month. After the simulation, similar to what we did for Window 1, we plot λ vs IWD and the interwell distance with $\lambda_{cut\ off}$ = 0.1 equals to 3600 ft. (**Figure 5.18**). On the areal R_{ε} (f = 0.075 cycle/month) plot, IWD = 3600 corresponds to $R_{\varepsilon\ crit.}$ = 0.0001297 (**Figure 5.19**). Using the I62 R_{ε} plot and $R_{\varepsilon\ crit}$, we find that I62 radius of influence equals to 3774 (**Figure 5.20**). As expected, its radius of influence is greater than IWD at $\lambda_{cut\ off}$, because the I62 major frequency component is less than the median frequency.

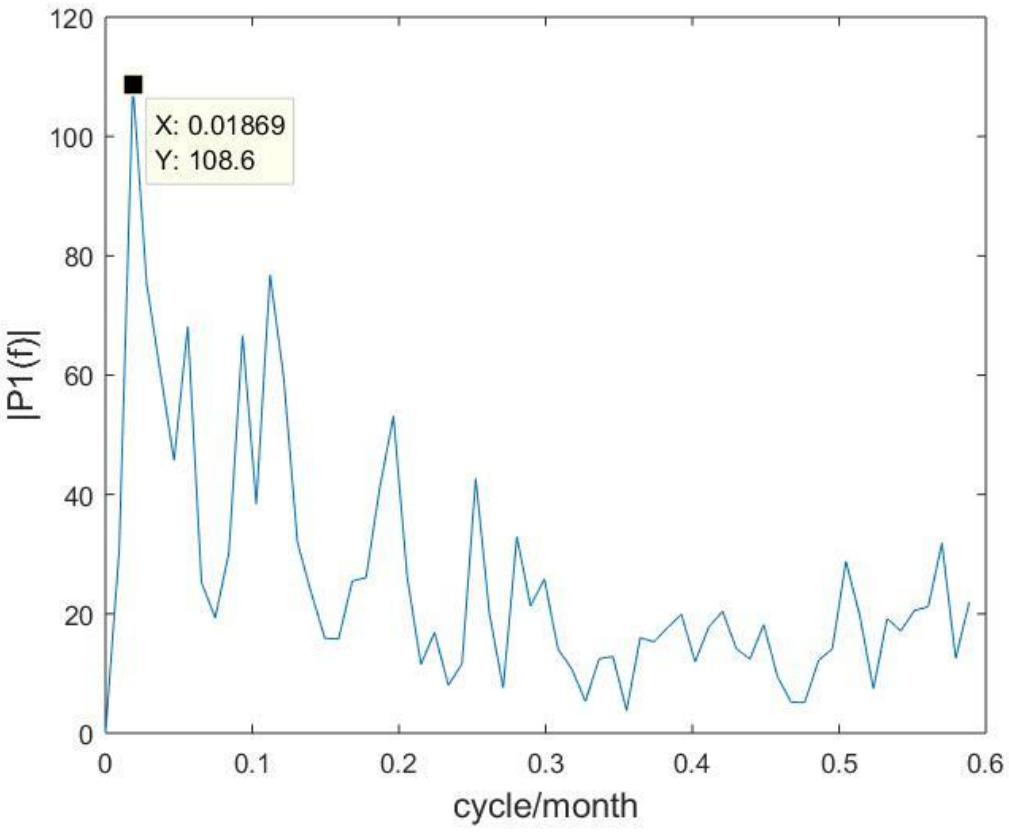

Figure 5.17 I62 FFT Periodogram showing the most significant low-frequency peak and its corresponding frequency value

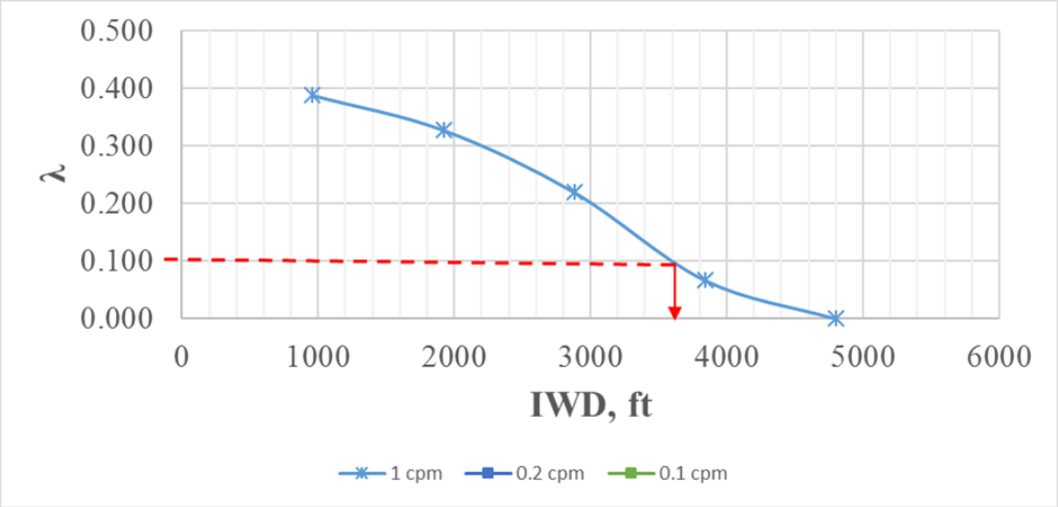

Figure 5.18 Corresponding IWD at λcut off = 0.1

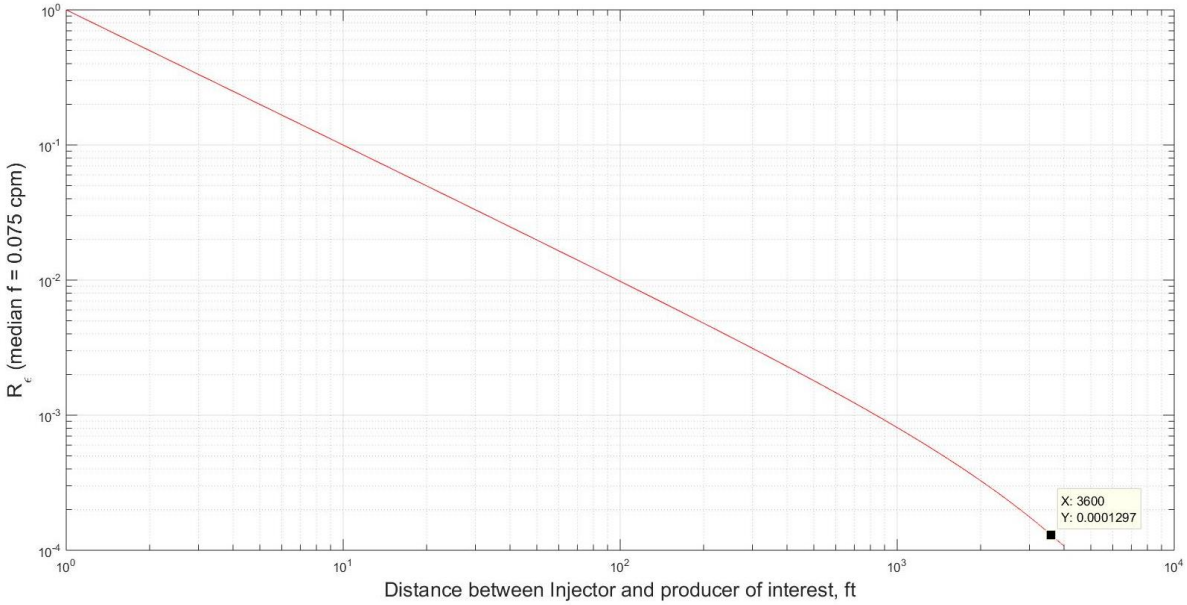

Figure 5.19 Area R_ε plot. The critical R_ε at IWD = 3600 ft

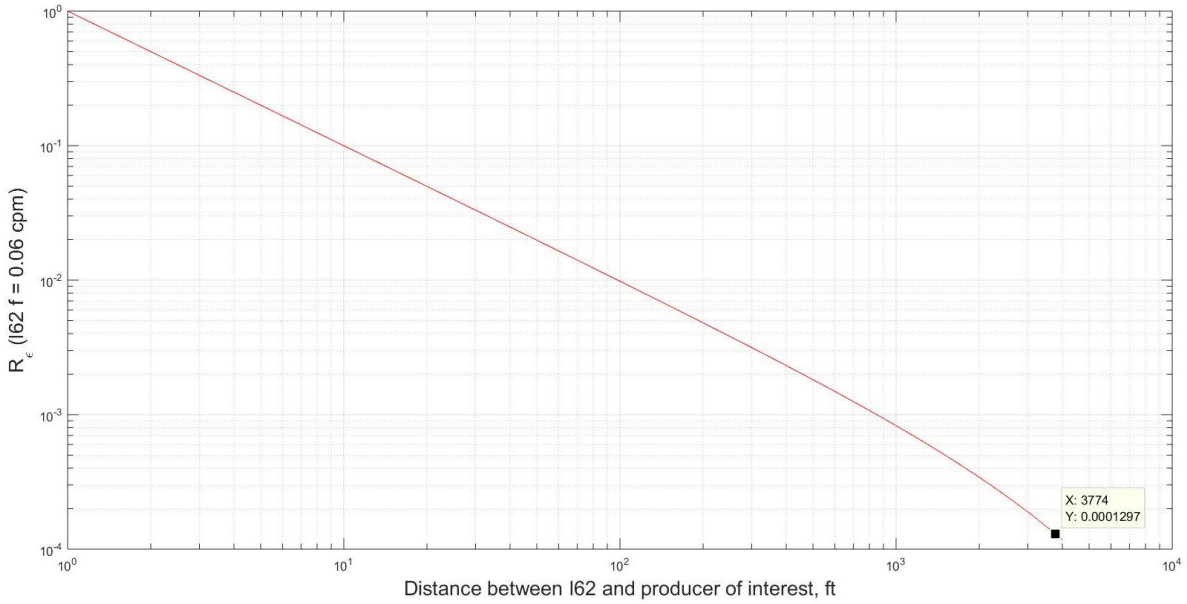

Figure 5.20 I62 Rε plot. For the critical Rε = 0.0001297, IWD = 3774 ft

The IWD of 3774 ft exceeds the 160-acre well spacing. All of the wells in this window area therefore fall within the I62 radius of influence. We choose offset producers around I62 and expect that model accuracy will be good.

5.2.2.2 CM-PW Analysis

In this window area (**Figure 5.21**), there are four producers and one injector. We selected three periods (**Figure 5.22**) to study the effects of well treatments and the presence of conglomerate on interwell connectivity We obtain a very good match between the CM-PW predicted and measured rates for all three periods with $L \geq 3.4$ (**Table 5.5**). We also observe that R^2 increases with increasing L, which is consistent with Kaviani et al.'s (2014) findings.

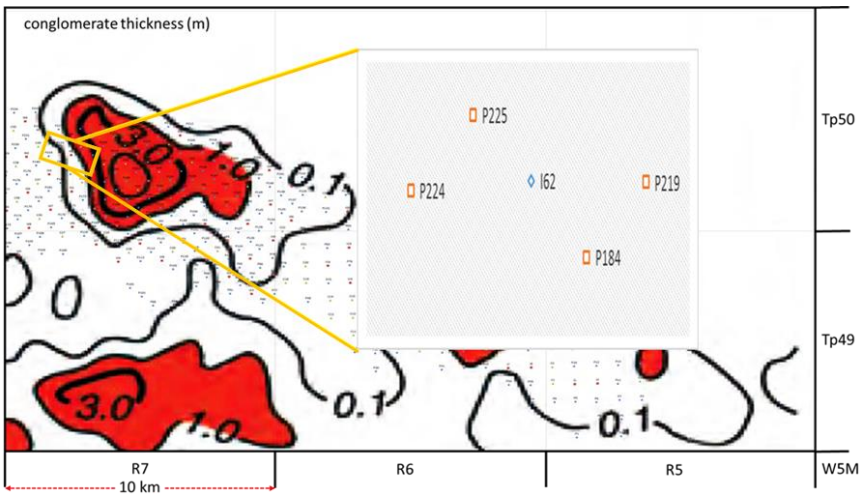

Figure 5.21 Window 2 location and its proximity to significant conglomerate thicknesses.

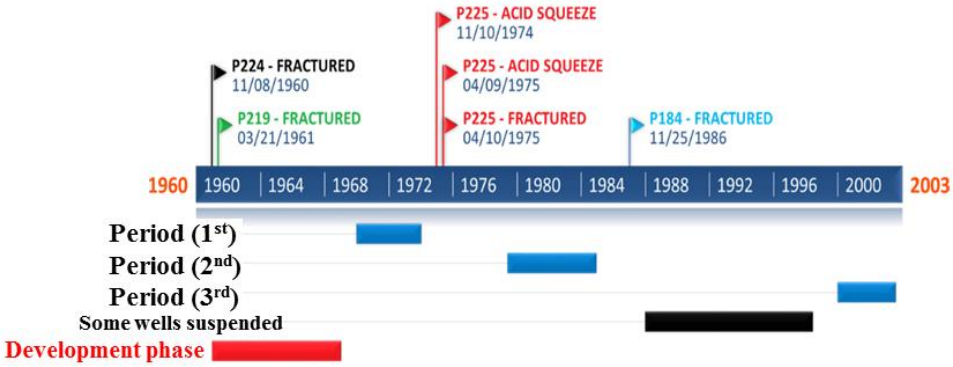

Figure 5.22 Window 2: well treatment timeline (I62 and P 219 were intermittently suspended)

Table 5.5 Window 2 – R^2 values of total predicted vs total measured production rates during each period.

Period	Start Date (dd/mm/yyyy)	End Date (dd/mm/yyyy)	R^2	L values
1st	01/07/1970	01/06/1974	0.91	4.7
2nd	01/06/1979	01/12/1984	0.95	6.6
3rd	01/02/2000	01/07/2003	0.89	3.4

The CM-PW analysis of the first period shows that the normalized connectivities between well pairs I62-P224 and I62-P219 are large (**Figure 5.23**). This result is consistent with our expectation from the FFT analysis that the I62 injection rate fluctuation frequency is sufficiently low to strongly affect producer wells at the distances of P224 and P219. This issue will be discussed further below.

Since the pseudo well connectivity (**Figure 5.23**) is directed towards the conglomerate bearing zone in the east, we infer that the conglomerate contributes to the connectivities in this window. Core data from the unfractured wells P225 and P184 also suggest the presence of conglomerate in the east, since the flow capacity (permeability-thickness product, kh) of P184 is 2½ times that of well P225 and there appears to be a clear relation between λ′ and kh for these wells (**Figure 5.24**).

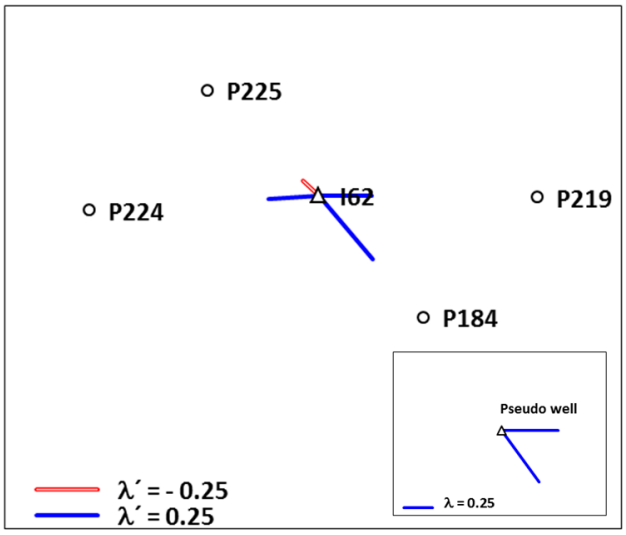

Figure 5.23 Window 2 – 1st Period –connectivity map where P224 and P219 are fractured (the plot in the lower right corner shows pseudo well connectivity).

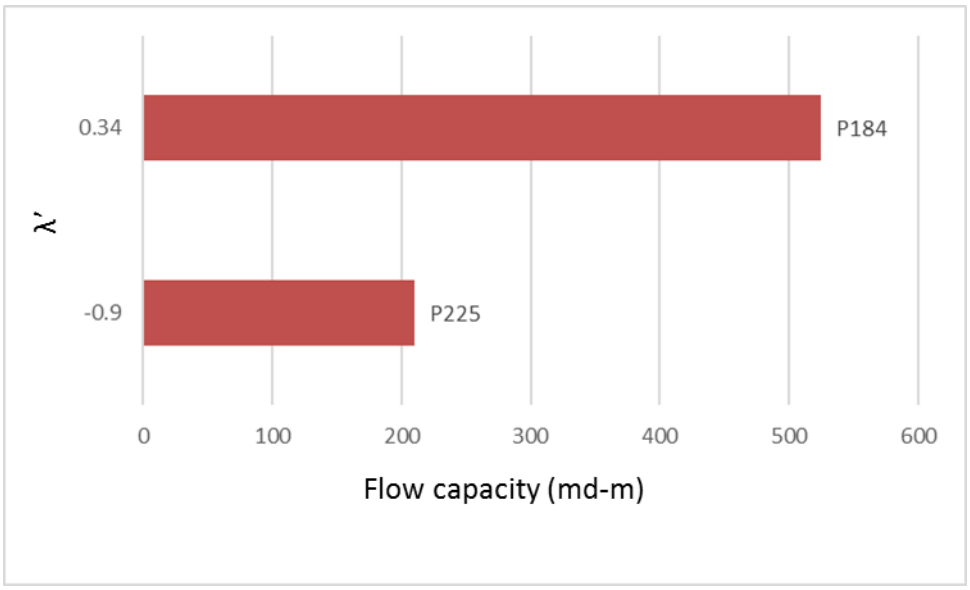

Figure 5.24 λ' vs $k_{max}h$ for the initially unfractured wells P184 and P225; the connectivities are consistent with the well flow capacities.

P225 is the only well having λ' < 0 and the operator may have recognized that this well was receiving little support from I62 because P225 was acid squeezed twice and fractured with 8.5 tons of 10/20 sand after the first period (AER reports). CM-PW analysis in the second period (**Figure 5.25**) indicates the connectivity of P225 increased by 0.16 (i.e., $\Delta\lambda' = \lambda'_{period2} - \lambda'_{period1} = 0.16$), and the connectivity of I62 with other producers either decreased (I62 – P184) or remained the same (I62 – P224). The pseudo well still exhibits the strongest support directed to the east (**Figure 5.26**).

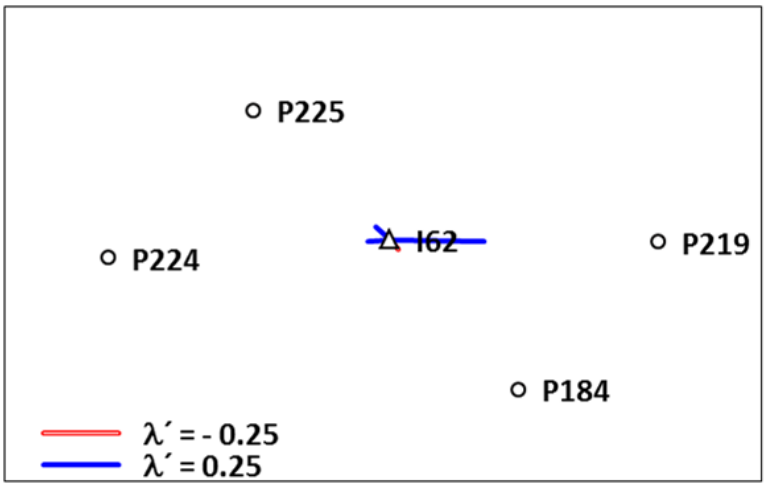

Figure 5.25 Window 2 – the connectivity map after acid squeezing and fracturing P225 (2nd Period)

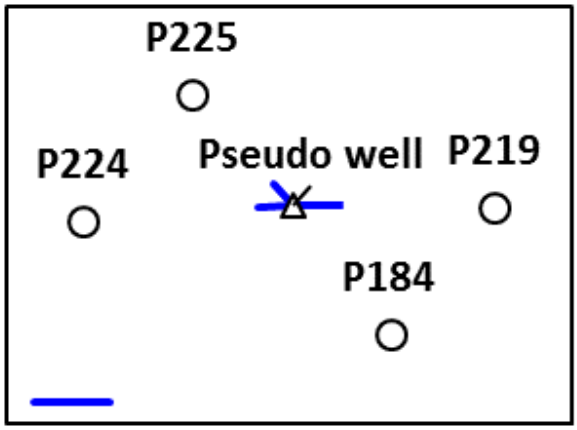

Figure 5.26 Pseudo well connectivity during the 2nd Period shows largest connectivity with P219 the east.

A plot of $\Delta\lambda'$ vs proppant tonnage for the treatments of wells P225 and P184 shows a direct proportion (**Figure 5.27**), where we have added the point at the origin on the basis that zero proppant should leave the connectivity unchanged.

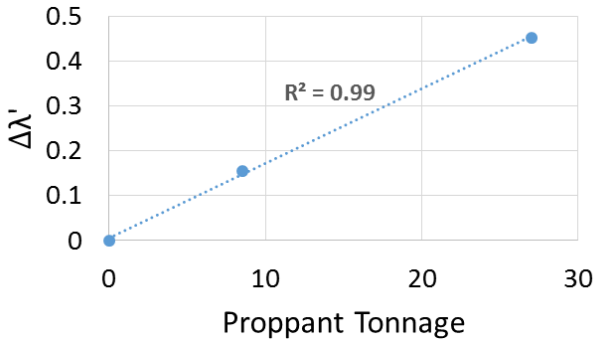

Figure 5.27 Change in connectivity, Δλ′, vs proppant tonnage suggests a linear relationship, where the point at the origin is added from physical reasoning.

After all the treatments, the I62 – P184 connectivity was strong during the 3rd period (**Figure 5.28**). The pseudo well also shows a strong connection with P225 and P184 (**Figure 5.29**). P225 connectivity has improved after the suspension of some wells outside the areal window. It may be that refracturing P184 reactivated the connection with both the injector and the conglomerate bearing region. Fracturing the wells close to the thick conglomerate zone increases the connection with that zone; therefore, fracturing those wells close to the conglomerate region may be considered a successful operation to extract oil from that zone.

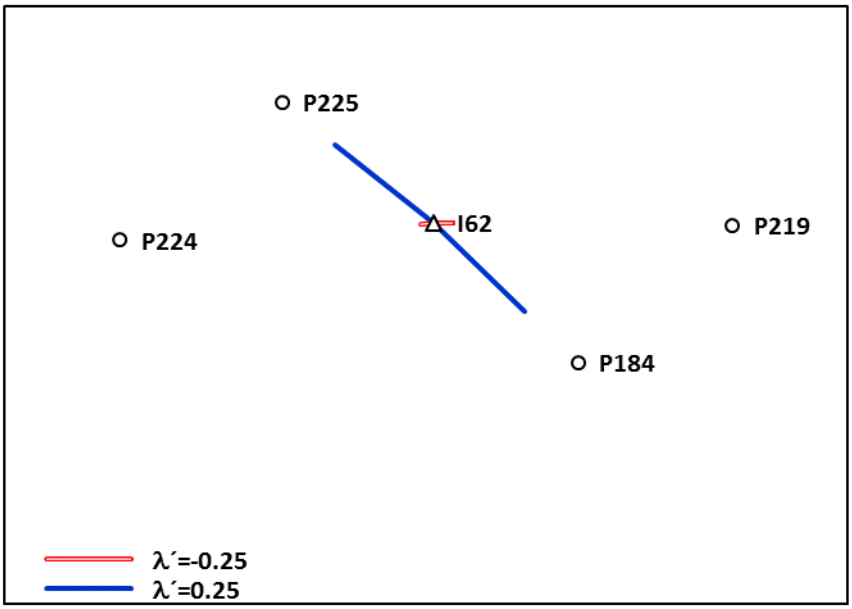

Figure 5.28 Window 2: Connectivity map during the 3rd Period

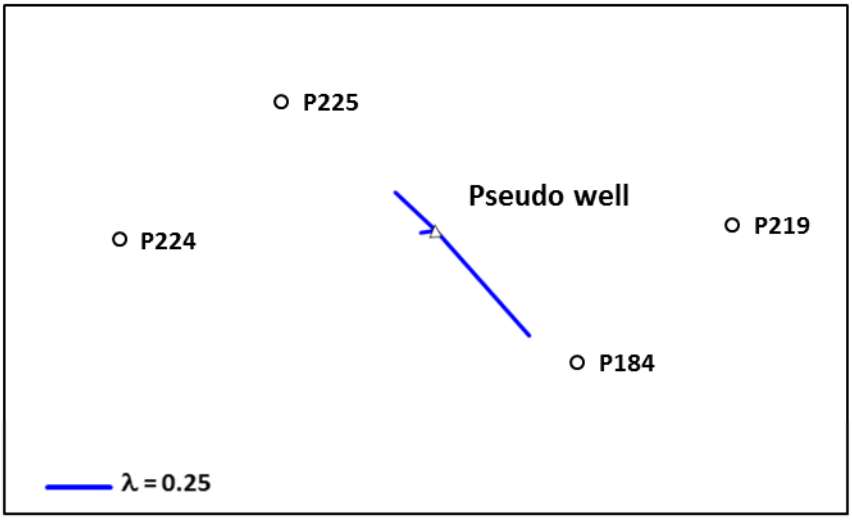

Figure 5.29 Pseudo well connectivity during the 3rd Period

5.3 Discussion

Previous Cardium Formation studies indicate that it is very heterogeneous vertically. For a few lithofacies, lateral continuity in the East Pembina Oil Field has been studied. Butrenchuk et al. (1995) report that high lateral continuity in sandstones and shales would be likely to occur if the depositional model of a NW-SE prograding shoreline stepping out into the basin were the case. P184's strong connection with I62 in Window 2 suggests that there exists a significant hydraulic continuity between this well pair having an interwell distance of 1916 ft. This distance is larger than Krause et al.'s (1987) assumption that the lithofacies extend halfway between wells. It appears that the conglomerate is an important element in the connectivity of wells, even where only some of the wells show conglomerate. During the first period of the Window 2 analysis, the pseudo well connectivity map showed that there is strong support from the thick conglomerate-bearing region. As for Window 1, we could not infer anything about lateral continuity because the wells were fractured before any of the CM-PW analyses.

All of the wells inside the windows were within the determined window size for the central injectors. The CM-PW analyses revealed that wells within the injectors' radius of influence can

have $\lambda' > 0$. Some positive λ's were close to $\lambda_{cut\ off}$, although those wells are offset to the injectors. We observed connectivity of those wells changed as analysis periods are chosen between the well events. The average field permeability is used for the R_ε calculation, It might be more representative to use injectors' core data instead of the average field permeability. In these window areas, the injectors were not cored. Hence, we used field permeability for the simulations.

The field case applications showed that having a pseudo-well in the model helps to identify the contribution of a high permeability layer (the conglomerate) to the wells in contact with that layer. Similar to Krause et al. (1987), we also determined that an area with a significant conglomerate layer (> 1 m thick) contributes to IWC and thereby to total production. There are some wells in the eastern parts of the East Pembina Oil Field which are located in the thin conglomerate-bearing regions, and these wells might still benefit because of proximity to the thicker portions. It is possible the fractures of these wells might penetrate to the thicker parts of the conglomerate layer. Having microseismic images of these wells would help us to characterize these phenomena.

By analyzing the connectivities after well treatments, insights into the stimulation effects can be seen. In Window 1, the CM-PW identified the wells in need of treatment during all the periods. We determined that well connectivity increased with the amount of proppant used. It remains unclear how the field operator identified the wells to treat; we could not locate reports evaluating whether the stimulations were considered successful. We also could not find any study covering how hydraulic fracture networks change shape with time in the Cardium pool. Window 1 seems to be more stress sensitive than the Window 2 since re-fracturing could not improve the P145 connectivity. Well P127, initially fractured with a larger amount of proppant, kept benefiting from injection outside of the chosen area during all the periods. The first period results were in agreement with the S_{Hmax} in the region. We have some questions left unanswered, as most of these wells lack detailed reports.

The analyses suggest that fracturing all the wells or re-fracturing might not be the best solution to preserve existing connections with surrounding wells. For instance,

1) Fracturing a well located in a high permeability zone might establish a connection with a possible water-bearing zone, which causes a very high watercut in the early period of that well. P128 from the Window 1 was one of those wells.

2) Re-fracturing can reopen a closed fracture, which might re-establish a connection with an injector through an already swept zone and reduce or lose connection with a current contributor.
3) Re-fracturing can starve other producers of injection support, as we saw in Window 1.

As the reservoir is waterflooded, fracture shear failure might occur and which directly affects the connectivity of a fractured well (Palmer et al., 2007). For example, after the first period, P145 did not communicate with the injectors I40 and I37 aligned along the direction of S_{Hmax}. Injection induced fractures can also affect the IWC, which could cause needless remedial work on nearby producers. Therefore, determination of threshold injection rates to avoid fracturing a formation might avoid such causes. It seems I40 had injection-created fractures during the first period since the cumulative injected volume plot shows the largest slope and I40 had the positive normalized connectivity with both P127 and P145 and aligning with the S_{Hmax}.

Using heat analogy and simulation methods gave us approximate window size. Estimated window sizes of two areal windows revealed that surrounding producers are within the injectors radius of influence. It suggests that using heat analogy and simulation methods is consistent with spatial window sizing.

5.4 Conclusions

The analysis of the two study areas using the CM-PW gives promising results and insights:

- Early time IWC of fractured wells was consistent with the regional stress
- Refracturing does not always offer improvement; it can impair IWC for some situations
- Injection induced fractures can contribute significantly to the IWC
- The type of heterogeneity controlling the IWC in a system may depend on the nature of the stimulations and their interactions with depositional heterogeneities. For the Cardium, conglomerates enhanced connectivities with nearby injectors.

The field study results suggest that well treatments ought to be carefully designed in order to avoid unintended reductions of IWC.

The CM-PW analysis showed there exists significant hydraulic communication between the well pairs having interwell distances of approximately 2000 ft. i.e. 80-acre well spacing. This

effect was also observed using the heat-conduction analogy and the FFT of the injection rate spectrum (described in Chapter 4). Combining the spectral analysis with the emittance ratio, we were able to predict window size for the model application. In both windows, we found that the injector radius of influence is greater than the interwell distance between the central injector and the surrounding producer wells. In Window 2, the IWD at $\lambda_{cut\ off}$ is within 5% change of IWD from the R_{ε} plot. Wells located beyond the radius of influence are likely to be less affected by the injector of interest.

CHAPTER 6 INTERWELL CONNECTIVITY SURFACE PLOTS

In this chapter, we generate and analyze IWC surface plots for a wide range of permeabilities for a two-injector, one producer model. We also tested a single-barrier case to evaluate the effect of heterogeneity on IWC and heterogeneity-ratio. The effect of diffusivity on IWC is significant. There are specific ranges of diffusivity in which IWC has a different behavior. As expected, increasing injection well frequency decreases contribution percent from that well. There are discrepancies, however, to this observation when the diffusivity gets very low. The τs are insensitive to injection signal frequency and amplitude, but increasing diffusivity causes decrease in them in general. Heterogeneity-ratios revealed the interwell heterogeneity for a wide range of diffusivity.

6.1 Model and Parameters to be Tested

A model (**Table 6.1**) comprises 2 injectors (I01, I02) and a producer (P01) (**Figure 6.1**). We used sinusoidal injection signals for injection rates (Eq. 6 – 1). To have positive injection rates, we added a constant shift to the signal. The coefficient A represents the amplitude of the signal. **Figure 6.2** shows a sample sinusoidal signal with an amplitude of 200 rb/day and frequency of 1 cpm (cycle per month). The list of parameters from Eq. 6 – 1 to be tested are:

- Injection signal amplitude, A
- Frequency of injection signal, f

Table 6.1 Reservoir and fluid data used for the homogeneous 1x2 model.

Parameter	Value
Porosity, ϕ, fraction	0.1
Horizontal k, md	1.0
Total compressibility, c_t, psi^{-1}	1×10^{-6}
Fluid viscosity, μ, cp	0.5
Reservoir size in x-direction, ft	3240
Reservoir size in y-direction, ft	3240
Formation thickness, ft	20
Reservoir depth, ft	3000
Reservoir pressure, psi	1470
N_x	81
N_y	81
N_z	1

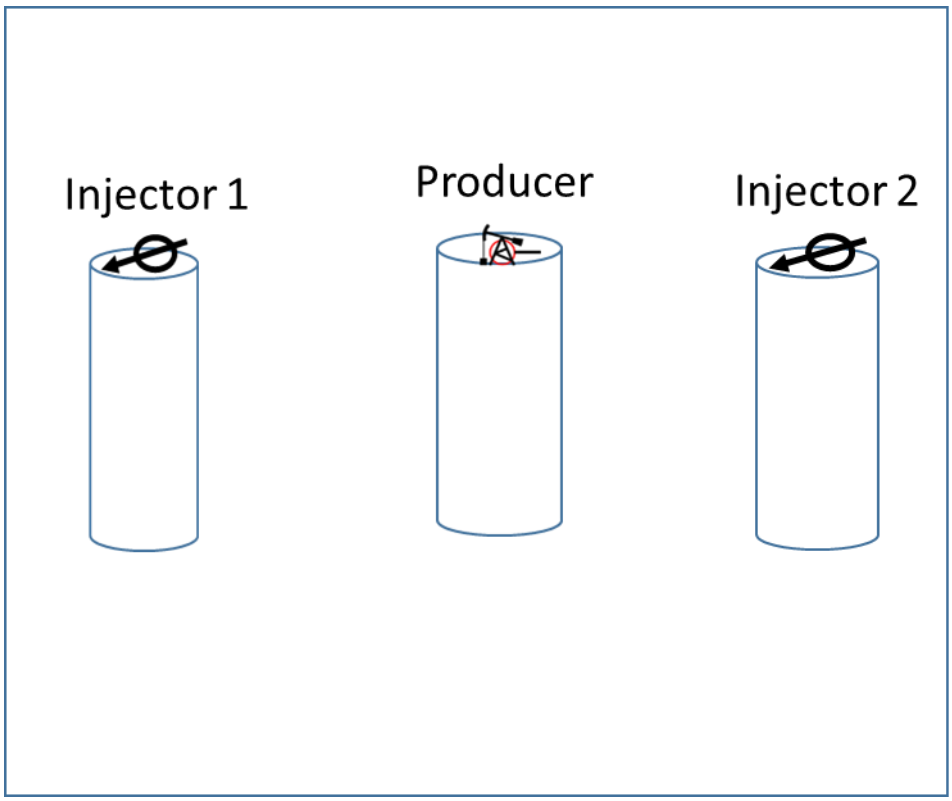

Figure 6.1 2x1 model - Producer surrounded by two injectors

$$Injection\ rate = Constant\ shift + A * \sin(2\pi f * t + \theta) \quad (6-1)$$

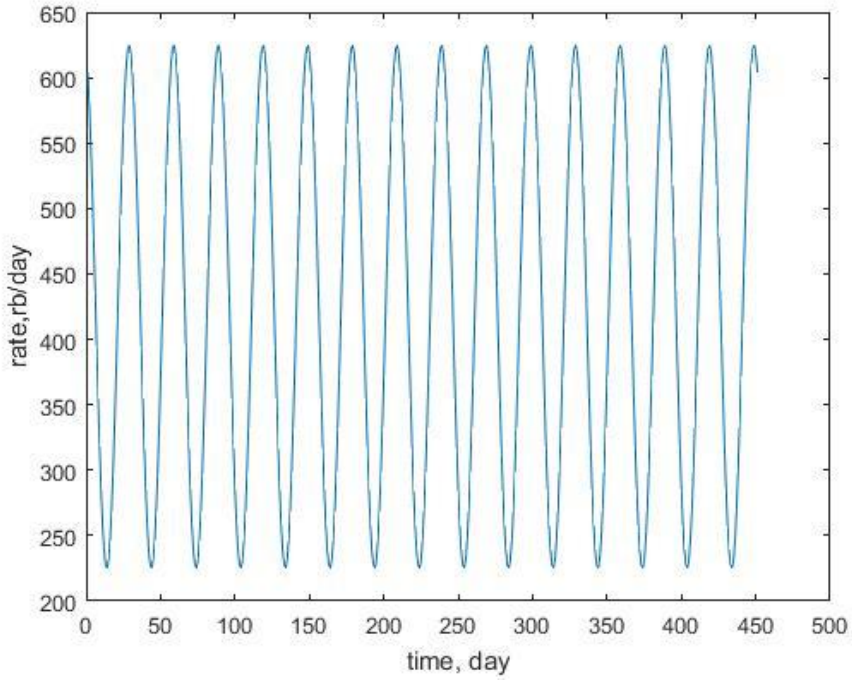

Figure 6.2. Sample sinusoidal injection rate with amplitude A = 200 rb/day and f = 1 cycle per month

6.2 Automation of Model: Model linking CMG and CM-PW

We prepared a Matlab script, which links models and provides input for the CM-PW automatically. **Figure 6.3** shows the workflow of the Matlab script. We converted the CM-PW to a Matlab function, which simply works as an input-output function in the automated model. The model asks injection signal parameters to be analyzed, and gives λ and τ values. The model automation helps us run hundreds of simulation cases. Once we plot the results, we can analyze how the CM-PW connectivity parameters change while permeability and other injection signal characteristics vary.

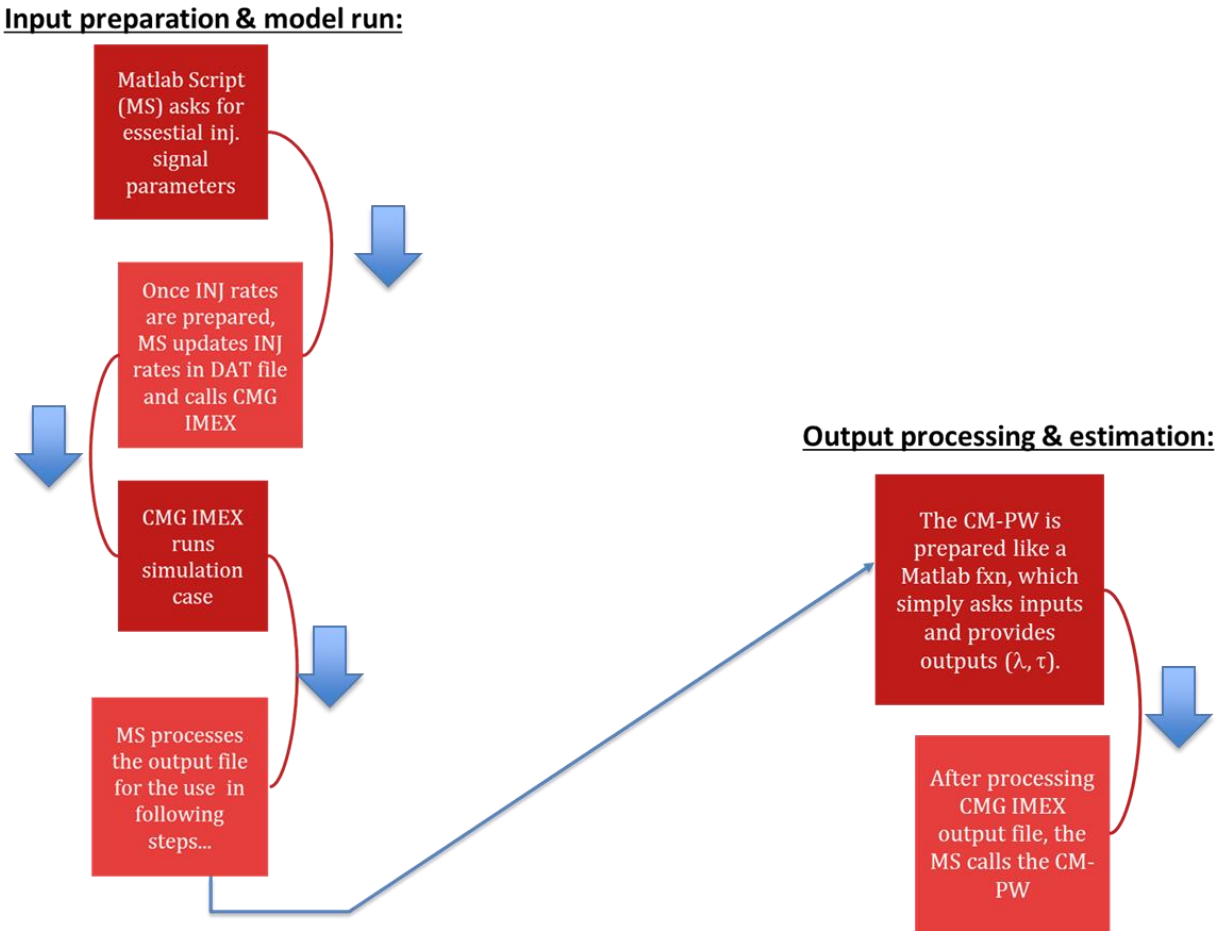

Figure 6.3 The workflow of the Matlab script.

6.3 Analysis of IWC Surface Plots

To observe how λ, τ, and the heterogeneity-ratio behave as key injection signal parameters change, we created surface plots depicting the changes. From the emittance ratio (Eq. 4-4), we are aware of which parameters might directly affect λ. Hence, we define λ as a function of following predetermined terms to be investigated:

$$\lambda = f(\dots, \boldsymbol{f}, \boldsymbol{D})$$

- **f**: Injection signal frequency
- **D**: diffusivity term $(= \frac{k}{\varphi \mu C_t})$

To evaluate the effect of heterogeneity, we also tested some cases for a semi-heterogeneous scenario (**Figure 6.4**) with similar reservoir and fluid data employed in **Table 6.1**. First, we started testing the bold variables **D** and **f**. As expected, we found that these parameters are effective on λ. The Injectors 1 and 2 with a constant f_1=1 cpm and $f_2 \geq$2 cpm represents λ_1 (low f) and λ_2 (high f), respectively. For **D** = 1.0E+08 md*psi/ cp, 10*(λ_1/ λ_2) has a slightly increasing trend, as the frequency of I02 increases from 2 cpm up to 12 cpm. Generally, the ratio λ_1/ λ_2 is ≥1 for all the diffusivities (**Figure 6.5**: A-B), with the exception of **D** = 2.0E+06 md*psi/ cp. The whole surface has a hump shape in this case. We observe that the ratio increases between the diffusivity range of 2.0E+06 and 1.0E+07 md/ (cp*1/psi). There is a decreasing trend in ratio when the diffusivity increases from 1.0E+07 to 8.0E+07 md/ (cp*1/psi). For diffusivities greater than 8.0E+7 md*psi/ cp, the ratio reaches a plateau in the range of 1 and 1.25. Keeping I01 frequency at 1 cpm gives us λ_1 = 1 for the rest of diffusivities, except **D** = 2.0E+06 md*psi/ cp (**Table 6.2**). When **D** = 2.0E+06 md*psi/ cp, due to low permeability (k= 0.1 md), λ_1 decreases from 0.72 to 0.51 (**Figure 6.6**). In case of a model with low permeability, λ_2 increases from 0.66 to 0.87 with increasing I02 frequency, which is opposite of the high diffusivity cases. It is not likely increasing I02 frequency causes λ_2 to increase in low permeability cases. Actually, decreasing λ_2 with increasing I02 frequency is not in agreement with the Emittance ratio versus frequency plot. As injection well frequency increases, emittance ratio decreases (**Figure 6.7**). This contradiction might happen when the CM-PW is not converging to the correct solution. It is possible the model lands on local minima during the optimization process. Another cause can be due to noise in the simulator data.

As in the R_ε ratio [R_ε (low f)/ R_ε (high f)] plots (**Figure 4.8**), we also observe similar trend where λ_1/ λ_2 decreases within the diffusivity range of 1.00E+07 and 8.00E+07 md*psi/cp (**Figure 6.5 (-B-)**). We observe the model was able to detect major trends in certain diffusivity ranges. We note deviations start when we deal with very low perm (low D) models, which still remains challenging due to mimicking fluid flow in very low permeability simulation models introducing noise to data. Kaviani et al. (2014) reported for L=32 λs are inconsistent for k < 1 md with noise range of 5% (low noise) and 40% (large noise level). For k = 0.1 md and L = 32, with 5% noise, median C_v of λ is above 0.4 (Kaviani et al., 2014).

Table 6.2 λ_{1S} as I02 frequency changes for various diffusivities

D, md*psi/cp	I02 Frequency, cycle per month											
	2	**3**	**4**	**5**	**6**	**7**	**8**	**9**	**10**	**11**	**11.5**	**12**
2.0E+06	0.72	0.63	0.57	0.55	0.54	0.53	0.53	0.52	0.51	0.51	0.51	0.51
1.0E+07	1	1	1	1	1	1	1	1	1	1	1	1
1.8E+07	1	1	1	1	1	1	1	1	1	1	1	1
8.0E+07	1	1	1	1	1	1	1	1	1	1	1	1
1.0E+08	1	1	1	1	1	1	1	1	1	1	1	1
2.0E+08	1	1	1	1	1	1	1	1	1	1	1	1
2.0E+09	1	1	1	1	1	1	1	1	1	1	1	1

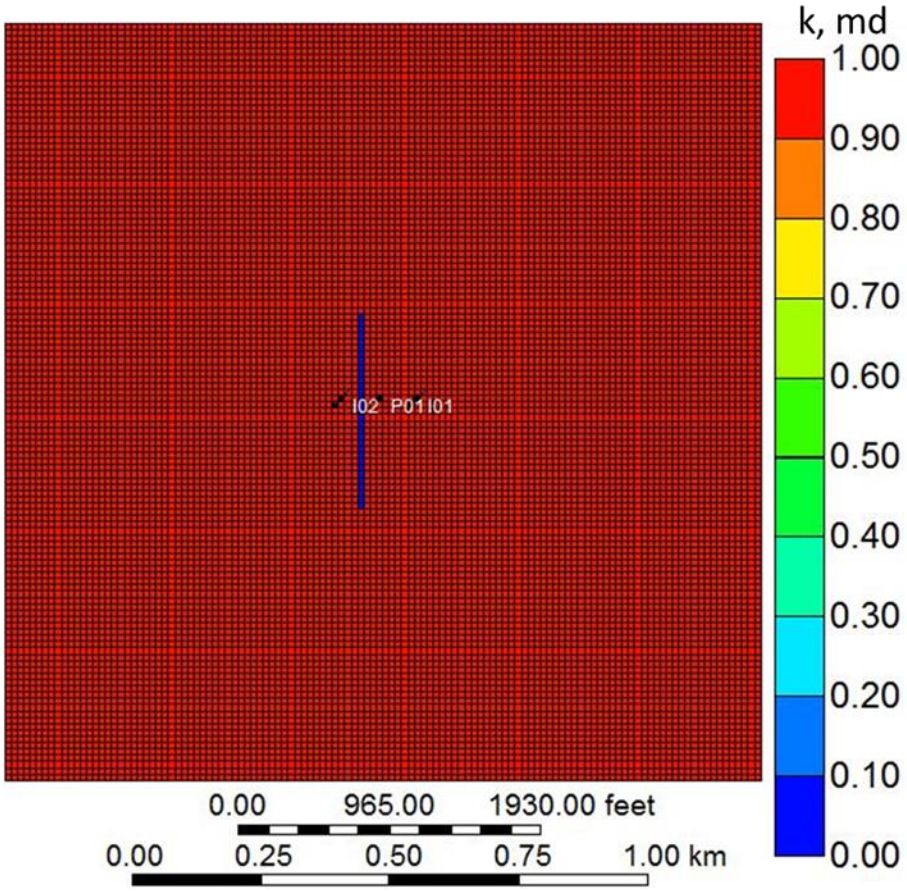

Figure 6.4 2x1 semi-heterogeneous model having a barrier between I02 and P01

(-A-)

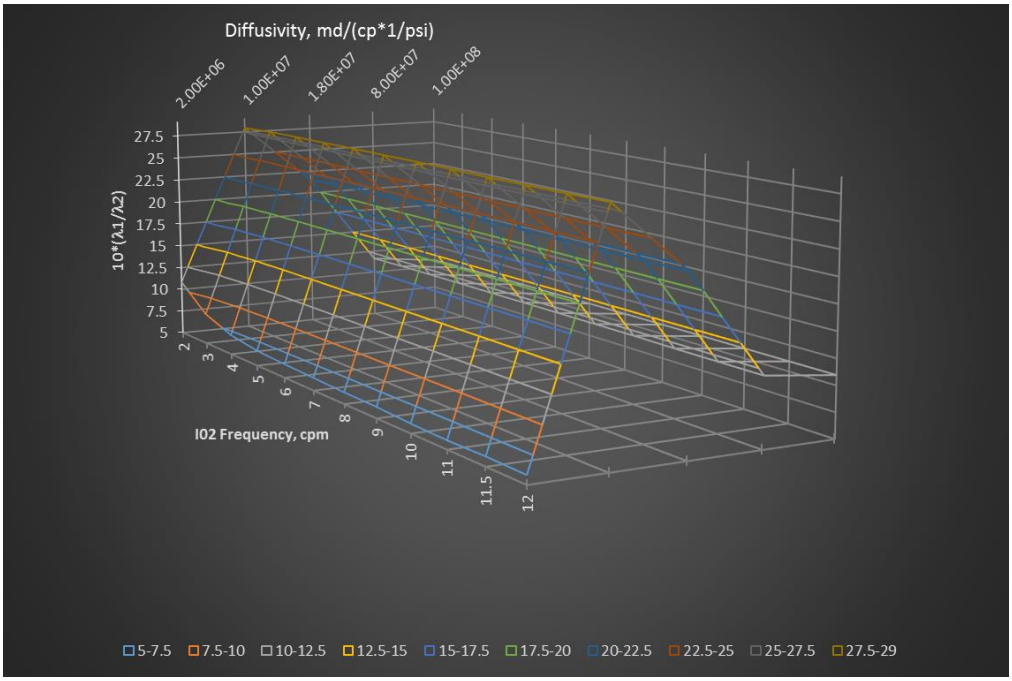

(-B-)

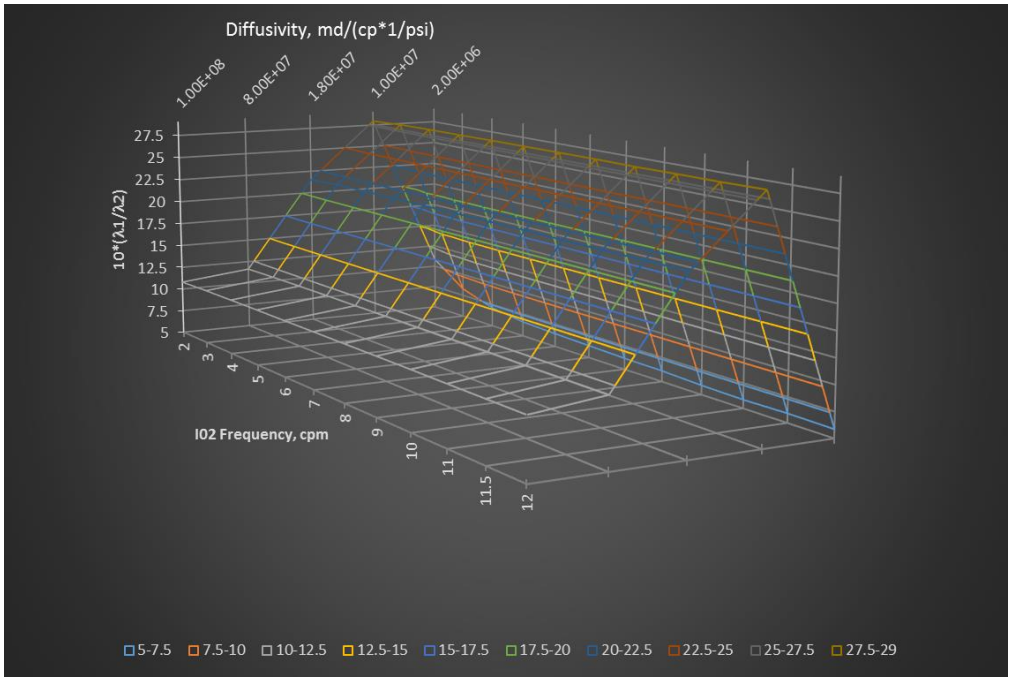

Figure 6.5 (-A-): Surface plot of $10*(\lambda_1/\lambda_2)$ when I02 frequency and diffusivity change. We multiplied the ratio by 10 to magnify the values. (-B-): same surface plot as in (-A-) with diffusivity in reverse order to show backside of the surface plot.

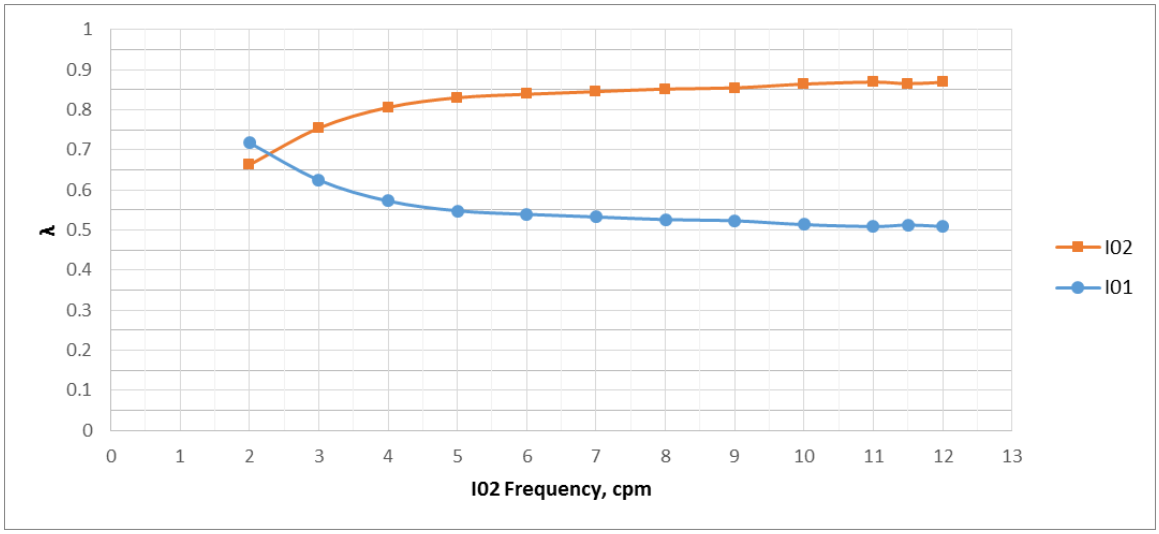

Figure 6.6 λ_1, λ_2 plots as I02 frequency changes, when D = 2.0E+06 md*psi/ cp

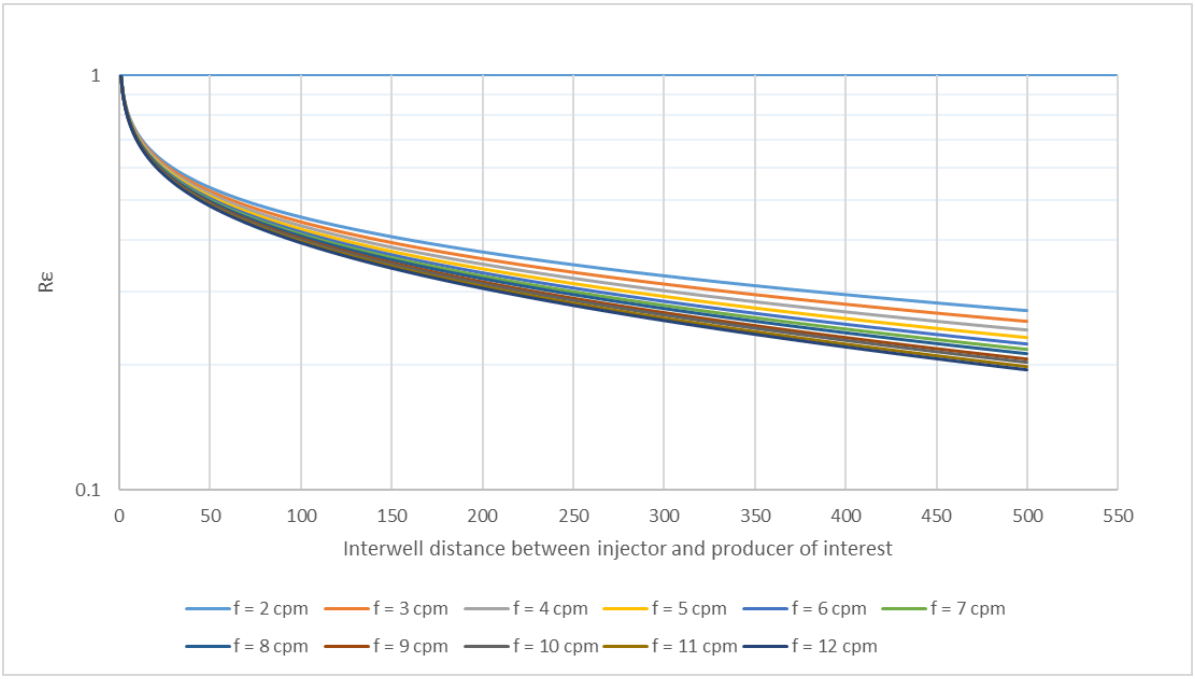

Figure 6.7 For D = 2.0E+06 md*psi/ cp, Emittance ratio plots for frequency range of 2 and 12 cpm

We did not observe any significant effect of I02 frequency on Producer τ surface plot (**Figure 6.8**). For low diffusivity range 2.0E+06 and 1.8E+07 md*psi/ cp, τ values increase as diffusivity increases. Then, τs decrease down to 30 days when diffusivity reaches to 2.0E+09 md*psi/ cp. There is insignificant effect of Injection signal amplitude on Producer τs (**Figure 6.9**) from the semi-heterogeneous case (**Figure 6.4**). For the diffusivity range of 8.0E+06 to 1.8E+07 md*psi/ cp, the standard deviation of Producer P01 τ varies between 1.5 and 2 days, when the injection signal amplitude in both injectors changes. In the semi-heterogeneous case, λ_1 does not change more than twice, when we change injection signal amplitude of both injectors (**Figure 6.10**). As signal amplitude changes, the λ_1 standard deviation is less than 0.1. Due to interwell region homogeneity, λ_1 shows a simple behavior as diffusivity increases; λ_1 increases with increasing diffusivity. For **D** = 2.0E+09 md*psi/ cp and amplitude of 382.5, λ_2 shows anomaly when compared to values at different amplitudes (**Figure 6.11**).

The effects of diffusivity on the λs are clear. λ Surface plots reveal that connectivity is quite sensitive to diffusivity. We observe λ_2 varies when diffusivity increases. When **D** = 2.0E+06 md*psi/ cp, $\lambda_2 = 1$. When we look at the heterogeneity-ratio surface plot, we observe that λ_1/λ_2 is generally in the range of 1 – 2 (**Figure 6.12**). The model fails to estimate rational values for low diffusivities. Given that none of the wells in our model is stimulated, this is not common in the low permeability case studies. Since this algorithm is prepared to evaluate the effect of selected parameters on λs, the values are automatically changed solely in the simulation model. In field application, we usually stimulate wells in low permeability formations to enhance near well region, which is to make wells as productive as possible. In very low permeability cases, not modifying near well region might cause deviations from the correct solution.

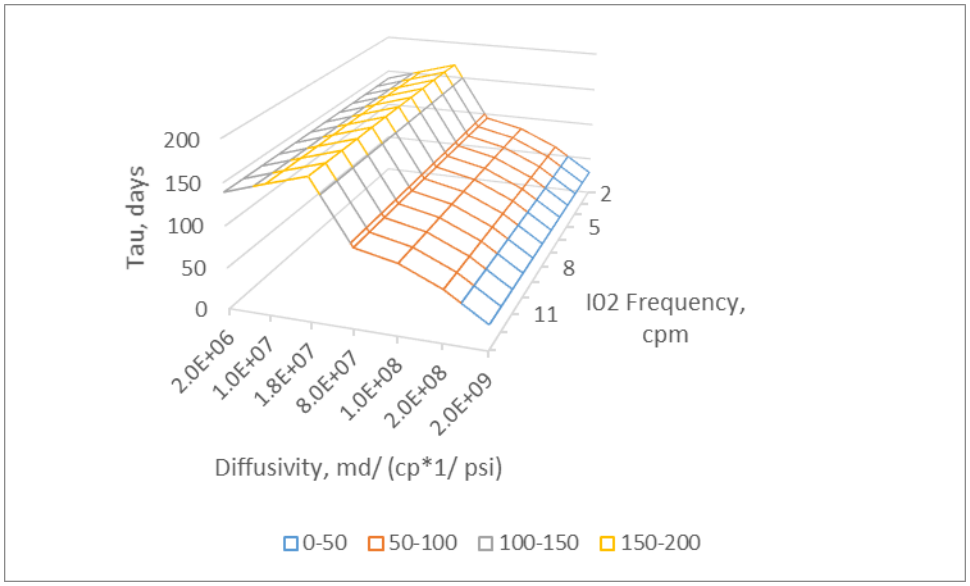

Figure 6.8 Producer P01 tau surface plot as I02 frequency and Simulation model diffusivity change

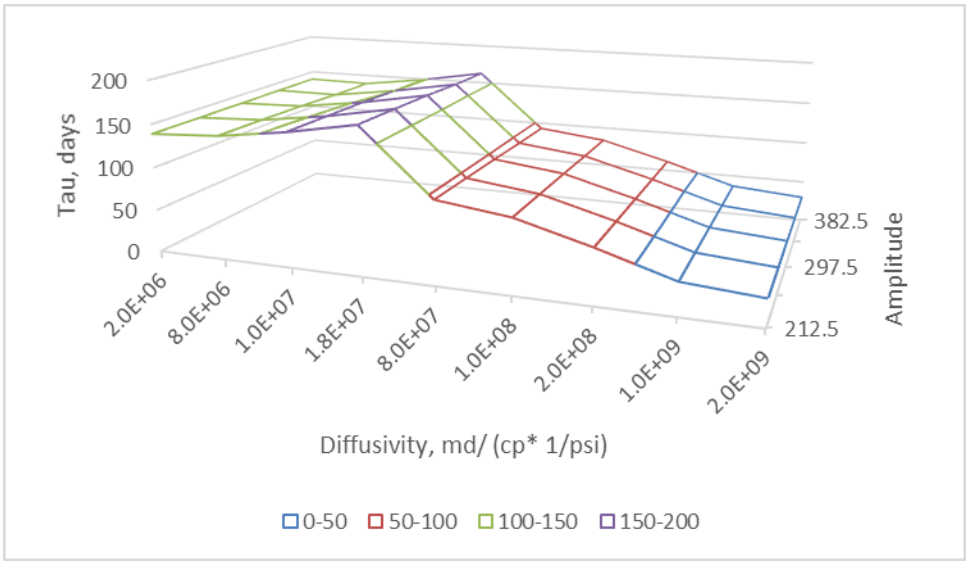

Figure 6.9 Producer P01 tau surface plot as injection signal amplitude in both injectors and Simulation model diffusivity change

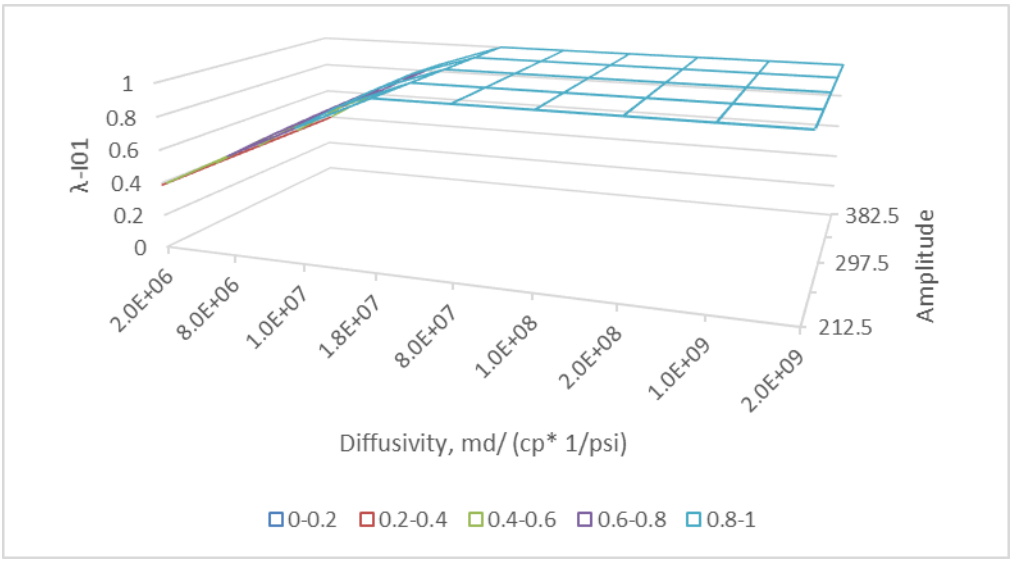

Figure 6.10 λ_1 Surface plot in case of Semi-heterogeneous scenario (Figure 6.4)

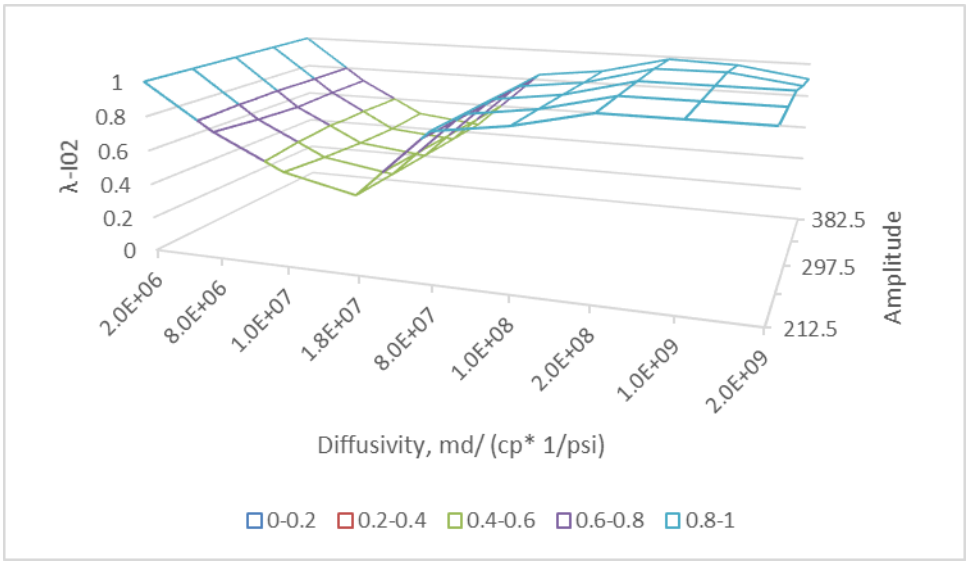

Figure 6.11 λ_2 Surface plot in case of Semi-heterogeneous scenario (Figure 6.4)

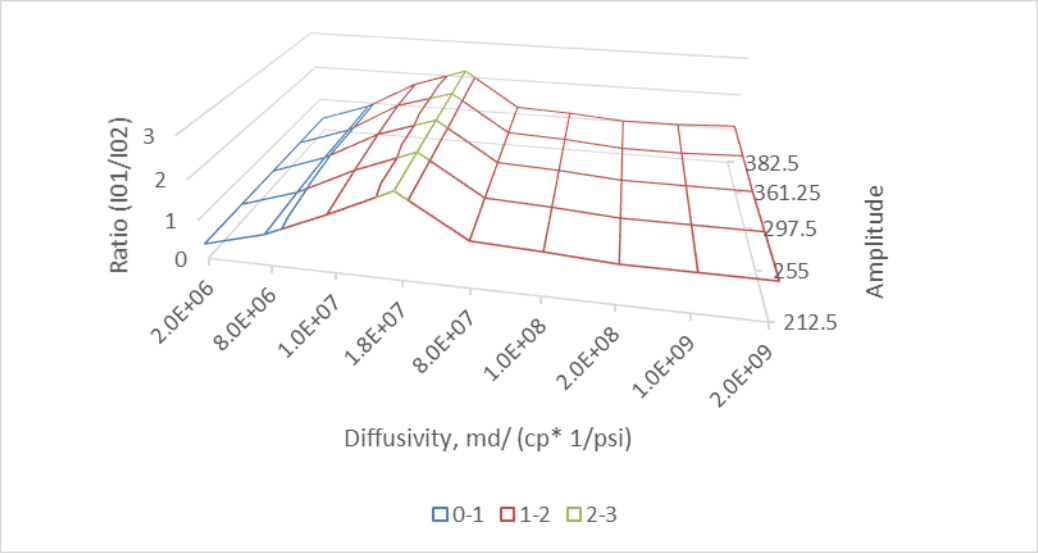

Figure 6.12 Heterogeneity-ratio Surface plot of λ in case of Semi-heterogeneous model (Figure 6.4)

6.4 Conclusions

In addition to heterogeneity, the IWC (λ) can be affected by diffusivity and injection signal frequency. This is consistent with the findings described in Chapter 4. Both [R_ε (low f)/ R_ε (high f)] and λ (low f)/ λ (high f) decrease as diffusivity increases. Signal amplitude does not affect λ, although one would expect there to be an effect if noise were added to the flow rate measurements The time constant (τ) decreases while diffusivity increases. The injection signal frequency and amplitude do not affect τ in a noise-free system. Surface plots are helpful to visually analyze the effect of key parameters on λ and τ. We note a few anomalies when the model does not converge to the correct solution. We observed deviations from the correct solution start when we deal with very low permeability simulation models.

CHAPTER 7: BAKKEN FORMATION WATERFLOOD CASE STUDY

The Bakken Formation is divided into three members: Upper Bakken Member, Middle Bakken Member and Lower Bakken Member (Borcovsky et al., 2017). Lefever et al. (1991) reported "All three members of the Bakken Formation are present in the Saskatchewan portion of the study area", which includes our study area, Viewfield Bakken oilfield.

The work in this chapter is primarily based on the journal paper entitled "Determining well-to-well connectivity using a modified capacitance model, seismic, and geology for a Bakken Waterflood[1]" but with updated and expanded results. I was first author and Riazi, N., Cronkwright, D., and others were co-authors. Dr. Riazi did the seismic interpretation. Cronkwright prepared Figures 7.1 – B, 7.3, 7.4 and 7.22 and parts of Section 7.1 text. He and Dr. Pedersen helped respond to the reviewers' concerns. Sections 7.2.1 Window size Calculation in the tracer test area did not appear in the paper.

7.1 Field Description and Geology

We use the Forget North pilot waterflood study area within the Viewfield Bakken oilfield (**Figure 7.1-A**) for the CM-PW application and integrate results with seismic and geological interpretations. The field produces from the Bakken Formation, located in the Williston Basin. The Bakken play is spread between the US (North Dakota, Montana) and Canada (Saskatchewan, Manitoba). The Viewfield Pool has an initial pressure between 1900 - 2700 psi (slightly over- to slightly under-pressured), a depth of 1490 – 1545 m, and temperature of 157 °F (CPE, 2015). It is an undersaturated oil reservoir with an oil API gravity of 44.7°. The reservoir permeability is in the 0.001 to 1 md range (Ghanizadeh et al., 2015). This is in sharp contrast to the deeper basin, where reservoirs often exceed depths of 10,000 feet and are overpressured due to localized hydrocarbon generation (Theloy and Sonnenberg, 2012).

---

[1] Mirzayev, M., Riazi, N., Cronkwright, D., Jensen, J.L., & Pedersen, P.K. (2017). Determining well-to-well connectivity using a modified capacitance model, seismic, and geology for a Bakken Waterflood, *Journal of Petroleum Science and Engineering*, 152, 711-727. doi.org/10.1016/j.petrol.2017.01.032.

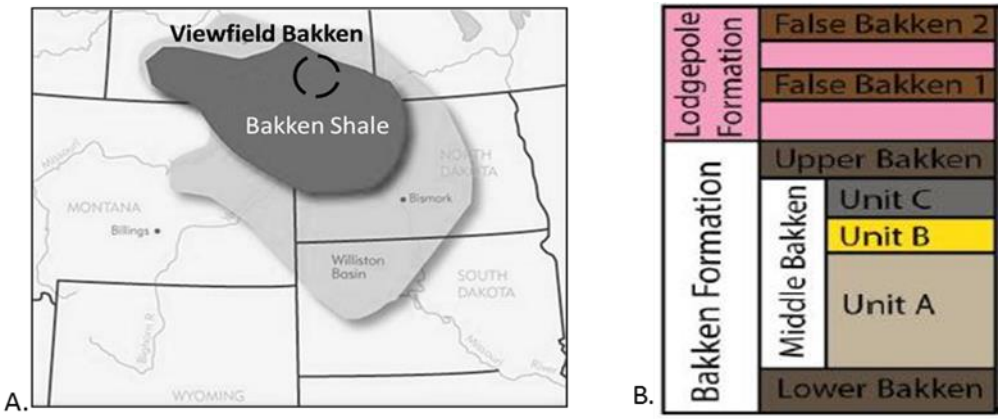

Figure 7.1 A. The Viewfield Bakken oilfield location (dashed circle) (modified from the CanadianOilStocks, 2015). B. Local stratigraphic column with well log responses, with Unit A being the main reservoir; Unit B is absent in the Forget North area (Edited from Cronkwright, 2017).

There is only one target zone and no co-mingling of production from multiple reservoirs in and around the Forget North area (**Figure 7.1-B**). Formations above and below the Bakken are considered non-pay and will have little to no contribution to hydrocarbon production, although the overlying Lodgepole Formation is a source of significant volumes of water in some wells. Fracking and injection pressures in this area are tightly controlled to try and keep propagating fractures within the Bakken Formation. Microseismic data from Kendall (2008) demonstrates a vertical offset of 40m between the upper and lowermost-recorded events in a horizontal well completed near the southern margin of the Viewfield Pool. This study also demonstrated fracture height can be controlled by varying injection rates. The less mechanically competent Upper and Lower Bakken members and the False Bakken act as a lithological barriers to vertical fracture propagation (Hassen et. al., 2012). Ferrill et. al. (2014) showed that the mud rock layers in the Eagle Ford can impede tensile fracture propagation from adjacent bedding and isolation of natural fracture networks can occur within more competent beds bounded by incompetent mudrock layers. The Bakken Formation consists of a more competent middle member, bounded by two less competent shale beds, and should behave in a similar fashion. Fisher and Warpinski (2011) suggest vertical fracture growth is hindered by sediment layers and weak interfaces, and thus horizontal fracture growth is more prevalent. The Upper and Lower Bakken, False Bakken, and the very vertically heterogeneous Unit C are expected to hinder vertical fracture growth. Simulations by Hassen

(2012) show increasing the shale thickness from 1m to 4m can reduce fracture growth out of the Upper Bakken from 25m to about 2m.

The first horizontal wells were drilled in the pilot area in 2007. Approximately 4 years later, some of the wells were converted to injectors and water flooding started. The wells used for the IWC analysis employing geological, geophysical and engineering evaluations are shown in **Figure 7.2** (IHS Accumap, 2015).

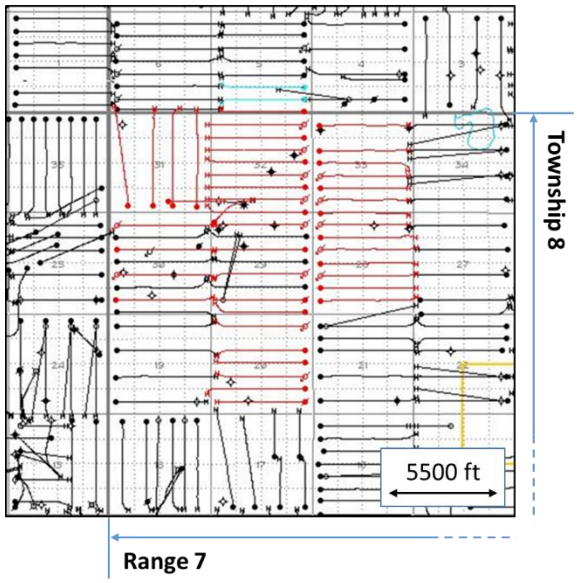

Figure 7.2 Wells from the Forget North area in Township 8, Range 7 W2M shown with red color (recently, a few infills have been added to the area and are not included in the analysis; Accumap, 2015)

Despite lithological factors and stimulation design efforts to avoid water from the Lodgepole, the fracture barrier of the upper Bakken may occasionally have both natural and stimulated fractures passing through it, explaining the high water production observed in some non-fractured horizontal wells (Cronkwright et al., 2014). Halabura et al. (2002) propose that those fractures were created by local collapse tectonics due to karstification of the underlying Duperow Formation. Also, the upper part of the middle member, Unit C, might occasionally have thin zones of high permeability that can act as thief zones between wells (Cronkwright et al., 2014).

The producing middle member of the Bakken has three distinct units, Unit A, B and C (**Figure 7.3**). Cronkwright et al. (2014) described Unit A as dolomitized, highly bioturbated

siltstone, Unit B is mainly absent in the Viewfield area but when present is a very fine to medium grained, well-cemented sandstone, and Unit C comprises interbedded siltstones and mudstones. Unit A which forms a vast portion of the reservoir is a coarsening upward unit hosting oil (Kohlruss and Nickel, 2009).

The structure map of Unit A shows the general dip direction is to the southwest (**Figure 7.4**). Deviations from a linear contour trend are likely related to faulting. Pitman et al. (2001) reported in the study covering the North Dakota portion of the Bakken Formation that the formation has various fracture types occurring on macroscopic and microscopic scales. In the middle member, most of these fractures are nonmineralized, horizontal, and discontinuous. They are believed to be hydrocarbon-generated features if bounding shale layers (upper and lower) are mature. They observed that fracture density in the middle member changes remarkably as a function of source-rock thickness and increases with the thickening mature shales. It is noteworthy that high levels of thermal maturity correspond to the burial depths greater than 3000 m (Pitman et al., 2001), which means the adjacent shales in this study area are immature. Therefore, the presence of hydrocarbon-generated fractures should be rare. However, there might exist mineralized fluid-release fractures during burial diagenesis due to sediment dewatering and lithification causing minor pore-pressure buildup and extension fractures created later during mild tectonic stress as noted by Pitman et al. (2001).

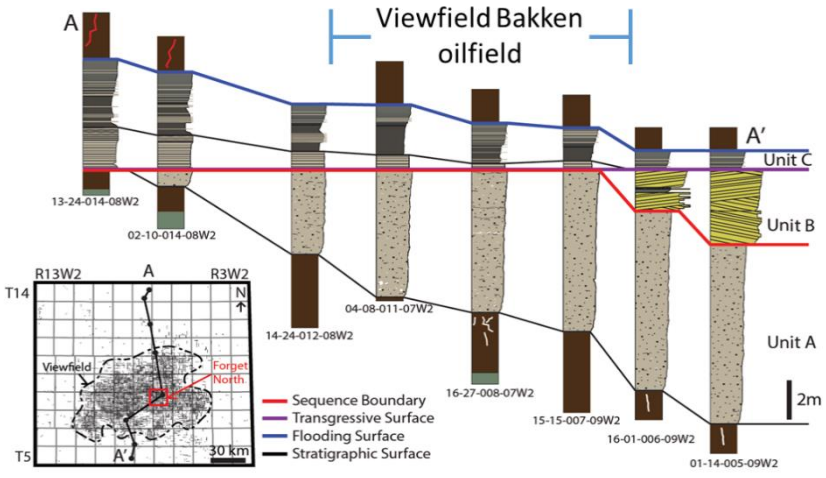

Figure 7.3 A N-S core cross section through the Viewfield Bakken oilfield (From personal communication with D. Cronkwright).

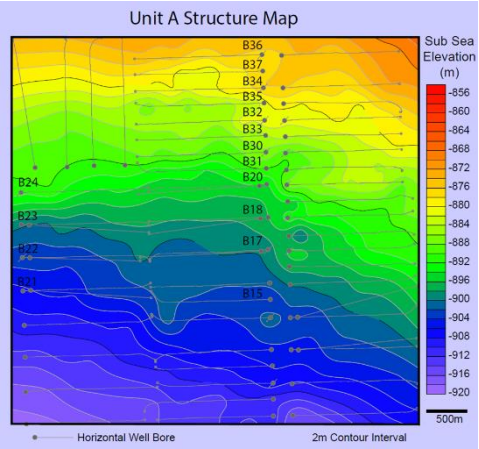

Figure 7.4 Structure map of the top surface of Unit A of the Bakken Forget North pilot study area. The map was produced using horizontal gamma ray logs, and picking the interface between Unit A and the overlying Unit C contoured using kriging (From personal communication with D. Cronkwright).

7.2 Connectivity Maps and Analysis

We ran the CM-PW for wells in the Forget North pilot waterflood study area. We have tracer test results and 3D seismic datasets from the field operator. After estimating connectivity parameters, we compare them with tracer tests and integrate seismic with connectivity.

7.2.1 Window size calculation in the tracer test area

We calculated window size of all injectors from the tracer test area. The tracer test area has 6 producers and 5 injectors (**Figure 7.5**). Three isotopes were placed in the southernmost 3 injectors – B13-inj, B11-inj and B9-inj. All direct offset producers produced some amount of tracer and with similar arrival times. Breakthrough times were less than 24 hours to the offset producers. Since the offset producers received tracers earlier than the expected time, the produced tracers were unintentionally re-injected in all injectors in the injection system. Therefore, the tracers were

found in the northernmost producers as well, but tracer arrival times on these producers were not measured. The operator found a direct fracture connection between wells B9-inj and B10.

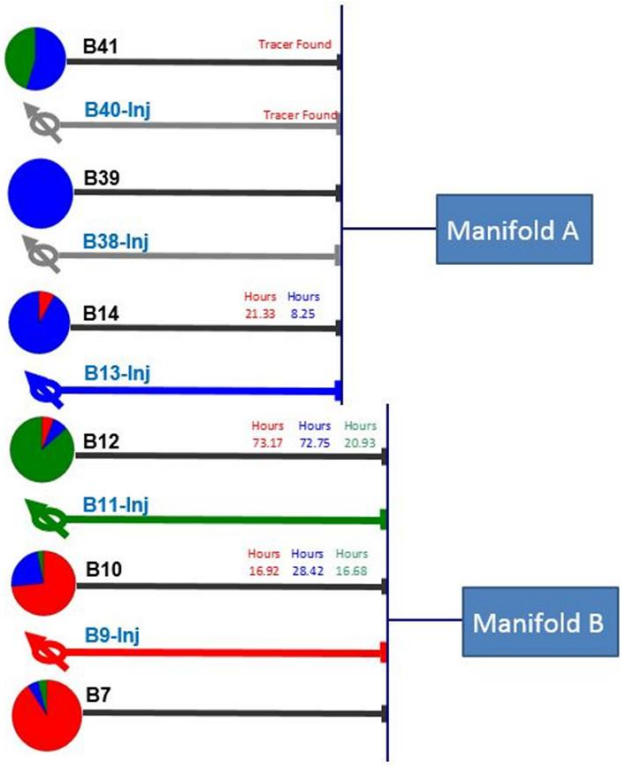

Figure 7.5 Producer based tracer arrival times and concentrations shown with three colors: blue, green, red. Tracers were placed in the southernmost 3 injectors (Courtesy of CPE).

Following the steps described in Chapter 4 (Section 4.3), we determined frequencies and amplitudes of all injectors in the area (**Table 7.1**). Using the median injector frequency, we created sinusoidal injection signal to be employed in the simulation model (**Figure 7.6**). The model has similar IWD as the area has. The simulation model has permeability of 0.09 md. The simulation is run to acquire flow rates to be used for the CM-PW analysis. Then, we plot λ vs IWD to find IWD at $\lambda_{cut\ off} = 0.1$ (**Figure 7.7**). We estimated R_ε using the median injector frequency in the area and plotted with respect to the IWD. On the area R_ε vs IWD plot, R_ε at IWD = 1080 ft equals to $3.4*10^{-12}$ (**Figure 7.8**).

Table 7.1 Frequency and amplitude of injectors from the tracer test area

Well	B9-Inj	B11-Inj	B13-Inj	B38-Inj	B40-Inj
Frequency, cycle/month	0.03	0.07	0.05	0.04	0.07
Amplitude, rb/day	15.5	11.2	29.1	42.5	22.9

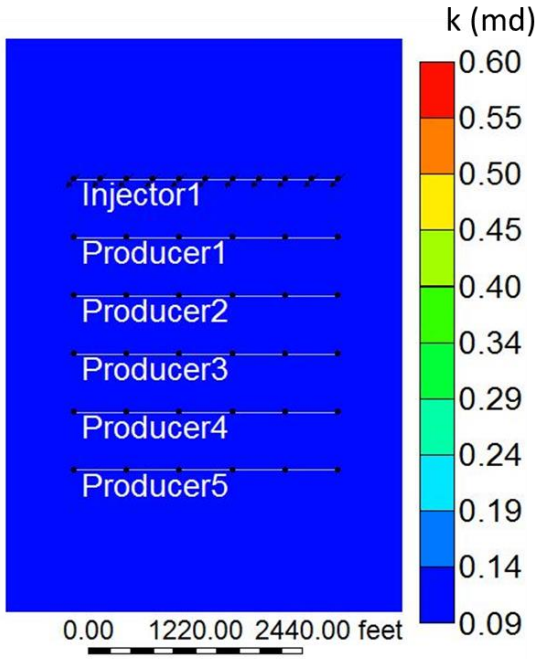

Figure 7.6 Schematic view of a homogeneous simulation model with an injector and 5 producers

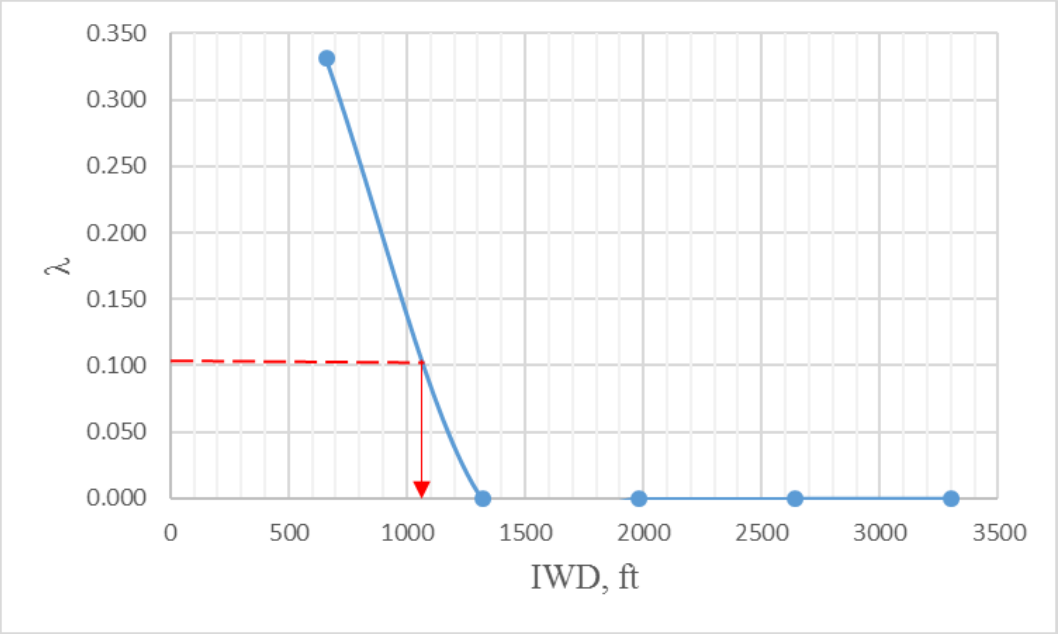

Figure 7.7 Corresponding interwell distance at $\lambda_{cut\ off}$ = 0.1. IWD = 1080 ft.

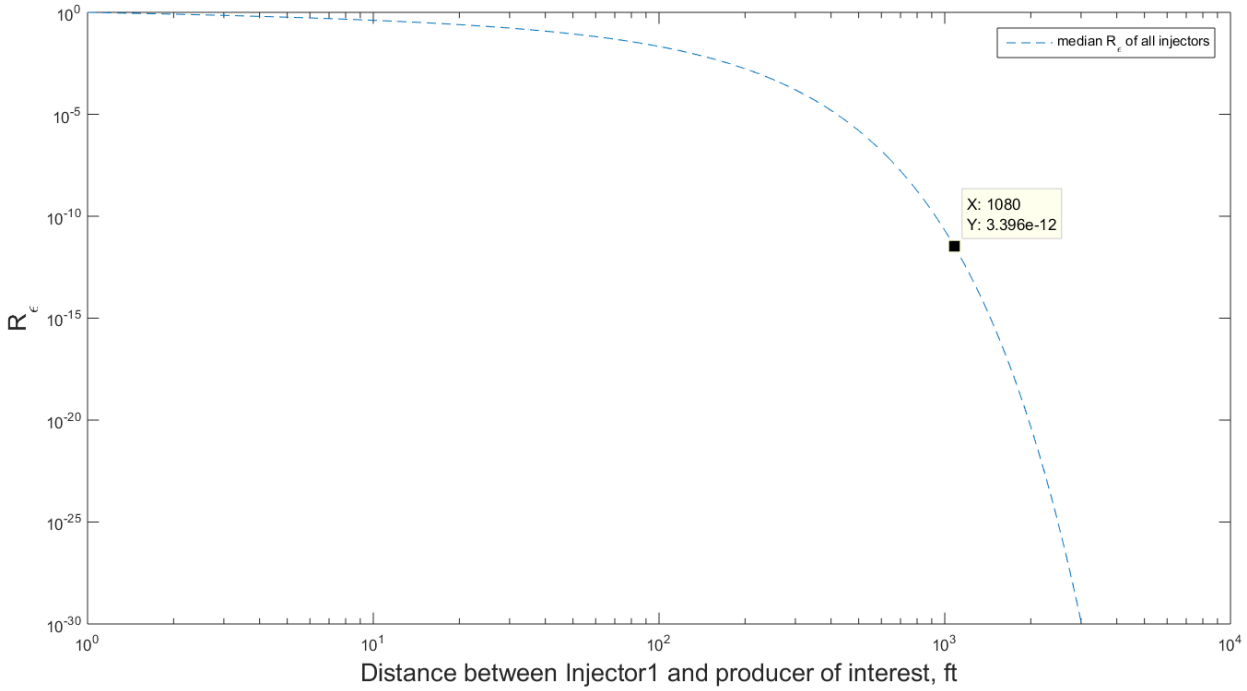

Figure 7.8 Area Rε plot. The critical $R_ε$ at IWD = 1080ft. $R_ε = 3.4*10^{-12}$.

After estimating $R_{\varepsilon\text{-crit.}}$, we determined maximum distance of influence of each injector (**Table 7.2, Appendix 2**). The median distance of influence is 1080 ft. The median IWD to offset well in the area is approximately 663 ft. Since the area has horizontal wells in serial arrangements as in waterflooding (**Figure 7.5**), any producer after the first offset producer is around 1989 ft away. This distance is greater than 1080ft. Therefore, it is recommended to choose wells for connectivity analysis within the corresponding distance found from the Emittance ratio plot.

Table 7.2 Injectors' distance of influence at $R_{\varepsilon\ crit.} = 3.4*10^{-12}$.

Well	B9-Inj	B11-Inj	B13-Inj	B38-Inj	B40-Inj
Distance of influence at $R_{\varepsilon\ crit.}$, ft	1391	914	1080	1206	914

In the following section, the connectivity analysis reveals that most wells with IWD > 1080 ft have $\lambda < 0.1$.

7.2.2 Connectivity maps

First, we divided the wells in the area into two groups: wells in the tracer test area and the rest of the wells in the pilot area. A timeline of the wells used in the tracer test highlights the important events in their history (**Figure 7.9**). We ran the CM-PW for the tracer test area including all wells in one window to identify possible long distance connections (**Figure 7.10**) and also divided the area into 3 smaller windows; Window B40-B38, Window B13-B11 and Window B9 (**Table 7.3**). The high R^2 values suggest to us that the model is working well. Since the wells in the analysis were put into production for at least a year before the period starts, we did not observe any pre-production effects i.e., λ_p's ~ 0 in Eq. 3-1. L > 4 was also preserved in each analysis period to avoid overfitting.

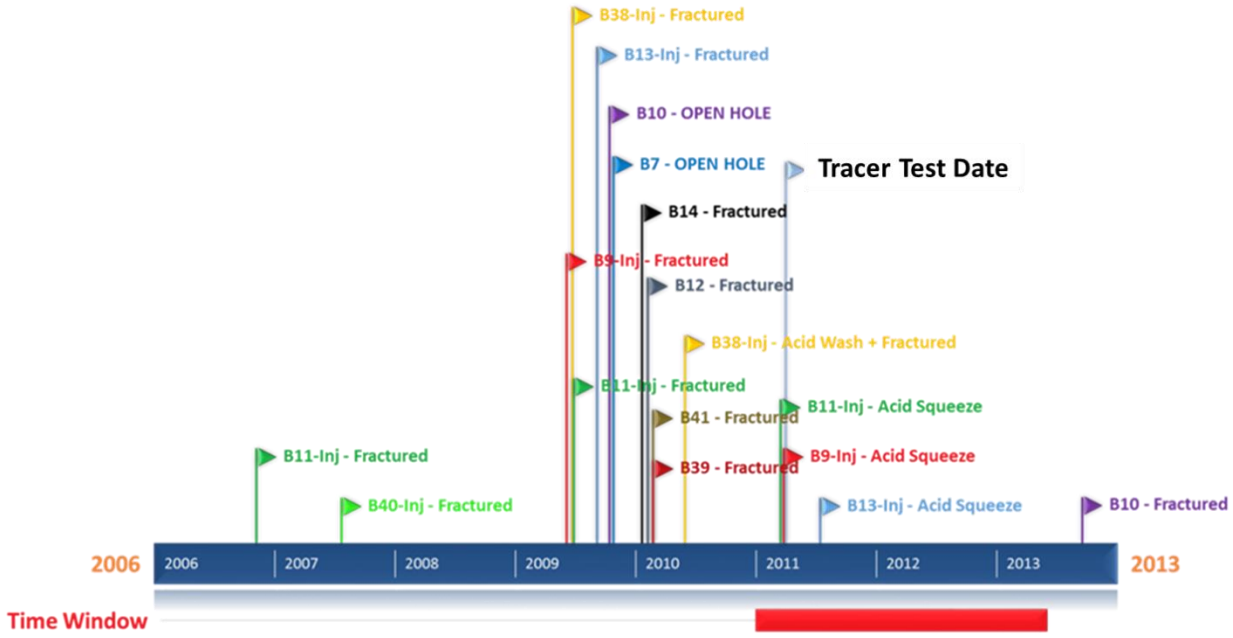

Figure 7.9 Timeline of the wells used for the tracer test (tracer test: March 23, 2011)

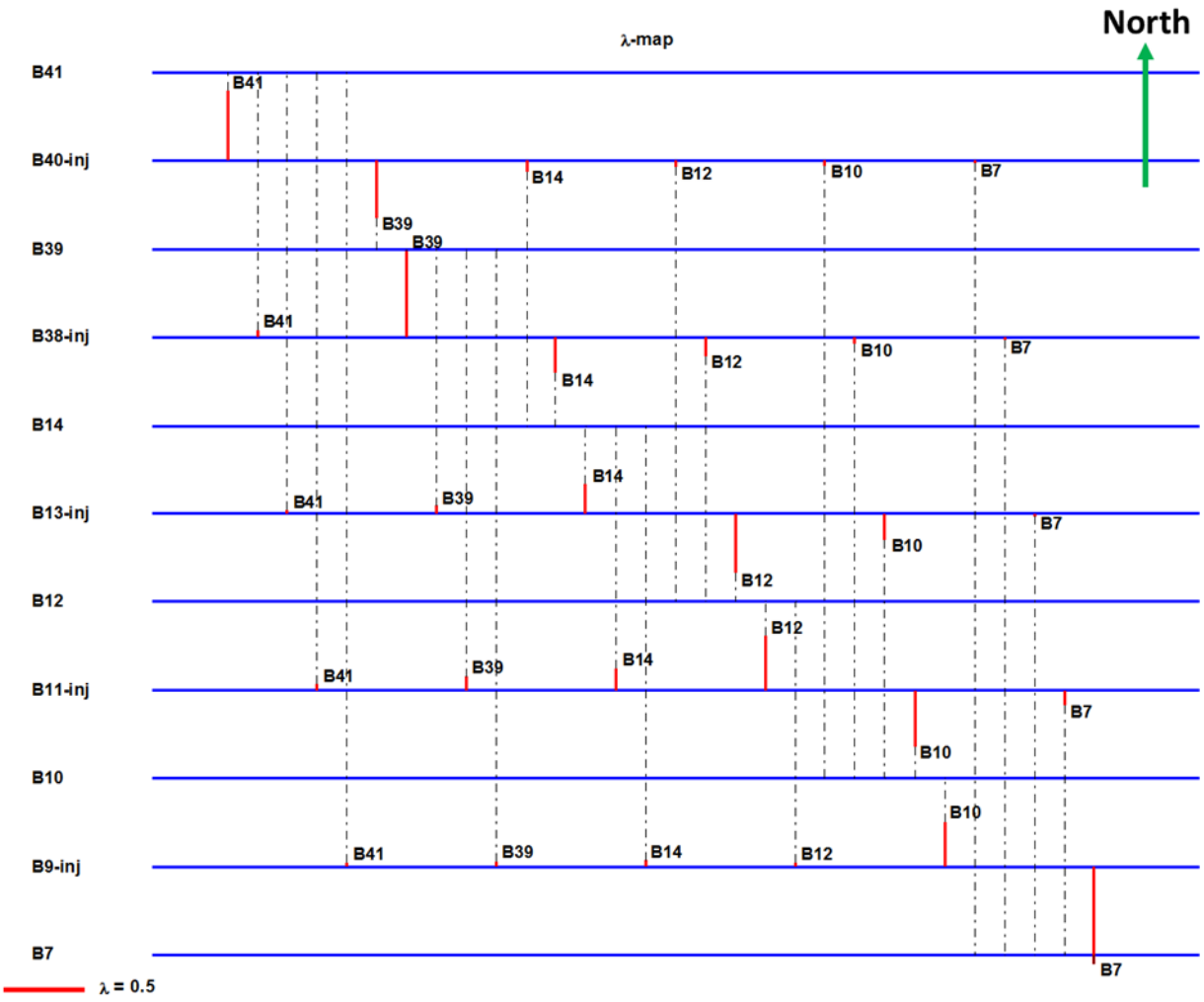

Figure 7.10 Connectivity map of the tracer test area. Each blue horizontal line represents one of the horizontal wells. The dashed lines originating from injectors connect injector-producer pairs. Solid red lines show the magnitude of a connection (λ) by their length. The connectivity between offset pairs is shown with an order that the wells are introduced to the model.

Table 7.3 Wells inside windows and R^2 (predicted vs measured total rate match) of windows. The tracer test area is divided into 3 smaller windows to include producers within the median distance of influence determined in Section 7.2.1. The large R^2 values suggest that the model can predict measured total rate with good accuracy.

Windows	Wells inside windows	R^2
Window B40-B38	B40-inj, B38-inj, B41, B39, B14	0.94
Window B13-B11	B13-inj, B11-inj, B14, B12, B10	0.79
Window B9	B9-inj, B10, B7	0.90

The connectivity analysis for the rest of the pilot area wells was conducted and the connectivities were mapped (**Table 7.4, Figure 7.11**). These results were employed for more analyses together with the evaluated and interpreted geological and geophysical data to characterize the field in detail.

The window B20-B17 does not have equal well spacing compared to other windows. That might be the reason why this well has the lowest R^2 among all. Having wells unequally spaced may affect model estimates, thereby resulting in poor match quality.

Table 7.4 Wells inside windows and R^2 (predicted vs measured total rate match) of windows.

Windows	Wells inside windows	R^2
Window B37-B34	B37-inj, B34-inj, B45, B37, B35	0.93
Window B32-B30	B32-inj, B30-inj, B35, B33, B31	0.93
Window B20-B17	B20-inj, B17-inj, B31, B18, B15	0.82
Window B24-B22	B24-inj, B22-inj, B23, B21	0.98

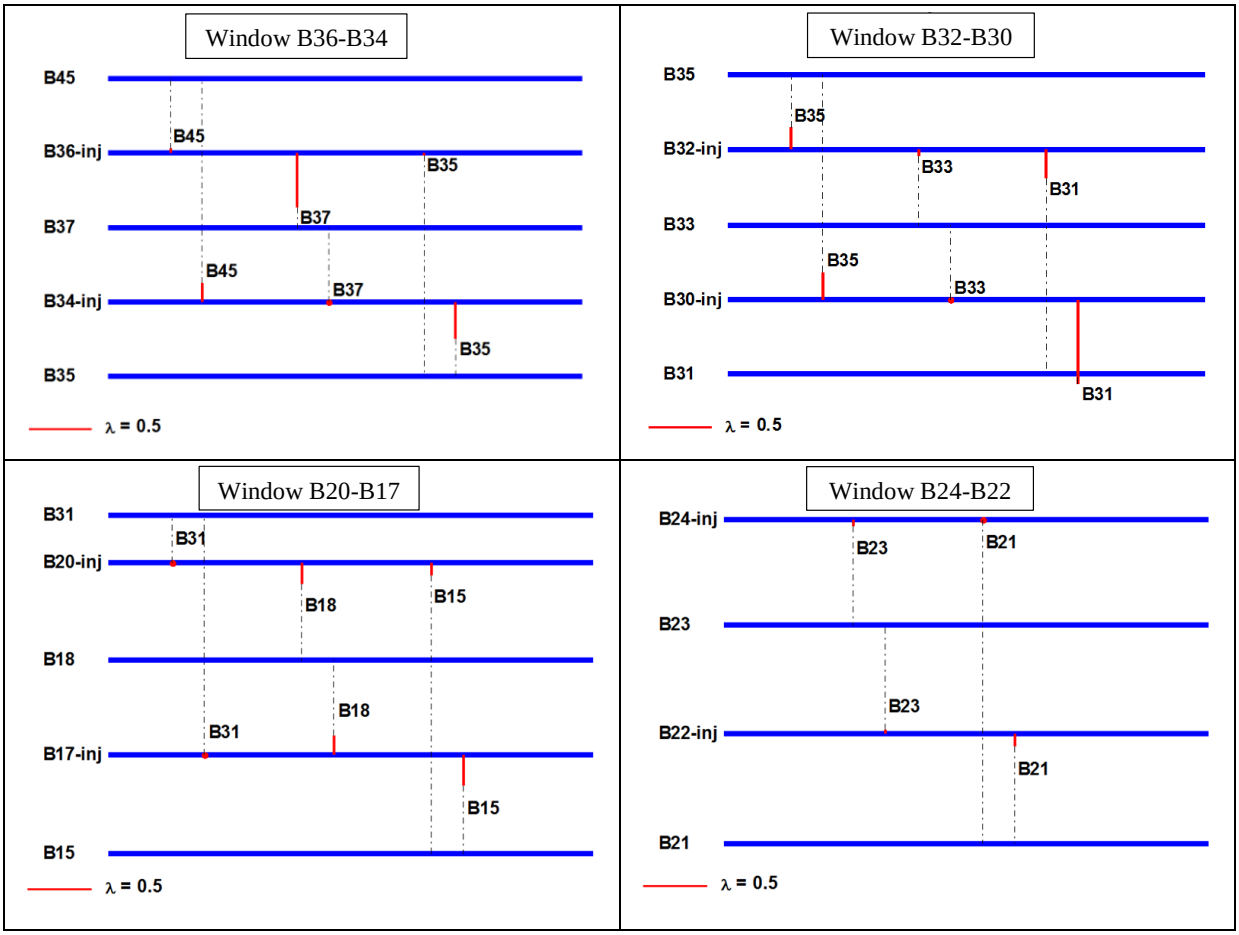

Figure 7.11 Connectivity maps of other windows from the Forget North pilot area

7.2.3 Comparison of CM-PW results with tracer tests

The operator of Forget North conducted a tracer test in the east section of the area (**Figure 7.**5). Tracer percentages at producers B14, B12 and B10 reveal strong levels of connection with injectors B13-inj, B11-inj, and B9-inj, respectively (**Figure 7.12**). As highlighted in the timeline (**Figure 7.9**), the tracer injected wells were acid squeezed during the analysis period, which may have increased the apparent connectivities.

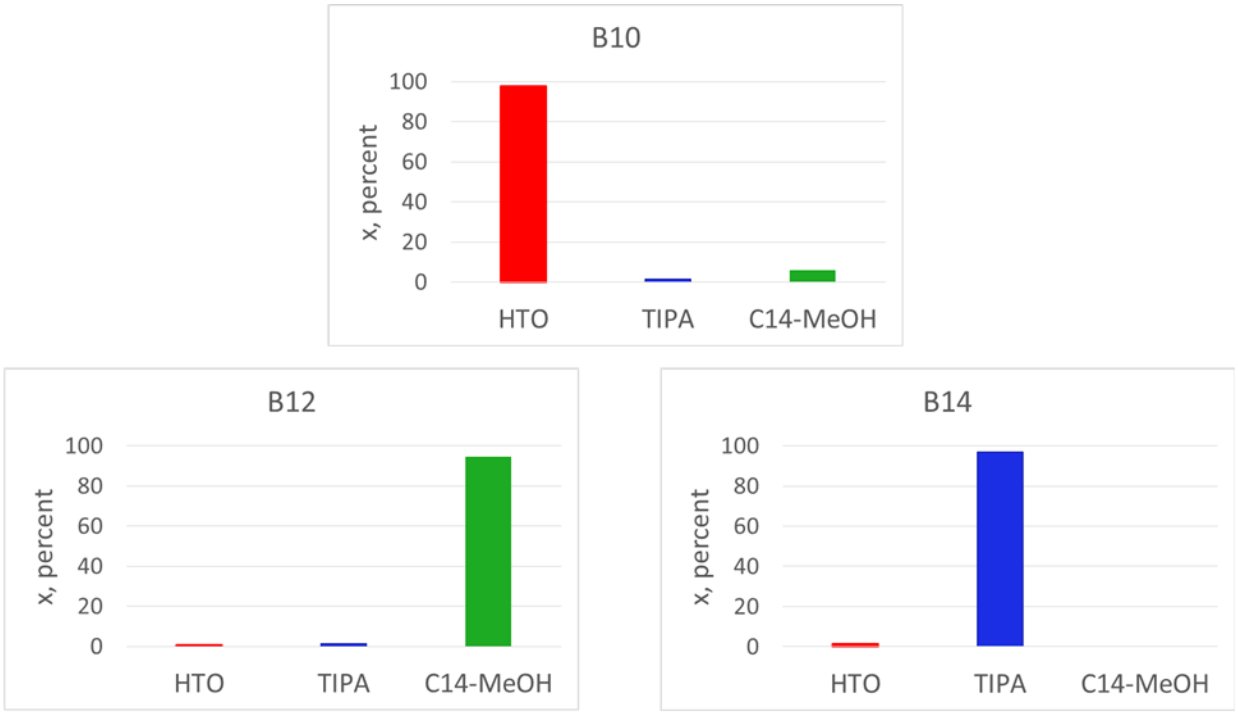

Figure 7.12 Percent of tracer samples at producers B14, B12 and B10 (B9-inj: HTO – tritiated water, B11-inj:TIPA – tritiated isopropyl alcohol, B13-inj:C14-MeOH – methanol with C14)

The map of CM-PW λs (**Figure 7.10**) shows that larger connectivities are directed towards the north in the northern region and towards the south in the southernmost part. In the central part, they are more balanced. This is similar to the tracer results (**Figure 7.5**). For example, well pair B9-inj and B7 shows a large CM connectivity (**Figure 7.10**) similar to the results in **Figure 7.5**. Even though the tracer test did not always indicate a strong connection between an injector-producer pair, such as B12 – B13-inj, the connectivity analysis results show that to be the case. The acid squeeze into injectors, run after the tracer test, may have contributed to the good connections with offset producers (i.e., B9-inj and B7). As expected, most of the direct offset producers have moderate to large connectivities with the injectors.

Using a plot of the λ vs percent of tracer (from **Figure 7.12**) arriving at the producers B10, B12 and B14, we set percent of tracer > 95% as "fracture hit" zone (**Figure 7.13** – above orange line). For the uncertainty assessment in connectivity, we apply bootstrap in one of window areas. The average change in connectivity is around ± 0.1, which is noted in **Figure 7.13** caption as well.

These well pairs establish their first and likely shortest connection through fractures. The wells connected through rock bodies had a small amount of tracer. Disconnected wells, as measured by the CM-PW with $\lambda < 0.1$ received negligible tracer amounts.

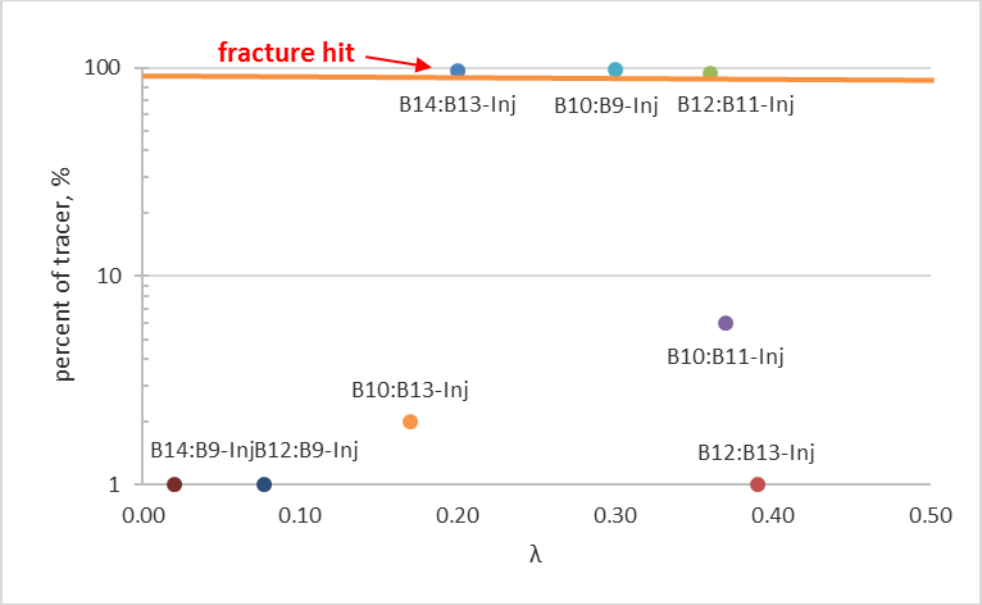

Figure 7.13 Percent of tracer vs λ. Pairs above the orange line are assumed to be connecting via fracture hits. The operator found a direct fracture connection between B9-Inj and B10. Tracer percentages at producers B14, B12 and B10 reveal strong levels of connection with injectors B13-inj, B11-inj and B9-inj, respectively. IWC is subject to statistical variation: λ ± 0.1. Due to this variation, there might be a pair with relatively strong connection which received a negligible amount of tracer (e.g., B12:B13-Inj).

7.2.4 Integration of connectivity, seismic, and geological information

In addition to the geological findings, geophysical evaluations are another important source of information to better characterize the study area. Hence, we interpreted two adjacent 3D seismic datasets available in this study area, which were called A and B (**Figure 7.14**). Both datasets consist of post-stack seismic data. Seismic attributes are useful tools for detecting sub-seismic fractures or faults and geological lineaments which are below the seismic resolution but which could affect connectivity. To this end, after interpreting seismic horizons, the volumetric curvature attributes were estimated. Among different curvature attributes, the azimuth of maximum dip of seismic traces shows some important features that may be related to the sub-seismic

faults/fractures or lithology changes in the reservoir (**Figure 7.15**). The possible fault/fracture direction or lithology changes are shown with the dashed lines. These sub-vertical horizontal faults/fractures are consistent with the area geology.

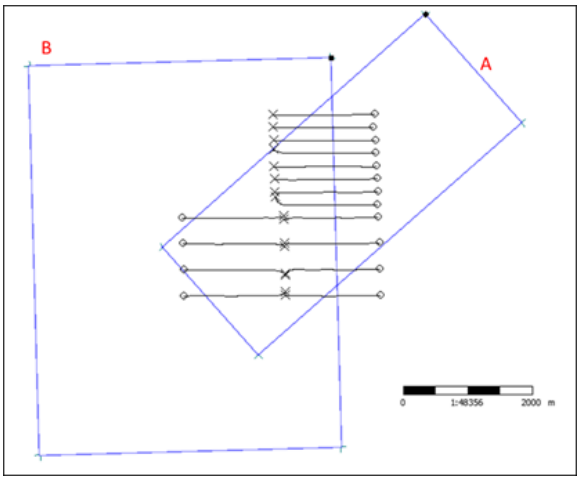

Figure 7.14 Seismic basemap with the wells which are used in the connectivity analysis.

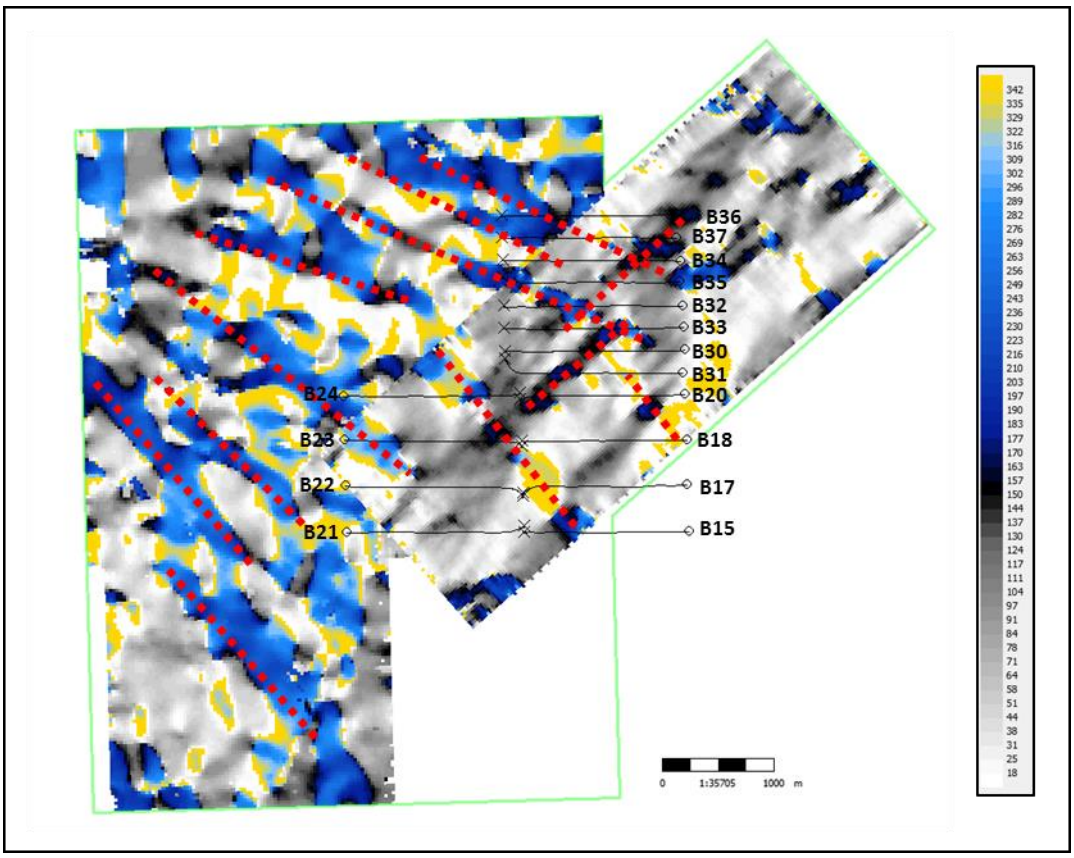

Figure 7.15 Curvature attribute map-azimuth at maximum dip attribute with possible sub-seismic faults/fractures or barrier shown with the dashed lines. The color scale indicates the azimuth value at maximum dip of the seismic horizon in the reservoir.

Geology of the field and the seismic results, therefore, suggest that wells can establish hydraulic connections in a variety of ways including natural fractures between wells, thief zones, low permeability matrix, hydraulic fractures extending from one well to an offset well, hydraulic/natural fractures connecting the Lodgepole aquifer and wells, and any combination of any of these. To better understand and characterize connection types between wells, we used the tracer test results and the CM-PW derived connectivities.

Short-term connectivity is directly affected by fractures while in the longer term, reservoir rock capable of transmitting fluids will also play a role in the connection between wells. Therefore, we looked at acoustic impedance (AI), which is the product of the density and velocity and can detect rock and fluid changes in the reservoir. Besides lithological variations, the AI in this

formation may also be related to fracture abundance, with smaller AI values indicating greater fracture density.

The average relative acoustic impedance map in the reservoir zone is shown in **Figure 7.16**. In this figure, the higher impedance values are masked and shown in a light color to be able to focus on the lower relative acoustic impedance distribution. Pairs with large connectivities such as B30-inj – B31 are partly located in a faults/fractures-free area (**Figure 7.15**) and partly located in an area with a lower relative AI, where there may be a high fracture density facilitating the connectivity. On the other hand, the well pair B30-inj – B33 is located at the northern limit of the area with the low relative AI and exhibits small connectivity.

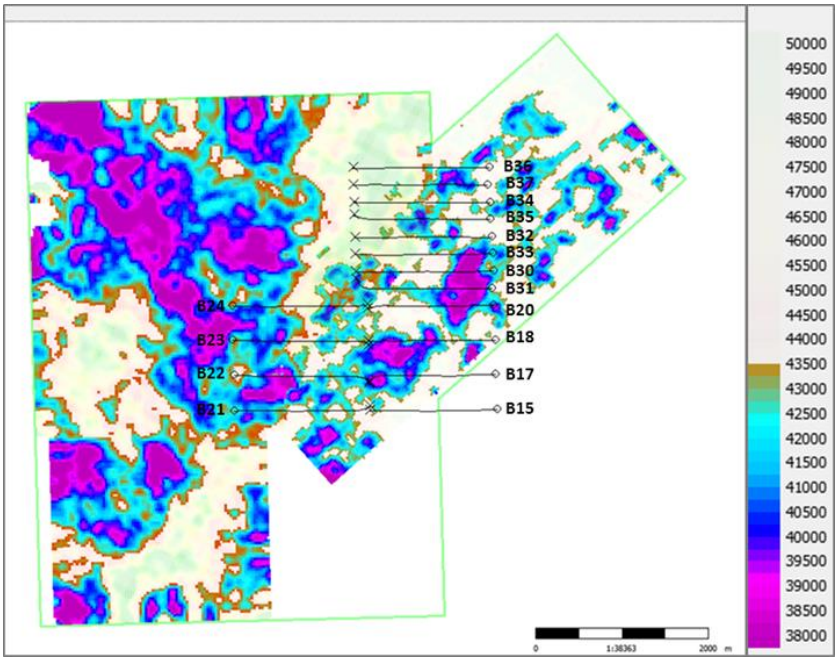

Figure 7.16 The average relative acoustic impedance over the reservoir interval. The color key is normalized and the higher values are masked and shown in light color. The lower values of relative acoustic impedance are purple.

A cross section of the relative AI volume which crosses horizontal wells in the target area shows similar results (**Figure 7.17**). The wells which have good connectivity have low values of relative AI. For example, wells B30-inj and B31 have good connectivity with low relative AI. Similarly, for well pair B37-inj and B37, also have good connectivity and low relative AI.

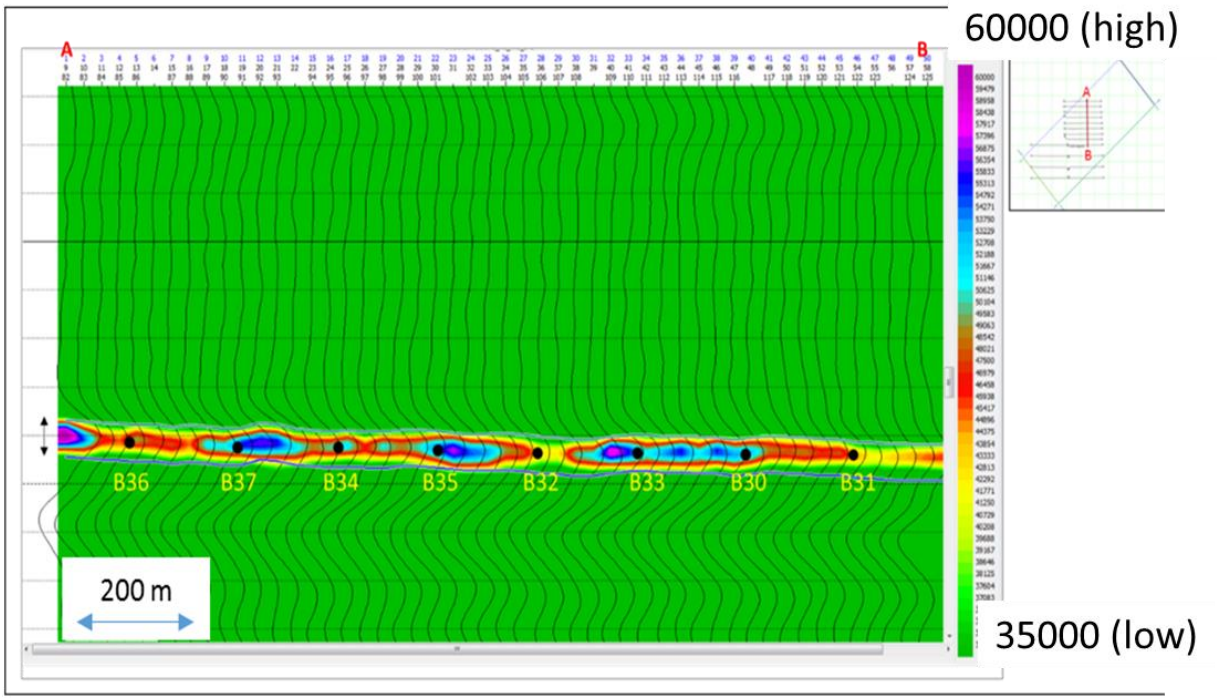

Figure 7.17 A seismic section of relative acoustic impedance volume in direction of A-B which is shown in the basemap (top right). The arrow on the left shows the reservoir zone.

To analyze these results more quantitatively, one section of the target area was divided into different zones (**Figure 7.18**). This section was chosen because the injector-producer well distances are small, i.e., 750 ft, compared to other sections, which reduces the effect of lithological heterogeneity between wells. Each zone is surrounded by an injector and a producer. As the relative AI decreases, the connectivity between wells clearly increases (**Figure 7.16**).

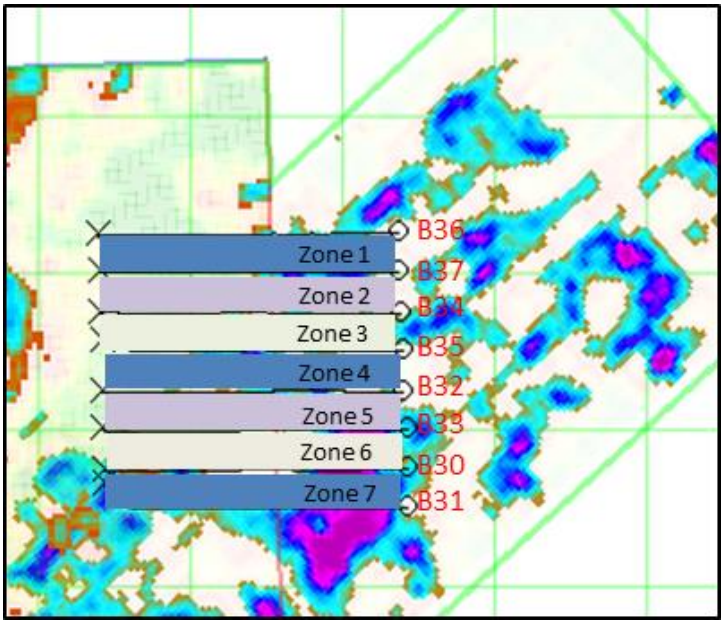

Figure 7.18 Division of the target area to 7 zones.

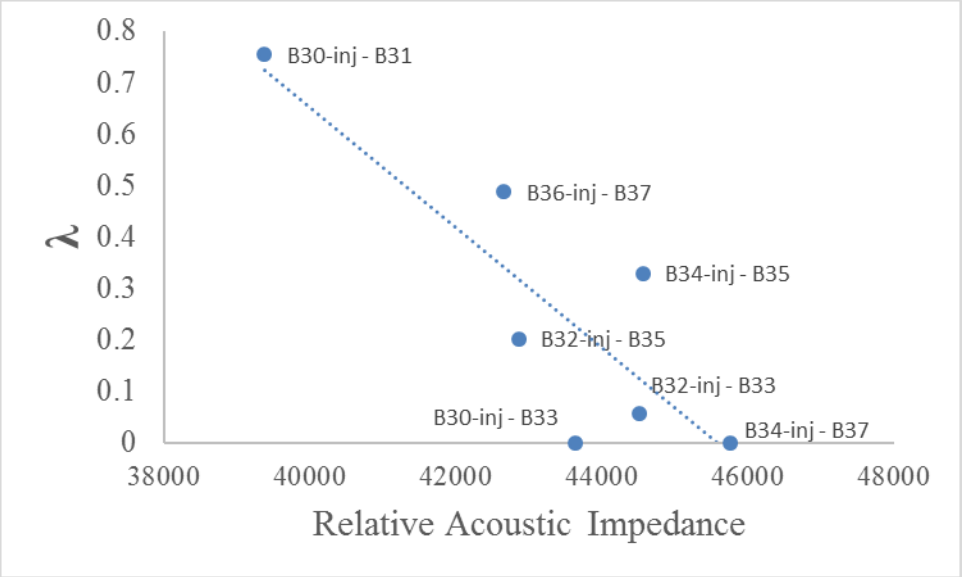

Figure 7.19 A comparison between the average relative acoustic impedance in the area between wells and IWC. R^2 = 0.72 and the regression line slope is non-zero at the 0.017 level of probability.

We also plotted the maximum AI in an area, $(AI)_{max}$, versus connectivity for non-neighboring well pairs, i.e. those well pairs with 1300 feet or larger distances between the wells (**Figure 7.20**). We observe a threshold behavior, which can be used to predict connectivity for

corresponding AI values. The behavior is consistent with the idea that IWC is limited by the densest, least fractured part of the rock in the interwell area. Such a non-linear response also agrees with the percolation-based behavior of geosystem connectivity, which has been observed elsewhere (e.g., Larue and Hovadik, 2007; Li et al., 2009; Sadeghnejad et al., 2012).

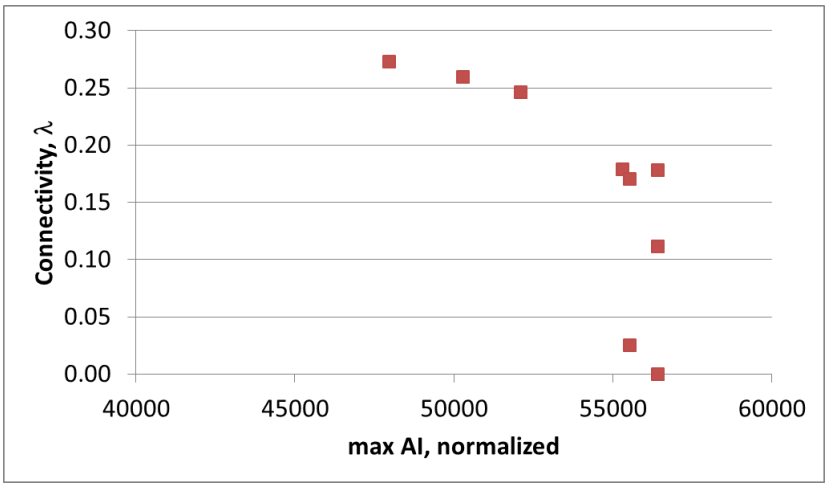

Figure 7.20 Maximum AI vs connectivity of non-neighboring wells shows a "threshold" behavior.

7.3 Discussion

Most of the long distance fracture-to-fracture connections may be lost as depletion continues within the fracture system (Sardinha et al., 2014). Therefore, we do not expect the fracture-to-fracture connection between a non-offset injector-producer pair existing during the water flooding. Some might argue that fractures created during stimulation may have closed and might not re-open during injection. In this pilot area, the flooding started within two years of fracturing most of the wells, which means the long term established production may not have started yet (Merkle et al., 2013). Therefore, the major fractures are likely still open during this period and injected fluid preferentially followed the paths through these fractures. Tracer test results also support this, showing that the breakthrough times to the offset wells were less than 24 hours. In low permeability reservoirs, it is unlikely for injected fluid to travel this fast through the reservoir matrix. In addition to the injected fluid flowing through natural/hydraulic fractures, the fluid taking the longest pathways will also eventually reach the producers. Now a question arises as to what will be the CM-PW response when a combination of fracture-to-fracture and geological flow paths exists. Since the CM-PW is a perturbation-based model, it will evaluate mainly the

effect of the dominant connection type, which is likely to be the fracture-to-fracture connection if both types exist. As the permeability contrast decreases, which is an unlikely case in this study, the volume of these paths will become a controlling factor.

Using **Figure 7.20**, we can determine maximum AI value at which $\lambda = 0$, no interwell connection between an injector-producer pair. This value can be used for future areas of the field to determine $\lambda_{cut\ off}$ for window size. **Figure 7.20** also reveals that connectivity does not change for $(AI)_{max} > \sim 56300$, which means increasing $(AI)_{max}$ does not affect λ or there are no parts of the reservoir with $(AI)_{max}$ above 56000. **Figure 7.19** can be used to determine likely connection type dominating interwell region as presented in following pages. This information can be helpful for constructing a geomodel to be used for reservoir simulation runs.

The median injector distance of influence showed that injectors' effect does not reach to producers after the first offset producer. The wells located beyond 1080 ft are expected to have $\lambda < 0.1$. Some wells still having weak connections with distant wells might communicate through 'extension' fractures (Pitman et al., 2001) or vertical leaking faults/fractures (hydraulic/natural) connecting them via the Lodgepole aquifer. We have depicted some of these vertical faults using a horizontal gamma ray log and deviation survey (**Figure 7.21**). Hassen et al. (2012), reporting on the wells drilled in the Viewfield area, noted that, in certain wells, water production was low during the pre-frac period but that it increased drastically during the post-frac period. We observed similar behavior in some of the wells including B24 (**Figure 7.22**). Prior to fracture stimulation, the water cut was below 20%. After fracking, the water cut exceeded 90%. This observation suggests that the distant wells which are not communicating through natural faults/fractures may have connections through the aquifer.

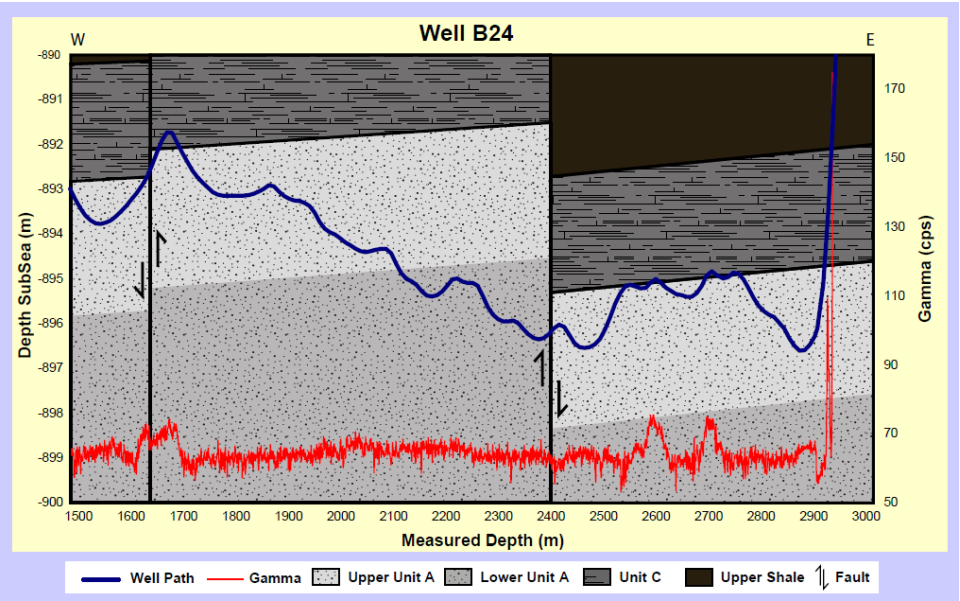

Figure 7.21 Horizontal cross section of Well B24 with the gamma ray log and deviation survey.

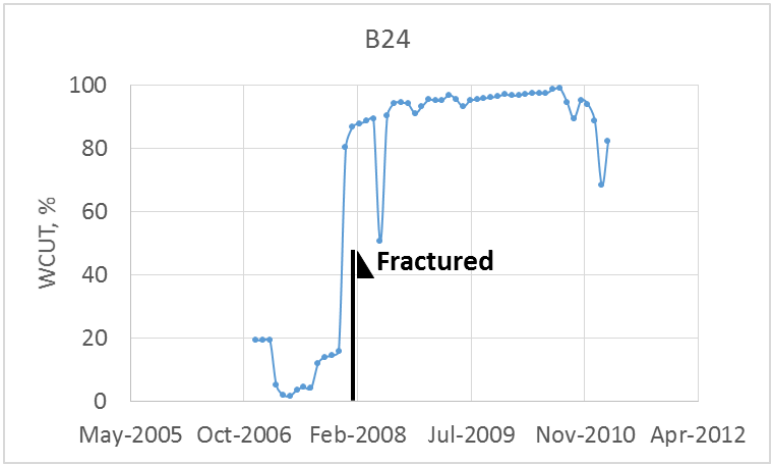

Figure 7.22 Water cut plot of B24.

Another group of wells established fast connections through natural/hydraulic fractures (**Figure 7.23**). The last group of wells connects with injectors through the reservoir matrix (**Figure 7.24**). The highest water cut in producer B18, having a moderate level of connection with the offset injectors (**Figure 7.10**), does not exceed 40%.

The discussion in this part guided us to propose connection types between the wells within the seismic basemap and the non-neighbor well pairs with $\lambda > 0.1$. We labeled the pairs from the

Figure 7.19 with the most likely connection type (**Figure 7.25**), which sheds a light on the causes of variability in the λs. Next, **Table 7.5** shows the list of the non-offset well pairs having $\lambda > 0.1$ with their connection types and the most likely causes. Data types used for clarification are also listed in the **Table 7.5**.

Figure 7.23 Water cut plots of B10 and B14; the starting dates of the offset injectors shown.

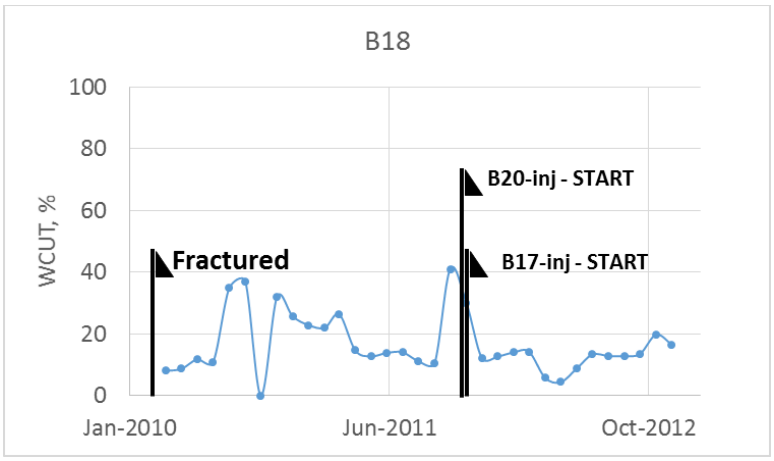

Figure 7.24 Water cut plot of B18; the starting dates of the offset injectors shown.

Table 7.5 Most likely causes of the connection between non-offsets well pairs. λ > 0.1 used as a connectivity threshold

well pair	connection type	most likely cause	supporting data
B30-inj - B35	moderate geo-connection through the aquifer	natural/hydraulic fractures and aquifer	water cut plot
B32-inj - B31	moderate geo-connection through the aquifer	natural/hydraulic fractures and aquifer	water cut plot
B11-inj - B14	moderate geo-connection	reservoir matrix	water cut plot
B13-inj - B10	moderate fracture connection	hydraulic & natural fracture networks	tracer test

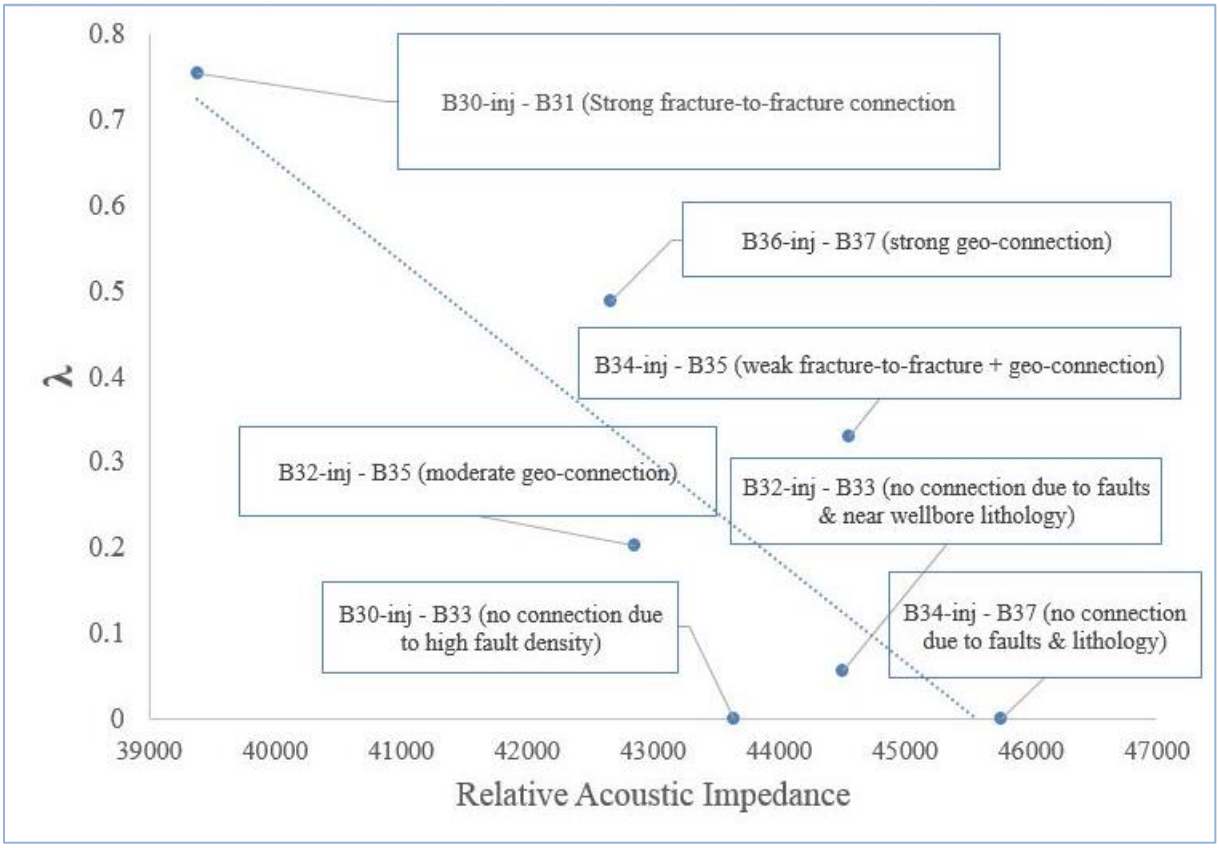

Figure 7.25 Average relative acoustic impedance vs connectivity plot revisited. The likely connection types are identified.

7.4 Conclusions

The field case study from the Bakken Forget North area revealed that

- the CM-PW is very helpful to identify key controlling factors on HW IWC and correlate the values with geological and seismic analyses.
- More than 90% of tracers flowed through fracture-to-fracture connections.
- Once a connection was confirmed by the CM-PW, checking water cut plots with the events timeline suggested a dominant connection type controlling IWC.

- IWC decreases as relative acoustic impedance increases.
- Spectral analysis and R_ε plots of all injectors in the tracer test area showed that the median of injectors' maximum distance of influence is about 1080 ft, which means beyond this distance injectors' effect on producer will reduce.
- IWD at $\lambda_{cut\ off}$ is within 3% change of IWD from the R_ε plot.
- The CM-PW can help us to identify dominant connection types like fracture connection and connection through an aquifer.
- The existence of the Lodgepole Formation aquifer was the cause of a long distance connectivity. Some well pairs established connection through the vertical faults and Lodgepole aquifer.

CHAPTER 8: CONCLUSIONS AND RECOMMENDATIONS FOR FUTURE WORK

In this research, we developed the CM-PW, a modified version of the CM, to make the model useful for tight reservoir IWC evaluation. This modification allows us to apply the model to any size areal window. We introduced a way to determine optimum window size for the CM-PW application. Depending on the injection well frequency and the field diffusivity, the normalized well pressure-based effect coefficient is estimated. Once we can calculate its critical value, we can determine the radius/distance of well influence which determines the spatial window size. Finally, we applied the CM-PW to field data from the east Pembina Cardium and the Viewfield Bakken oilfields.

8.1 Conclusions

We draw several conclusions from this investigation:

1. We have modified the CM to account for interactions outside an area of interest. Applying the CM-PW to field and synthetic cases, we observed that the CM-PW can

- accurately evaluate connectivities within 7% variation when wells are excluded from a windowed area.
- obtain a good match between predicted and actual production with $R^2 \geq 0.85$ for Horizontal well (HW) and $R^2 \geq 0.97$ for Vertical well (VW) .
- evaluate connectivities where a significant part of the production history includes transient flow, provided that more than 30% of the history includes pseudo-steady state flow
- facilitate the analysis of connectivities during the period having a long production decline profile. After the decline period, having $L > 4$ is enough for the model to estimate reliable connectivity values.

2. We found that the CM-PW works well in tight formations when we decrease injection signal frequency to less than a cycle per year.

3. From the surface plots, we found signal amplitude does not have a significant effect on λ and τ, yet diffusivity definitely does.

Well emittance rate, ε and its ratio, R_ε study results:

3. We found that the effect of decreasing signal frequency on the R_ε ratio decreases as the model diffusivity increases, which means we can find a diffusivity value of a model where changing signal frequency will not affect R_ε.
4. We have described the method for estimating window size for vertical and horizontal wells to be used in the CM-PW application. Applying method in field cases confirmed that the method could give us an approximate areal window size to include surrounding wells in the analysis.
5. R_ε simply showed how a change in a parameter of interest affects well emittance as interwell distance increase.
6. R_ε shows how diffusivity and injection signal frequency content impact nearby producers.
7. Both **Figures 4.4** (R_ε plots for different diffusivities) and **6.10** (λ surface plot of increasing diffusivity and signal amplitude) are in good agreement. As diffusivity increases, λ and R_ε increase.

East Pembina Cardium oilfield study results:

8. The model results were helpful to observe how IWC was affected by net local stress.
9. The CM-PW detected the conglomerate layer within parts of and outside the area window.
10. There was an obvious relation between λ' ($\lambda_{heterogeneous} - \lambda_{homogeneous}$) and flow capacity.
11. Early time IWC of fractured wells depends on net local stress.
12. The IWC study showed there exists a significant hydraulic continuity between the well pair having an interwell distance of 1916 ft, which reveals sandbodies is likely to be extending laterally from well to well.
13. In the Window area 2, for $L \geq 3.4$, we obtained a very good match between the CM-PW predicted and measured rates for all the three periods with $0.95 \geq R^2 \geq 0.89$.

The Viewfield Bakken oilfields study results:

14. More than 90% of tracers flowed through fracture-to-fracture connections in the tight oil reservoir, which revealed how detrimental fracture hits can be during flooding.
15. We were able to identify key controlling factors on HW IWC and correlate the values with geological and seismic analyses.
16. HW IWC decreases as relative acoustic impedance increases
17. Checking water cut plots with the events timeline suggested a dominant connection type controlling IWC.
18. A threshold behavior between IWC and maximum Acoustic impedance values was found, which agrees with the percolation-based behavior.
19. Interwell connectivity vs Interwell distance and Emittance ratio vs Interwell distance are in accordance with each other

8.2 Recommendations for future work

The following future work recommendations are suggested:

1. In Optimization problems, landing on local minima/maxima might give misleading results. To avoid this issue, using global search algorithms along with parallel computing might be a solution. From Kaviani et al. (2014), we know that increasing amount of noise increases variability in the model estimates. It would be interesting to investigate the effect of noise on the Global search results.
2. With the help of the response surface analysis, we can find optimum values for the parameters of interest to increase interwell connectivity. To achieve better connection and minimize the cost, using the optimum values is recommended. There is another way to test effectiveness of these optimum values. We can build a reservoir simulation model of the field employing the optimum values. Once model is ready, we can simulate it and run the CM-PW with simulated flow rates. In this way, we can test IWC before proceeding to the real field development.
3. Emittance rate equation assumes homogeneous model. We also used same assumption in our calculations. This, however, may not be correct. Therefore, testing the model for heterogeneous

cases is recommended. The permeability term inside the diffusivity term can be estimated as an average value of the heterogeneous case.

4. We linked CMG © and CM-PW, which was used as an automated model. The noise from the simulation model was causing some deviation from true values. In the automated model, noise detection and filtering mechanism can be added to the model.

5. Sampling time affects our model results. The effect of sampling time can be investigated with the Emittance rate (ε) equations. The ε equation has a time term in it. Estimating the ε for different time intervals would give us that.

6. With the Emittance ratio, it is possible to estimate the radius/distance of injector influence. During field development stage, estimating radius of injector influence and plotting them on a map is recommended to find potential spots for infill drilling.

7. We can create the Emittance rate plot for wide range of frequencies. It is possible to find frequency content of interwell connectivities by plotting interwell connectivities on the plots of ε vs IWD. This might be another way of finding range of signal frequencies used in the field.

8. Initializing the optimization problem with appropriate starting point would help us a lot to find correct estimates. Time delay (τ) can be correlated with the water breakthrough time since injection. The initial τ value for optimization is assigned with random value. Rather than setting random τ for the starting point, employing correlation for τ with respect to water breakthrough time since injection is recommended.

9. In a field developed with horizontal wells, we can find amount of fluid reaching to the producer from the surrounding injectors by summing the product of interwell connectivity (λ) and injection rate (w). Then, plotting $\sum \lambda w$ vs q_{oil}, one can find out how much barrels of oil produced for a barrel of water injected.

10. For the constrained optimization problem of the CM-PW, we need to set upper and lower boundaries for the interwell connectivity (IWC). The relationship between IWC and Acoustic impedance was clear. Employing this relationship can be useful to set upper and lower boundary for initial IWCs during the optimization process.

11. With the Fast Fourier Transform, we can find the signal frequency. Tracking footprint of injection frequency in the production spectral analysis might be a way for the screening of

connected well pairs to be used in the IWC analysis. In this way, we can eliminate unconnected well pairs before applying the model.

REFERENCES

Alberta Energy Regulator. (2014). AER Database: Tour Reports – East Pembina Field Wells

Bansal, Y., & Sayarpour, M. (2012). *Fault-Block Transmissibility Estimation Using Injection and Production Data in Waterfloods*. Paper SPE-159067-MS presented at the SPE Annual Technical Conference and Exhibition San Antonio, Texas, 8-10 October. doi:10.2118/159067-MS

Bell, J.S., Price, P.R., McLellan, P.J. (1994). Chapter29-In-situ Stress in the Western Canada Sedimentary Basin; Geological Atlas of the Western Canada Sedimentary Basin, Mossap, G.D., & Shetsen, I. (1994). Canadian Society of Petroleum Geologists and Alberta Research Council. Retrieved from http://ags.aer.ca/publications/chapter-28-geological-history-of-the-peace-river-arch.htm

Blakey, R.C. (2017). Western Interior Seaway. Retrieved from http://deeptimemaps.com/western-interior-seaway-thumbnails/

Borcovsky, D., Egenhoff, S., Fishman, N., Maletz, J., Boehlke, A., Lowers, H. (2017). Sedimentology, facies architecture, and sequence stratigraphy of a Mississippian black mudstone succession – The upper member of the Bakken Formation, North Dakota, United States. *AAPG Bulletin*, v. 101, NO.10, pp. 1625-1673.

Braunberger, W.F., Hall, R.L. (2001). Ammonoid faunas from the Cardium Formation (Turonian-Coniacian, Upper Creataceous) and contiguous units, Alberta, Canada: I. Scaphitidae. *Canadian Journal of Earth Sciences. 38*: 333-346. doi: 10.1139/cjes-38-3-333

Butrenchuk, E.W., Cornish, S.A., Leggit, S.M., & Mills, M.M. (1995). *The Impact of Facies on Reservoir Performance; Pembina Cardium Reservoir, Alberta*. Presented at CSPG/CWLS 1995 Core Session: The Economic Integration of Geology and Formation Evaluation. Canadian Society of Petroleum Geologists, Pages 1-32.

Cao, F., Luo, H., & Lake, L. W. (2014). *Development of a Fully Coupled Two-phase Flow Based Capacitance Resistance Model (CRM)*. Paper SPE-169485 presented at the SPE Improved Oil Recovery Symposium Tulsa, Oklahoma, 12-16 April. doi:10.2118/169485-MS

Carslaw, H.S, & Jaeger, J.C. (1959). *Conduction of Heat in Solids*. Oxford: Clarendon Press. Print.

Chen, H., Zhang, Z., Sun, W., & Li, K. (2010). *Modification of Capacitance-Resistive Model for Estimating Waterflood Performance*. Paper SPE-129783 –MS presented at the International Oil and Gas Conference Beijing, China, 8-10 June. doi:10.2118/129783-MS

Clarkson, C.R., & Pedersen, P.K. (2011). *Production Analysis of Western Canadian Unconventional Light Oil Plays*. Paper CSUG/SPE 149005 presented at the Canadian Unconventional Resources Conference Calgary, Alberta, 15-17 November.

Crescent Point Energy – CPE. (2015). Forget North Pilot Area Reservoir Rock and Fluid Properties.

Cronkwright, D.J., Pedersen, P.K., Spencer, R.J. (2014). *Detailed Reservoir Characterization of the Middle Bakken Formation – Viewfield Pool, SE Saskatchewan.* Paper presented at the GeoConvention Calgary, Alberta, 4-8 May.

Cronkwright, D.J. (2017). Integrating Sedimentology, Sequence Stratigraphy and Mineralogy to Evaluate Controls on Hydrocarbon Accumulation and Production in the Bakken Formation of Southeast Saskatchewan (Master's Thesis). Retrieved from https://prism.ucalgary.ca/handle/11023/4105

Demiryurek, U., Banaei-Kashani, F., Shahabi, C., & Wilkinson, F. G. (2008). *Neural-Network based Sensitivity Analysis for Injector-Producer Relationship Identification*. Paper SPE-112124presented at the Intelligent Energy Conference and Exhibition Amsterdam, The Netherlands, 25-27 February. doi:10.2118/112124-MS

Dinh, A. V., & Tiab, D. (2007). *Inferring Interwell Connectivity from Well Bottom Hole Pressure Fluctuations in Waterfloods*. Paper SPE-106881-MS presented at the Production and Operations Symposium Oklahoma City, Oklahoma, 31 March – 3 April. doi:10.2118/106881-MS

Dinh, A. V., & Tiab, D. (2008). Inferring Interwell Connectivity from Well Bottomhole-Pressure Fluctuations in Waterfloods. *SPEREE*. doi:10.2118/106881-PA

Durand, E. (1966). *Électrostatique, Volume II: Problèmes Généraux Conducteurs*, Paris: Masson et Cie. Print

Ferrill, D.A., McGinnis, R.N., Morris, A.P., Smart, K.J., Sickmann, Z. T., Bentz, M., Evans, M. A. (2014). Control of mechanical stratigraphy on bed-restricted jointing and normal faulting: Eagle Ford Formation, south-central Texas. *AAPG Bulletin*, 98(11), 2477-2506.

Fic, J. D. (2013). *Characterization of the Lower Shoreface to Offshore Reservoir Facies of the Cardium Formation in East Pembina, Alberta* (Master's thesis). Retrieved from https://prism.ucalgary.ca/handle/11023/444

Fisher, M. K., & Warpinski, N. R. (2012). Hydraulic-fracture-height growth: Real data. *SPE Production & Operations*, 27(01), 8-19.

Gentil, P. H. (2005). *The Use of Multilinear Regression Models in Patterned Waterfloods: Physical Meaning of the Regression Coefficients* (master's thesis). Retrieved from https://www.pge.utexas.edu/research/theses/2005

Geoscout Database., 2017. Geoscout Database for Well Locations and Flow Rates.

Ghanizadeh, A., Clarkson, C.R., Aquino, S., Ardakani, O.H., & Sanei, H. (2015). Petrophysical and Geomechanical Characteristics of Canadian Tight Oil and Liquid-rich Gas Reservoirs: I. Pore Network and Permeability Characterization, *Fuel*, 153, 664-681, http://dx.doi.org/10.1016/j.fuel.2015.03.020

Ghori, S. G., & Heller, J. P. (1998). Well-to-well Tracer Tests and Permeability Heterogeneity, *Journal of Canadian Petroleum Technology*, 37(01), 32-43. doi:10.2118/98-01-06

Gillund, G.N. (1969). Review of the Lobstick Cardium miscible flood. *Journal of Canadian Petroleum Technology*, 8, 66-74.

Gough, D.I., & Bell, J.S. (1981). Stress orientations from oil-well fractures in Alberta and Texas. *Canadian Journal of Earth Sciences, 18*, 638-645.

Gough, D.I., Fordjor, C.K., & Bell, J.S. (1983). A stress province boundary and tractions on the North American plate. Letters to NATURE, *NATURE*. 305, 619-621.

Halabura, S., Costa, A., Danyluk, T., Prugger, A., & Nemeth, B. (2002). *Salt collapse or karst? A new model for reservoir development in Paleozoic carbonates of the Saskatchewan potash mining district*. Paper presented at the Canadian Society of Petroleum Geologists (CSPG) Meeting Calgary, Alberta, June.

Hassan, D. (1982). *A method for predicting hydraulic fracture azimuth and the implications thereof to improve hydrocarbon recovery*. Paper 82-33-19 presented at the 33rd Annual Technical Meeting of the Petroleum Society of Canadian Institute of Mining and Metallurgy Calgary, Alberta.

Hassen, B.R., Zotskine, Y., & Gulewicz, D. (2012). *Hydraulic Fracture Containment in the Bakken with a Synthetic Polymer Water Based Fracture Fluid*. Paper SPE-162670-MS presented at the SPE Canadian Unconventional Resources Conference Calgary, Alberta, 30 October – 1 November. doi:10.2118/162670-MS.

IHS Accumap. (2015). Well Location Map of the Forget North Pilot Area.

Izgec, O., & Kabir, C. S. (2009). *Establishing Injector/Producer Connectivity before Breakthrough during Fluid Injection*. Paper SPE-121203-MS presented at the SPE Western Regional Meeting San Jose, California, 24-26 March. doi:10.2118/121203-MS

Jansen, F. E., & Kelkar, M. G. (1997). *Application of Wavelets to Production Data in Describing Inter-Well Relationships*. Paper SPE-38876-MS presented at the SPE Annual Technical Conference and Exhibition San Antonio, Texas, 5-8 October. doi:10.2118/38876-MS

Johnson, C. R., Greenkorn, R. A., & Woods, E. G. (1966). Pulse-Testing: A New Method for Describing Reservoir Flow Properties Between Wells. *Journal of Petroleum Technology*, 18(12), 1599-1604. doi:10.2118/1517-PA

Kaviani, D. (2009). Interwell Connectivity Evaluation from Wellrate Fluctuations: A Waterflooding Management Tool (Doctoral dissertation). Retrieved from http://oaktrust.library.tamu.edu/bitstream/handle/1969.1/ETD-TAMU-2009-12-7553/KAVIANI-DISSERTATION.pdf?sequence=1

Kaviani, D., & Jensen, J. L. (2010). *Reliable Connectivity Evaluation in Conventional and Heavy Oil Reservoirs: A Case Study From Senlac Heavy Oil Pool, Western Saskatchewan*. Paper SPE-137504 presented at the Canadian Unconventional Resources and International Petroleum Conference Calgary, Alberta, 19-21 October. doi:10.2118/137504-MS

Kaviani, D. & Valkó, P.P. (2010). Inferring Interwell Connectivity Using Multiwell Productivity Index (MPI). *Journal of Petroleum Science and Engineering*, 73 (1-2), 48-58.

Kaviani, D., Jensen, J.L., & Lake, L.W. (2012). Estimation of Interwell Connectivity in the Case of Unmeasured Fluctuating Bottomhole Pressures. *Journal of Petroleum Science and Engineering*, 90-91 (1): 79-95.

Kaviani, D., Soroush, M., Jensen, J.L. (2014). How Accurate Are Capacitance Model Connectivity Estimates? *Journal of Petroleum Science and Engineering*, 122, 439-452.

Kendall, R. (2008). *Microseismic Monitoring of a Multi-Stage Frac in the Bakken Formation, SE Saskatchewan*; Paper presented at the CSPG CSEG CWLS Convention Calgary, Alberta. Retrieved from https://www.geoconvention.com/archives/2008/279.pdf

Khodaei, A., Lee, H., Banaei-Kashani, F., Shahabi, C., & Ershaghi, I. (2009). *A Mutual Information-Based Metric for Identification of Nonlinear Injector Producer Relationships in Waterfloods*. Paper SPE-121395-MS presented at the SPE Western Reginal Meeting San Jose, California, 24-26 March. doi:10.2118/121395-MS

Kloepfer, C. V., & J. D. Griffith, 1965. Solvent Placement improvement by pre-injection of water –Lobstick Cardium Unit, Pembina field. *Journal of Canadian Petroleum Technology*, *4*, 30-35.

Kohlruss, D., & Nickel, E. (2009). *A-6 Facies analysis of the Upper Devonian-Lower Mississippian Bakken Formation, southeastern Saskatchewan* (Report. 2009-4.1, Paper A-6, 11p).Retrieved from http://publications.gov.sk.ca/documents/310/37536-SOI2009V1_A6.pdf

Krause, F.F. & Nelson, D.A. (1984). *Storm event sedimentation: Lithofacies association in the Cardium Formation, Pembina area, west-central Alberta, Canada.* Paper presented at the Symposium on the Mesozoic of Middle North America Calgary, Alberta-Memoir 9, 485-511. Retrieved from http://archives.datapages.com/data/cspg_sp/data/009/009001/485_cspgsp0090485.htm

Krause, F.F., Collins, H.N., Nelson, D.A., Machemer, S.D., French, P.R. (1987). Multiscale Anatomy of a Reservoir: Geological Characterization of Pembina-Cardium Pool, West-Central Alberta, Canada. *AAPG Bulletin*, 71(10), 1233-1260.

Krause, F.F., Deutsch, K.B., Joiner, S.D., Barlcay, J.E., Hall, R.L., Hills, L.V. (1994). Cretaceous Cardium Formation of the Western Canada Sedimentary Basin. Geological Atlas of the Western Canada Sedimentary Basin; in Geological Atlas of the Western Canada Sedimentary Basin, G.D. Mossop and I. Shetsen (comp.), Canadian Society of Petroleum Geologists and Alberta Research Council. Retrieved from http://ags.aer.ca/publications/chapter-23-cretaceous-cardium-formation.htm

Larue, D.K., & Hovadik, J. (2006). Connectivity of channelized reservoirs: a modelling approach. *Petroleum Geoscience*, 12(4), 291-308.

LeFever, J.A., Martiniuk, C.D., Dancsok, E.F.R., Mahnic, P.A. (1991). *Petroleum Potential of the middle member, Bakken Formation, Williston Basin.* Paper presented at the Sixth International Williston Basin Symposium Grand Forks, North Dakota, 7 October. Retrieved from http://archives.datapages.com/data/sgs_wb_utf/data/0007/0074/0074.html

Li, W., Jensen, J.L., Ayers, W.B., Hubbard, S.M., & Heidari, M.R. (2009). Comparison of Interwell Connectivity Predictions Using Percolation and Geometrical Models and Monte Carlo Simulation, *Journal of Petroleum Science and Engineering*, 68, 180-186.

Liang, X., Lake, L. W., Edgar, T. F., Al-Yousef, A., Sayarpour, M., & Weber, D. (2007). *Optimization Of Oil Production Based On A Capacitance Model Of Production And Injection Rates*. Paper SPE-107713-MS presented at the Hydrocarbon Economics and Evaluation Symposium Dallas, Texas, 1-3 April. doi:10.2118/107713-MS

Liang, X. (2010). A simple model to infer interwell connectivity only from well-rate fluctuations in waterfloods. *Journal of Petroleum Science and Engineering*, 70(1–2), 35-43. doi:http://dx.doi.org/10.1016/j.petrol.2009.08.016

McLeod, J.G.F. (1987). Successful injection pattern alternation, Pembina J lease. *Journal of Canadian Petroleum Technology*, 17, 51-55.

Merkle, S., Lehmann, J., & Pyecroft, J. (2013). *Field Trial of a Cased Uncemented Multi-Fractured Horizontal Well in the Horn River*. Paper SPE-168928-MS presented at the Unconventional Resources Technology Conference Denver, Colorado, 12-14 August. doi:10.1190/URTEC2013-138.

Mirzayev, M., Riazi, N., Cronkwright, D., Jensen, J.L., & Pedersen, P.K. (2017). Determining well-to-well connectivity using a modified capacitance model, seismic, and geology for a Bakken Waterflood, *Journal of Petroleum Science and Engineering*, 152, 711-727. doi.org/10.1016/j.petrol.2017.01.032.

Moreno, G.A., & Lake, L.W. (2014). On the uncertainty of interwell connectivity estimations from the capacitance-resistance model. *Petroleum Science*, 11 (2): 265-271

Nguyen, A.P. (2012). Capacitance Resistance Modeling for Primary Recovery, Waterflood and Water-CO_2 Flood (Doctoral dissertation). Retrieved from https://repositories.lib.utexas.edu/handle/2152/ETD-UT-2012-08-6143

Palmer, I. D., Moschovidis, Z. A., & Cameron, J. R. (2007). *Modeling Shear Failure and Stimulation of the Barnett Shale After Hydraulic Fracturing*. Paper SPE-106113-MS presented at the SPE Hydraulic Fracturing Technology Conference College Station, Texas, 29-31 January. doi:10.2118/106113 MS

Pitman, J.K., Price, L.C., & LeFever, J.A. (2001). Diagenesis and Fracture Development in the Bakken Formation, Williston Basin: Implications for Reservoir Quality in the Middle Member. U.S. Geological Survey Professional Paper No. 1653, 19. Retrieved from https://pubs.usgs.gov/pp/p1653/p1653.pdf

Sadeghnejad, S., Masihi, M., Shojaei, A., Pishvaie, M., & King, P.R. (2012). Field scale characterization of geological formations using percolation theory. *Transport in porous media*, 92(2), 357-372.

Sardinha, C.M., Petr, C., Lehmann, J., Pyecroft, J.F., & Merkle, S. (2014). *Determining Interwell Connectivity and Reservoir Complexity Through Frac Pressure Hits and Production Interference Analysis*. Paper SPE-171628-MS presented at the SPE/CSUR Unconventional Resources Conference Calgary, Alberta, 30 September – 2 October. doi:10.2118/171628-MS

Sayarpour, M. (2008). Development and Application of Capacitance-Resistive Models in

Water/CO_2 Floods (Doctoral Dissertation). Retrieved from https://repositories.lib.utexas.edu/handle/2152/15357

Soeriawinata, T., & Kelkar, M. (1999). *Reservoir Management Using Production Data*. Paper SPE-52224-MS presented at the SPE Mid-Continent Operations Symposium Oklahoma City, Oklahoma, 28-31 March. doi:10.2118/52224-MS

Soroush, M. (2014). Interwell Connectivity Evaluation Using Injection and Production Fluctuation Data (Doctoral Dissertation). Retrieved from https://prism.ucalgary.ca/handle/11023/1285

Soroush, M., Kaviani, D., & Jensen, J. L. (2014) Interwell Connectivity Evaluation in Cases of Changing Skin and Frequent Production Interruptions. *Journal of Petroleum Science and Engineering*, 122, 616-630.

Stewart, G., and Gupta, A. (1984). *The Interpretation of Interference Tests in a Reservoir With Sealing and Partially Communicating Faults*. PaperSPE-12967-MS presented at the European Petroleum Conference London, UK, 22-25 October. https://www.onepetro.org/conference-paper/SPE-12967-MS

Theloy, C., & Sonnenberg, S. A. (2012). *Factors Influencing Productivity in the Bakken Play, Williston Basin*. Article presented at the AAPG Annual Convention and Exhibition Long Beach, California, 22-25 April.

Thiele, M. R. & Batycky, R. P. (2006). Using Streamline-Derived Injection Efficiencies for Improved Water flood Management, *SPE Reservoir Evaluation & Engineering*, 9(2): 187-196.

Weber, D. (2009). The Use of Capacitance-Resistance Models to Optimize Injection Allocation and Well /location in Water Floods (Doctoral Dissertation). Retrieved from The UT at Austin Electronic Theses and Dissertations.

Webber, K. J., & van Geuns, L. C. (1990). Framework for Constructing Clastic Reservoir Simulation Models. Journal of Petroleum Technology, 42(10), 1248-1297.

Yousef, A. A., Gentil, P. H., Jensen, J. L., & Lake, L. W. (2006). A Capacitance Model to Infer Interwell Connectivity from Production and Injection Rate Fluctuations. *SPE Reservoir Evaluation and Engineering*, 9(06), 630-646. doi:10.2118/95322-PA

Yousef, A.A. (2006). Investigating Statistical Techniques to Infer Interwell Connectivity From Production and Injection Fluctuations (Doctoral dissertation). Retrieved from https://repositories.lib.utexas.edu/handle/2152/2456

APPENDICES

Appendix 1: Testing simulation model flowrates for optimum grid size

In this appendix, we present the strategy we follow to determine final version of the simulation models. To evaluate the accuracy of simulation model flowrates, we test it with a large 2x1 simulation model with horizontal wells (**Figure A.1 – 1**). The model has 225x225xVLN number of grid cells. The VLN stands for Vertical Layer Number. Producers are left open-hole to avoid potential noise due to hydraulic fractures. We choose the finer grid cells as a benchmark level to compare with coarser grid cell cases. In order to reduce computational time, we want to find optimum cell size. 9 layers are chosen as a benchmark level. We look at the ratio of vertically coarser case Producer1 rates to the 9 layers case Producer1 rate. As cells get vertically coarser, the ratio fluctuates between 0.8 and 1.2 (**Figure A.1 – 2**). We also note that fluctuation range becomes narrower when the number of vertical layer gets closer to 9. For example, 7 layers case is almost similar to 9 layers case. Therefore, instead of 9 layers, we can choose 7 layers model to save computational time. Single layer case is within plus or minus 20 percent. If we choose this one, we will pay the price of deviation from likely accurate case. There might be additional noise affecting our optimization problem.

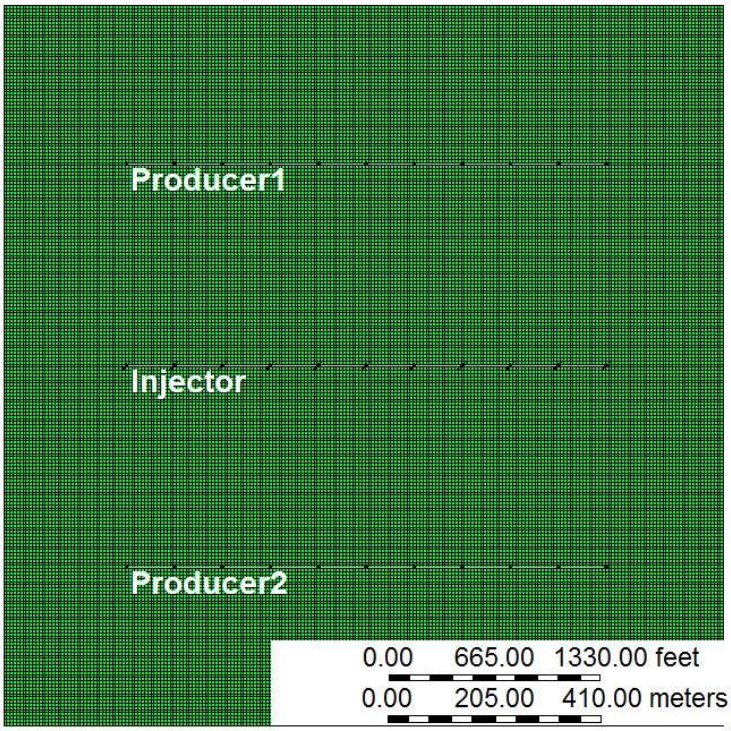

Figure A.1 – 1 2x1 Simulation model with horizontal wells.

7 Layers

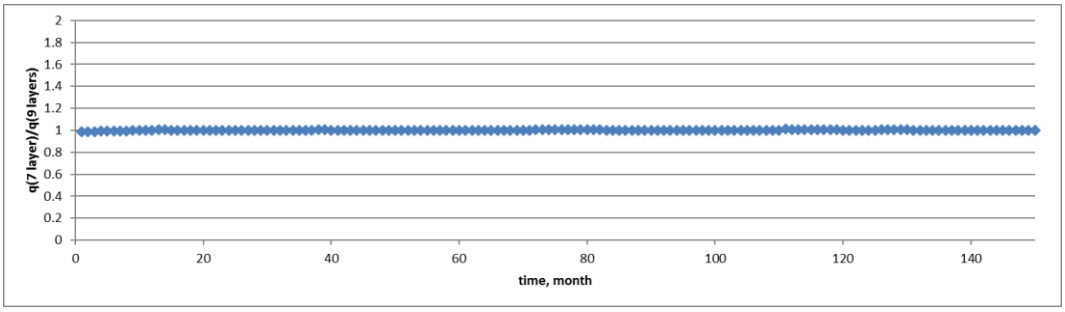

5 Layers

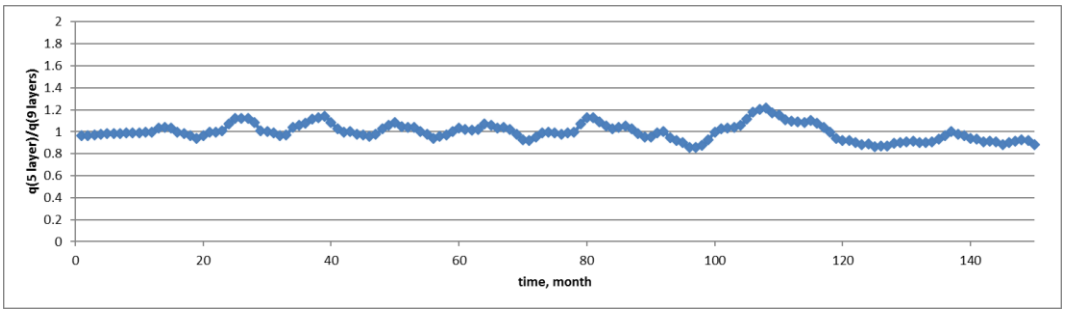

3 Layers

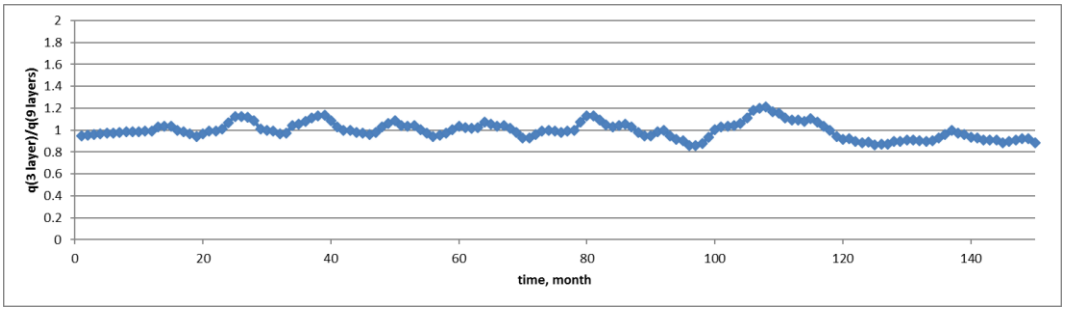

1 Layer

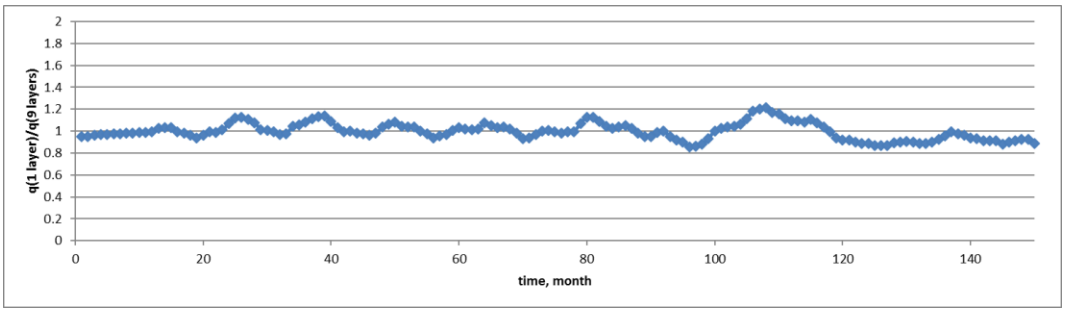

Figure A.1 – 2 Producer 1 flowrate ratio for different layer numbers

Appendix 2: R_{ε} plots of injectors in the tracer test area from the Forget North pilot area.

Using the injector f, and area diffusivity, we prepared R_{ε} plot of each injector. Then, $R_{\varepsilon\text{-crit.}}$ values are employed to determine injector distance of influence (**Figures A.2-1, A.2-2, A.2-3, A.2-4 and A.2-5**).

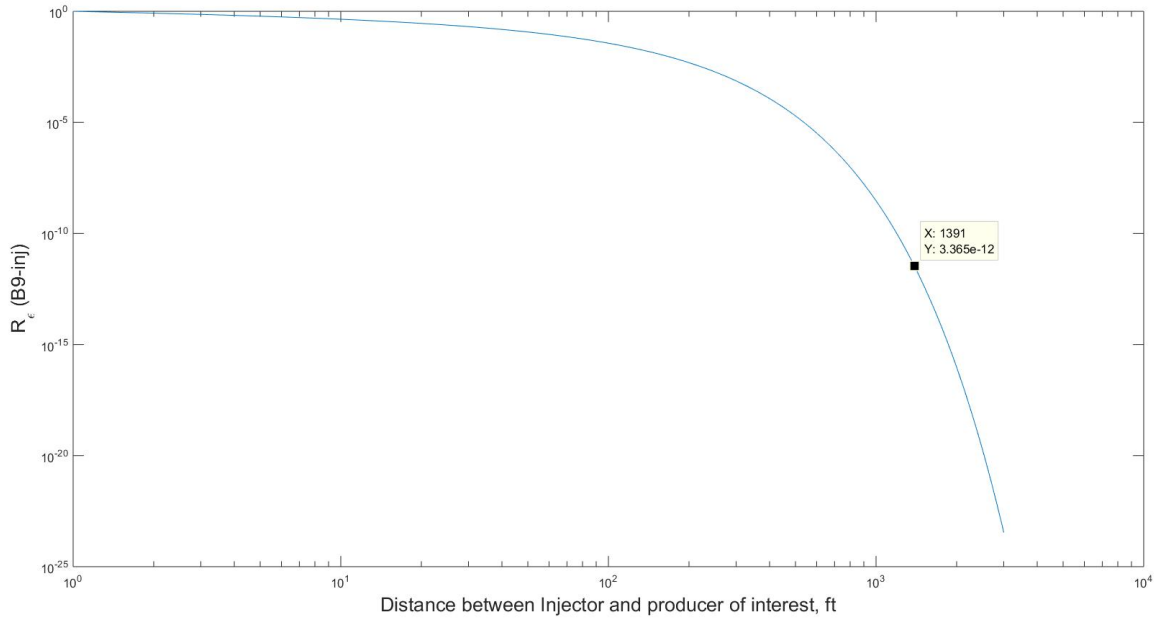

Figure A.2-1 B9-inj Rε plot

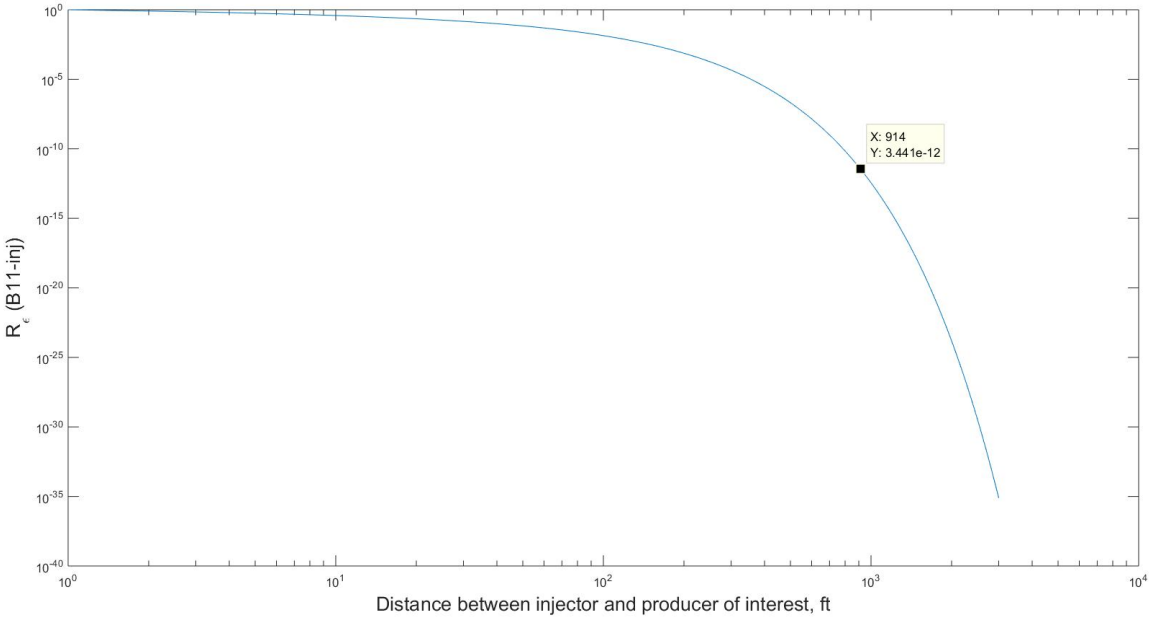

Figure A.2-2 B11-inj Rε plot

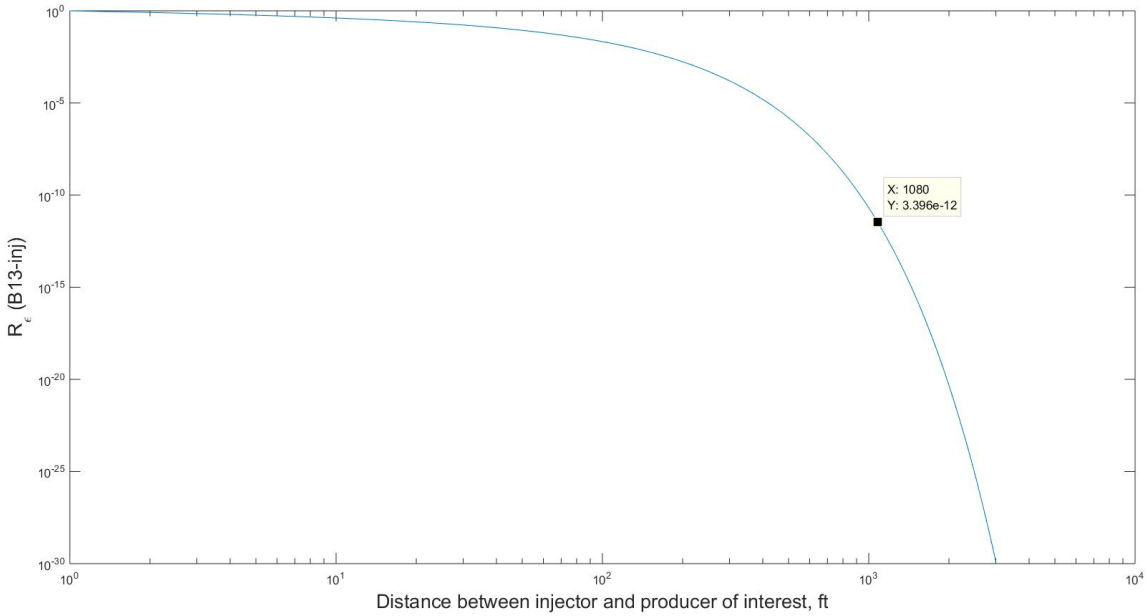

Figure A.2-3 B13-inj R_ε plot

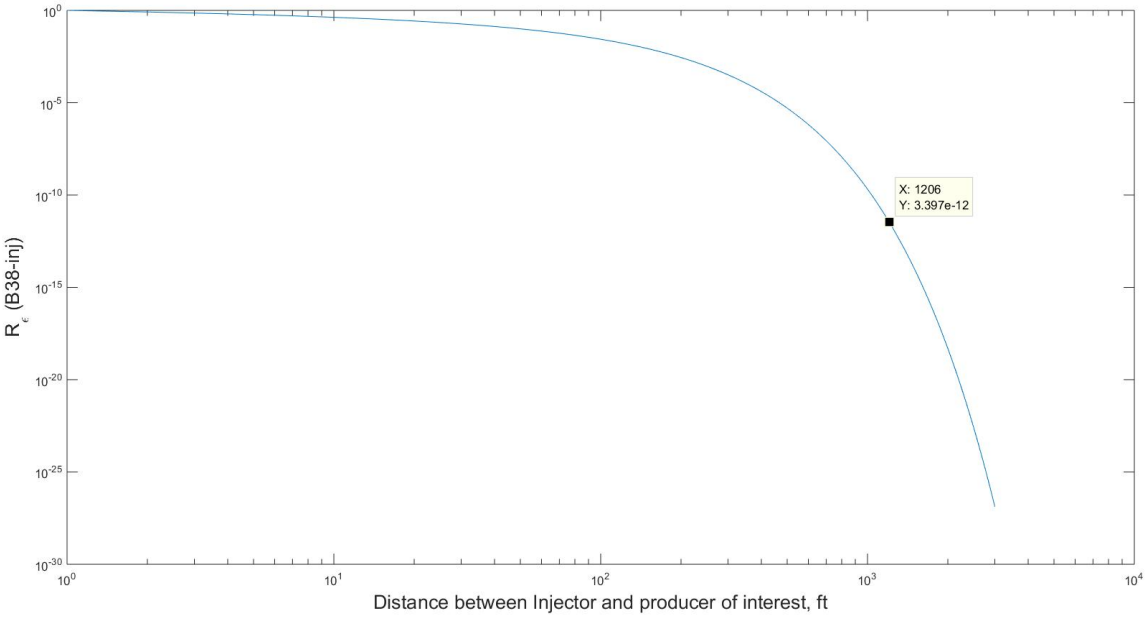

Figure A.2-4 B38-inj R_ε plot

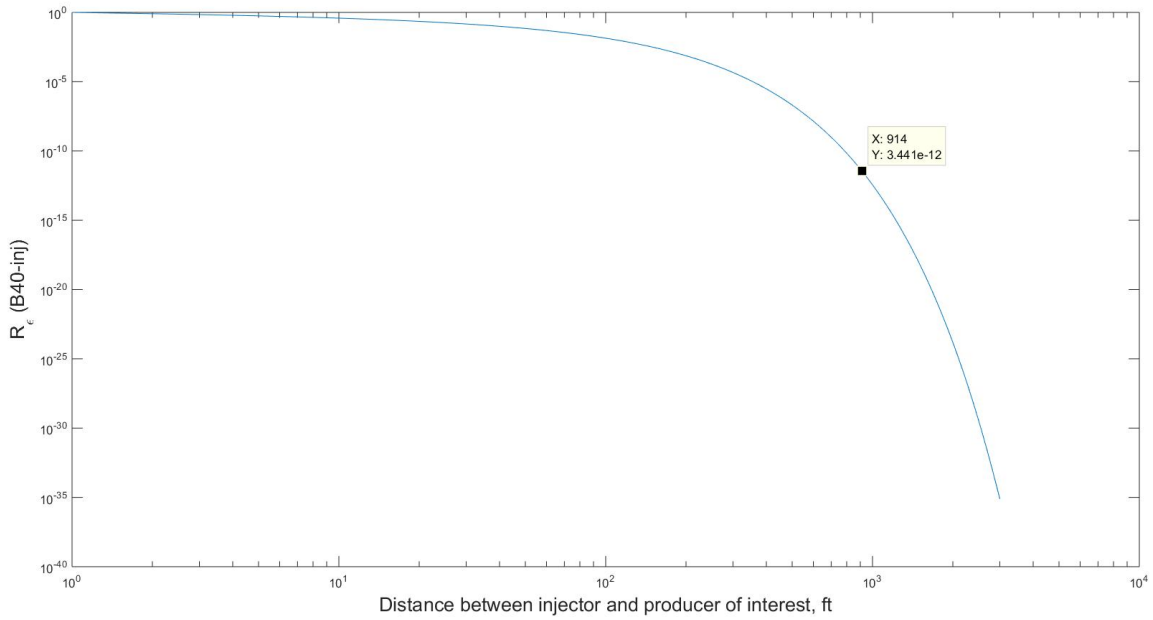

Figure A.2-5 B40-inj Rε plot

Appendix 3: Copyright Forms

Statement of Contribution of Coauthors for the Manuscript Entitled:
"Determining well-to-well connectivity using a modified capacitance model, seismic, and geology for a Bakken Waterflood"

The authors listed below have certified that:

1. They meet the criteria for authorship in that they have participated in the preparation, analysis, or interpretation of the results, of at least that part of the publication in the thesis in their field of expertise;
2. They take public responsibility for their part of the publication, except for the first author who accepts overall responsibility for the publication;
3. There are no other authors of the publications according to these criteria;
4. They agree to the use of the publications in the student's (first author) thesis.

Authors	Statement of contribution	Initials
Mammad Mirzayev	The first author involved in the model development, estimation of interwell connectivity, and participated in interpreting the results and main part of writing.	M.M.
Jerry Lee Jensen	Principal Investigator (PI), supervisor and the corresponding author.	J.L.J.
Naimeh Riazi	The author involved in interpretation of 3D seismic.	N.R.
Per Kent Perdersen	The author contributed with interpretation of the Bakken geology	P.K.P.
David Cronkwright	The author contributed with preparation of geological figures of the study area and part of the corresponding Section text.	D.C.

Principal Supervisor

Name: Dr. Jerry Lee Jensen

Copyright permission from the Elsevier

Journal of Petroleum Science and Engineering, **152, 711-727.**

DOI.org/10.1016/j.petrol.2017.01.032

Please find the answer to the question “Can I include/use my article in my thesis/dissertation?” from the list of Elsevier’s Frequently Asked Questions in the following pages.

Permissions

As a general rule, permission should be sought from the rights holder to reproduce any substantial part of a copyrighted work. This includes any text, illustrations, charts, tables, photographs, or other material from previously published sources. Obtaining permission to re-use content published by Elsevier is simple. Follow the guide below for a quick and easy route to permission.

Permission guidelines
ScienceDirect content
Non-ScienceDirect content
Help and support

Permission guidelines

For further guidelines about obtaining permission, please review our Frequently Asked Questions below:

When is permission required?

When is permission not required?
From whom do I need permission?
How do I obtain permission to use photographs or illustrations?
Do I need to obtain permission to use material posted on a website?
What rights does Elsevier require when requesting permission?
How do I obtain permission from another publisher?
What is Rightslink?
What should I do if I am not able to locate the copyright owner?
What is Elsevier's policy on using patient photographs?
Can I obtain permission from a Reproduction Rights Organization (RRO)?

Is Elsevier an STM signatory publisher?

Do I need to request permission to re-use work from another STM publisher?

Do I need to request permission to text mine Elsevier content?

Can I post my article on ResearchGate without violating copyright?

Can I post on ArXiv?

Can I include/use my article in my thesis/dissertation?

Yes. Authors can include their articles in full or in part in a thesis or dissertation for non-commercial purposes.

Which uses of a work does Elsevier view as a form of 'prior publication'?